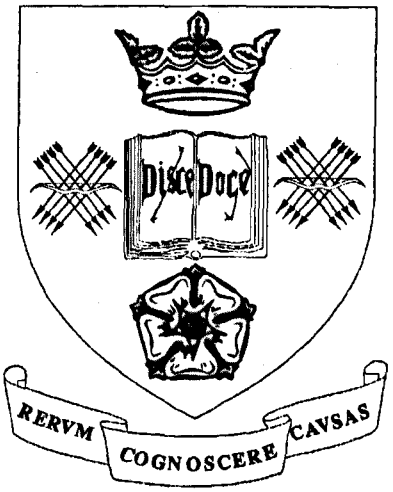

Laboratory simulation and modelling of the break-down rolling of AA3104

Menno Rutger van der Winden

Submitted for the degree of PhD, April 1999

Department of Engineering Materials,
The University of Sheffield

Abstract

Over the last few decades, the specifications for wrought aluminium products have become increasingly strict. Not only are the dimensional tolerances important, but also the material properties (strength, earing performance, corrosion resistance) must meet specified levels. The material properties are controlled by the microstructure. Hence the necessity for a modern aluminium plant to control the microstructure of the finished product through the processing parameters.

This microstructure strongly depends on the microstructures produced during each of the processing steps. Therefore, it is necessary to control the microstructure throughout the production process. It is thus imperative to know and model the influence of the processing conditions at each step.

The present work focuses on one processing step: break-down rolling. During this step, the thickness of the ingot is reduced from 500 to 25 mm on a reversing mill. Compared with the other production steps, break-down rolling has not been studied extensively. One of the reasons for this is the absence of a laboratory technique that simulates this process accurately. During this work the Sheffield Mill for Aluminium Roughing at Temperature (SMART) was developed and it was proven that SMART can be used to simulate industrial break-down rolling. Furthermore, the data generated from SMART have been used to validate and refine a model from the literature. This model (developed at NTNU in Norway) predicts the evolution of the recrystallised fraction, the grain size and certain texture components throughout a multi-pass rolling operation. It is shown here that the model predictions show a reasonable agreement with the results from SMART. Using the present experimental data, a set of recommendations to improve the model has been derived.

Apart from the microstructural data, the experiments on SMART were also used to model the lateral spread that occurs during laboratory rolling. A new model is proposed that shows a better performance compared with the models that are available from the literature.

The present work was carried out on AA3104 (Al-1Mn-1Mg) which is mostly used for the production of beverage cans.

Table of contents

1. Introduction

The processing of aluminium has dramatically changed since Hans Christian Oersted produced the first aluminium in 1827 [1]. Modern aluminium mills throughout the world run on a 24 hour a day schedule. This makes full scale experiments and trial runs very expensive and hard to realise. Furthermore, the rolling parameters in an industrial mill are not easy to change or measure. However, it is very desirable to experiment with the conditions during thermo-mechanical processing to optimise the process.

If predictive (computer-based) models were available and reliable, they would provide a useful alternative to full-scale experiments. For the thermo-mechanical treatment of aluminium, such models are not very well developed. Therefore, the use of laboratory simulation techniques can be extremely useful. By simulating the industrial process on a laboratory scale, insight can be gained regarding the outcome of full scale trials and hence the necessity for such trials will be reduced. Furthermore, based on the results of the laboratory simulations, better models can be developed to predict the behaviour of the material through the mill. These will not only help the day to day practice in industrial mills but also can aid the development of a better understanding of the metallurgy of aluminium during thermo-mechanical processing.

The aim of the present work is to develop further existing laboratory simulation techniques and to use the results to validate and improve the models that describe the microstructural development during the hot rolling of aluminium.

Firstly, the industrial process has been closely studied. Specifically the first hot rolling step (break-down rolling) in the production of sheet material has been analysed. From this analysis it became clear that two techniques were specially applicable to gain a better understanding of break-down rolling. In this project these two existing techniques, rolling on a laboratory mill and plane strain compression testing, have been used to investigate the influence of some key parameters upon the microstructural evolution during break-down rolling. The influences of temperature, homogenisation practice and chemical composition on the microstructural development have been studied. The microstructure was

characterised using optical microscopy, resistivity measurements, X-ray diffraction and scanning electron microscopy.

The results from the experimental simulations were then compared with predictions of models available from the literature. The models were then validated and further refined.

All the experimental work has been carried out on AA3104 (Al-1Mn-1Mg). This alloy is mainly used for the production of aluminium beverage cans and is therefore referred to as Can Body Stock (CBS). The industrial importance of this alloy is enormous, since beverage cans are a very important application for wrought aluminium.

This thesis consists of five sections: 'Literature review', 'Experimental work', 'Results', 'Discussion' and 'Conclusions and Further Work'. In the literature review the industrial process is analysed and the laboratory simulation techniques are discussed. This is followed by an overview of some existing models for hot rolling. The last part of this section discusses the microstructural development of AA3104 during thermo-mechanical processing. In the 'Experimental work' section all the experimental details of this work are presented. The results of the experiments are summed up in the 'Results' section and then discussed and compared with the literature and the model predictions in the next section. In the final section the conclusions are drawn and a list of suggestions for further work is given.

2. Literature Review

2.1 Industrial processing of can body stock

2.1.1 Introduction

Although the aluminium industry is not well known for its openness as far as production data are concerned, a general production schedule can be derived from the literature [2] [3] [4]. Figure 2.1 shows a flow chart for the production of can body stock (CBS). This figure also gives an indication of the thickness and the temperature of the material at each stage. It must be noted that considerable differences from this overview may occur for different companies.

Below a short overview is given of the main processing parameters of the different production steps.

2.1.2 Fluxing, Casting and Scalping

The mechanical properties and finishing characteristics of aluminium alloys are negatively influenced by non-metallic inclusions, alkali elements and hydrogen. To remove these inclusions, the molten metal is treated with a mixture of Ar/Cl gas, as it flows from the melting furnace to the casting unit. The gas is put into the melt via spinning nozzles. The non-metallic inclusions attach on to the fine gas bubbles and will float into the dross on top of the metal. After degassing, the molten metal is led through a ceramic foam filter where any remaining non metallic inclusions adhere to the large surface area of contact. For CBS, the removal of these inclusions is critical since any particles larger than 100 μm may cause holes in the final product.

The aluminium is normally Direct Chill (DC) cast into ingots of approximately 4700*1650*510 mm, weighing about 10 tons. The first patent for the vertical DC casting process was taken out by Ennor [5]. Figure 2.2 depicts the upper section of a DC-caster. At the start of the cast the mould is closed by the starter block. As the first of the metal is poured in, the starter block is lowered at a rate of several centimetres per minute. The water that cools the mould also sprays on to the surface of the emerging ingot to form a solid skin that contracts away from the

mould wall. After casting, the ingot is allowed to cool down to Room Temperature. To obtain the necessary surface quality, the skin of the ingot is milled away leaving an ingot of approximately 500 mm thickness. However, considerable differences from this procedure may occur at different suppliers. For instance, the initial thickness of the ingot can be as low as 300 mm. Obviously this will influence further processing. Also, the DC-casting technique has been refined into electromagnetic (EM) casting [6] (See figure 2.3). In this technique the water cooled moulds have been replaced by an electro-magnetic force, keeping the solidifying metal in its shape. Since there is no physical contact between the mould and the ingot, the surface quality will improve and thus decrease the need for scalping.

When either DC- or EM-casting is used to cast CBS, the further processing roughly follows the production schedule from figure 2.1. However, several other production routes have been developed. For instance, the metal can be produced by continuous casting incorporating in line hot and cold rolling mills. Various combinations of wheels, belts and rolls have led to differing machines [6]. However, these routes do not represent the most common industrial practice to date and are beyond the scope of this project.

2.1.3 Homogenisation

Figure 2.4 shows a typical temperature history during the homogenisation of AA3104. This heat treatment can be carried out in different furnace types such as; soaking pits with top lids, pusher furnace with slabs on shoes or batch furnaces with slabs on rail cars. After the homogenisation the slabs can either be air-cooled for subsequent rolling at a different plant or transported directly (while hot) to the break-down mill.

2.1.4 Break-down rolling

During the break-down rolling or roughing, the thickness of the initial ingot is reduced to about 25 mm. This reduction is achieved on a reversing mill in a number of passes. Some typical parameters of this process are shown in table 2.1 and will be discussed in this paragraph. The number of passes can vary from 9 to 25, depending on the size of the mill. The mill uses a combined coolant/lubricant of

soluble oil emulsion [7]. The initial temperature is normally controlled by the temperature at which the slab leaves the homogenisation furnace. However, this is valid only when the homogenisation treatment is integrated with the rolling. When this is not case (for instance when the homogenisation is carried out at a different site) an extra reheat treatment before rolling is necessary. In the literature there is little information available about the temperature development during the break-down rolling. Typically, the entry temperature is between 450 °C and 550 °C. At the initial stages, the thermal mass of the slab relative to its surface is so big that it hardly cools down during the inter-pass times. During the deformation the surface of the slab is chilled by the rolls, but the centre of the material is not affected by this and some deformational heating takes place. Therefore, the surface heats up again just after the deformation. At the start of break-down rolling, the inter-pass times are governed by the time the mill takes to reverse. This is of the order of 10 seconds. Later on, as the slab increases in length, the actual rolling becomes the time consuming step. This makes the inter-pass times longer (up to 1 minute). Because of the length of the slab, the actual inter-pass times throughout the slab vary from head to tail. The initial head and tail ends have a short and a long waiting time alternatively, depending on the rolling direction. Only the inter-pass time of the middle does not suffer from this effect. Towards the end of the break-down rolling process (normally after the penultimate pass) the ends of the slab are sheared off since they can lead to laminations and surface defects. Because of the time that cutting takes, that specific inter-stand time is lengthened considerably to around 3 minutes.

2.1.5 Tandem rolling and inter-annealing

The final hot rolling step is usually carried out in a tandem mill. Table 2.2 shows some typical parameters for this process. Compared with break-down rolling, tandem rolling is characterised by high strain and high strain rates during each pass. The number of passes is much lower and the inter-pass times are much shorter. After tandem rolling, the slab is coiled. To obtain a fully recrystallised structure before cold rolling, the coil can be annealed. This can either be done by just leaving the coil to cool down (if the exit temperature is high enough) or by placing it in a special furnace at around 350 °C for about one hour.

Since the capacity of tandem mills is much higher than that of reversing mills, some producers have two or three reversing mills upstream.

An alternative way of reaching the final gauge before cold rolling is the use of so called Steckel mini-mills [7] [3]. In this type of layout the tandem is replaced by one reversing mill with two coilers on either end. This mill takes the ingot down to final hot rolling gauge. However, this production route is beyond the scope of the present work and will not be discussed any further.

2.1.6 Cold rolling

In the cold rolling process the thickness is reduced to its final gauge of 0.25 mm. Normally the cold rolling is done on a three-stand tandem mill. The reduction per pass can be up to 60%, with speeds up to 2000 m/min, roll loads up to 1000 t/m width using a power of up to 3000 kW/m. Kerosene is the normal coolant, with 2 to 5% lubricant additives [7]. One of the key aspects in this process is the gauge control which should be within $5 \cdot 10^{-6}$ m [8]. Also the profile and shape control of the sheet are very important

2.1.7 Stabilising

After cold rolling, the coil is heated to approximately 150 °C. By doing this, the formability of the sheet is improved through partial recovery of the structure. By analogy with the inter-anneal after tandem rolling, this treatment may either be done in a separate furnace or may be integrated into the 'cold' rolling. It must be noted that since recovery already occurs at this low temperature, it may also occur during further processing steps. Especially curing of lacquers after can making may induce some recovery, reducing the strength of the can [9].

2.2 *Physical simulation techniques for break-down rolling*

2.2.1 Introduction

The objective of the physical simulation techniques used in this work is to simulate certain key aspects of the break-down process as closely as possible. Below, an analysis is given of the break-down rolling process from a simulation point of view. This analysis was used to choose and develop simulation techniques to study the microstructural and the mechanical behaviour.

Some key figures for the industrial break-down process are shown in table 2.1. The following parameters should be mimicked correctly during the physical simulation:

- Strain
- Strain-rate
- Strain (-rate) distribution
- Inter-pass times
- Temperature
- Friction conditions

These parameters are critical since they all have a strong influence on the microstructural development. In this project it was decided to use a laboratory mill to simulate break-down rolling. Each parameter is discussed together with the possibilities and or problems to simulate it on a laboratory mill.

It is essential to use the right definitions for these parameters. In the literature there is sometimes confusion about the exact definition of stress and strain. To be able to compare the results from different testing modes (i.e. plane strain compression versus tensile testing), it is essential to use one definition. In the present work, all stresses and strains are given as *equivalent true* stress (σ) and *equivalent true* strain (ε), and all the parameters that are derived from σ and ε, such as the strain rate ($\dot{\varepsilon}$) and the Zener Hollomon parameter (Z) are given as their 'true' values.

It is common practise to define all tensile stresses and strains as positive and their compressive equivalents as negative. In the present work, only compressive deformations have occurred, therefore the negative sign is omitted.

2.2.2 Strain

When a material is deformed under plane strain conditions, the *plane* strain (ε') is given as [10]:

$$\varepsilon' = \ln\frac{h_f}{h_0} \tag{2.1}$$

Where h_0 and h_f are the thickness of the slab before and after the deformation respectively. Assuming ideal plane strain (i.e. no lateral spread) and applying the von Mises criterion, the true strain can be calculated from this using equation 2.2 [10]:

$$\varepsilon = \frac{2}{\sqrt{3}}\cdot\varepsilon' = \frac{2}{\sqrt{3}}\ln\frac{h_f}{h_0} \tag{2.2}$$

Equation 2.2 assumes the strain to be homogeneously distributed throughout the thickness of the specimen.

Equation 2.2 is equally valid to either calculate the strain per pass or the total strain over any number of passes. In break-down rolling the accumulated strain can be as high as 3.5. Given the maximum and minimum gauge that can be achieved on the laboratory mill (50 and 2 mm) such a total strain is feasible for this technique.

2.2.3 Strain-rate

A first order estimate of the instantaneous strain rate throughout the roll gap can be derived from the geometry of rolling [10], assuming sticking friction conditions, as:

$$\dot{\varepsilon} = \frac{2}{\sqrt{3}}\left(\frac{dh}{dt}\right)\cdot\left\{\frac{1}{h}\right\} = \frac{2}{\sqrt{3}}\left(2\cdot v\cdot\sin\theta\right)\cdot\left\{\frac{1}{h_f + 2\cdot R_R\cdot\left(1-\cos\theta\right)}\right\} \tag{2.3}$$

Where R_R is the radius of the work rolls and θ is the angle subtended at the centre of the roll (see figure 2.5). The peripheral speed of the work roll (v) is given by:

$$v = 2 \cdot \pi \cdot R_R \cdot s \tag{2.4}$$

Where s is the speed of revolution of the rolls. To calculate the mean strain rate ($\dot{\bar{\varepsilon}}$) on the basis of time, equation 2.3 must be integrated over θ. This gives:

$$\dot{\bar{\varepsilon}} = -\frac{2}{\sqrt{3}} \cdot \frac{1}{\theta_0} \int_{\theta_0}^{0} \frac{2 \cdot v \cdot \sin\theta}{h_f + 2 \cdot R_R \cdot (1 - \cos\theta)} d\theta \tag{2.5}$$

$$= -\frac{2}{\sqrt{3}} \cdot \frac{v}{R_R \cdot \theta_0} \ln \frac{h_f}{h_0} \tag{2.6}$$

$$\approx -\frac{2}{\sqrt{3}} \cdot \frac{v}{\sqrt{R_R \cdot (h_0 - h_f)}} \ln \frac{h_f}{h_0} \tag{2.7}$$

The minus signs in equation 2.5 to 2.7 are usually ignored. Again, its presence signifies that the strain rate is calculated for compressive strain rates. Equation 2.7 can now be used to calculate the average strain rate in the industrial situation and from that, the speed of revolution of the laboratory mill is derived. The maximum strain-rate in the industrial process is 10 s^{-1} in the final passes. This results in a speed of revolution that is within the limits of a standard laboratory mill.

2.2.4 Strain (-rate) distribution throughout the thickness of the slab

So far, only the average values for strain and strain-rate have been considered. However, from slip-line field analyses (see figure 2.6) [11] it is seen that specially for break-down rolling, the deformation is far from homogeneous. The strain and strain-rate within an industrial slab will vary through the thickness. This is mainly a function of the roll radius (R_R) and the reduction. Backofen [12] defined a ratio (the mean zone-thickness/contact length ratio) Δ, to describe this effect as follows:

$$\Delta = \frac{\bar{h}}{\sqrt{R_R(h_0 - h_f)}} \approx \sqrt{\left(\frac{h_0 \cdot h_f}{R_R \cdot (h_0 - h_f)}\right)} \qquad (2.8)$$

Where $\bar{h}$ is the geometric average thickness of the slab.

The importance of Δ lies in its relationship with the deformation and recrystallisation textures [12]. To simulate these, it is necessary to have the same Δ-factor during the physical simulation to compare with the industrial process. When Δ is known, it can then be used to calculate the initial thickness for the laboratory mill with a given roll radius.

Again, the results from such calculations yield an initial thickness that is within the range of a laboratory mill.

2.2.5 Inter-pass times

In this project any difference in inter-pass time between the head and the tail end of the industrial slab is ignored. All work is focused on the middle of the industrial slab which will have gradually increasing inter-pass times. Before the last pass, the slab is transported away from the mill to cut off the head and tail ends. This results in an extra long inter-pass time. After the final pass, the inter-pass time is no longer determined by the break-down mill. At this stage in the process it is the entry to the tandem mill that is rate-determining. Normally, the tandem mill is positioned in line with the break-down mill, thus ensuring a short time between the last break-down pass and the first tandem pass. It is concluded that a laboratory mill can meet the minimum inter-pass times occurring in industry.

2.2.6 Temperature

In the industrial practice, the temperature of the slab is only measured before and after break-down rolling. Because of the way these measurements are done (contact thermometers) they have a limited accuracy. Therefore it is preferred to use first principle modelling to predict the temperature of the slab. Because of the

large thermal mass of the slab, the temperature during the first passes of break-down rolling will be fairly constant. Only on the last passes will the slab be thin enough to cool down during the inter-pass times. However, when using a laboratory mill the specimen will cool down considerably from the first pass and even faster with higher pass number. This is due to the chilling of the specimen by the (cold) rolls [13] [14] and the loss of heat during the inter-pass times. Therefore a standard laboratory mill cannot be used to simulate the complete process of break-down rolling. To overcome this problem, a new simulation technique has been developed where the mill is equipped with two directly adjacent tube furnaces. This technique will be described in detail in chapter 3.2.

2.2.7 Friction conditions

In the literature, sticking friction conditions are normally assumed for hot rolling operations (the equations 2.3 to 2.7 also use this assumption). Regretfully, there are very few data available about the actual friction conditions. During break-down rolling of aluminium, the rolls are sprayed with an emulsion of oil and water. To mimic the industrial situation as closely as possible, a lubricating system on the laboratory mill, using a similar emulsion was developed. However, this is no guarantee that the friction conditions are identical.

2.2.8 Relation between the grain size and the slab thickness

As cast aluminium has a typical grain size of 140 μm. In a 500 mm thick slab, this means that there are thousands of grains through the thickness. In the laboratory simulation the whole process is scaled down. However, since the same starting material is used in both industry and simulation. The initial grain size does not scale with the laboratory simulation. When the number of grains through the thickness becomes too small, the simulation of texture development will become inaccurate. In a 50 mm thick specimen for a laboratory mill, there are still about 350 grains through the thickness. This is enough to justify the assumption that the material will behave in a similar way to the industrial situation.

2.2.9 Plane strain compression testing

When simulating break-down rolling, plane strain compression (PSC) testing must be considered as an alternative simulation technique. This technique was originally developed by Watts and Ford [15] for testing at room temperature. Modern PSC-machines can test at high temperatures (up to 1100 °C). They also offer an excellent control of strain, strain-rate, inter-pass time and temperature [16]. However, PSC is not an obvious technique for the simulation of break-down rolling. The main problem lies in the high total reduction. Since the initial thickness of a PSC specimen is normally limited to 10-12 mm. the specimen is only 0.5 mm thick after 95% reduction. Such a small thickness carries not only severe practical problems, but also the influence of surface effects are very large. Furthermore, the strain per pass during break-down rolling is relatively small. This means that, specially in the later passes, the absolute reduction of the thickness of the specimens is below the resolution of the machine. Also the number of (as cast) grains through thickness in a standard PSC-specimen is relatively small [17], which causes problems when simulating the texture development. Finally, the deformation in a PSC-machine is in principle homogeneous through the thickness. For the highly non-homogeneous deformation during break-down rolling, it would be necessary to do separate simulations for different depths below the surface.

Nevertheless, a PSC machine has a number of features that can be very useful in a project such as this one. A strong point of PSC-testing is its accuracy in determining the mechanical response of the material. Therefore, in this project, this technique has been used to characterise the mechanical strength of the material at different stages of the break-down process.

2.3 *Physical metallurgy of AA3104*

2.3.1 Introduction

The alloy AA3104 is mainly used for the production of Can Body Sheet (CBS) for the production of beverage cans. The commercial importance of this alloy is enormous. (In 1994 the production of aluminium beverage cans in the USA alone, was 1.03 billion cans [8].)

Table 2.3 shows the limits for the chemical composition of AA3104 as prescribed by the Aluminium Association [18]. The chemical composition influences the microstructural development during thermo mechanical processing. Therefore, a short analysis of the main elements is given below. After this, an overview of the microstructural development from casting to break-down rolling is given. Here, mainly a qualitative approach is used. How these mechanisms could be modelled quantitatively is discussed in chapter 2.4.

2.3.2 Main alloying elements

2.3.2.1 Manganese

Manganese is the most important alloying element in the 3XXX series. It is present in the alloy both as precipitates and dissolved in the matrix. The maximum solubility of Mn in pure Al is 1.6 wt.% at 625 °C. From the ternary phase diagram [19] (see figure 2.7), it is seen that this decreases in the presence of Fe. At 0.7 wt.% Fe, only 0.3 wt.% Mn can dissolve at 625 °C. This will be even less at lower temperatures. Due to the high cooling rates after the casting of the metal, not all the Mn will precipitate during and after solidification. An as cast ingot will thus be supersaturated with Mn. Hence there is a driving force for Mn to precipitate during the thermo-mechanical processing.

The precipitated manganese can be α-AlFeMnSi, β-$(Fe,Mn)Al_6$ or $MnAl_6$. Usui et al. [20] found that $MnAl_6$-precipitates have a restraining effect on the dynamic recovery.

2.3.2.2 *Magnesium*

Magnesium has a large solubility range in aluminium alloys. It has a strong influence on the work-hardening of the material. At room temperature the UTS increases roughly linear with the amount of Mg. At hot working temperatures a power law relationship applies [16]:

$$\sigma^{ss} = k \cdot w^{0.25} \tag{2.9}$$

σ^{ss} = steady – state flow stress
w = atomic percentage Mg
k = temperature dependent constant

In the presence of Si, Mg can form Mg_2Si during and after the solidification.

2.3.2.3 *Silicon*

Si mainly influences the microstructure though its strong tendency to form inter-metallic compounds with Al, Fe, Mg and Mn [21]. The two main Si-containing precipitates are Mg_2Si and α-$Al_{12}(Fe,Mn)Si$. The α-precipitates are mainly formed after the solidification out of β particles via diffusion of Si. Therefore the amount of Si highly influences the ratio between α- and β-particles.

2.3.3 Microstructural development during thermo mechanical processing

Between being an as-cast ingot and the final product, the microstructure of the material changes dramatically. The microstructure can be characterised from several viewpoints:

- The dendrite arm spacing (in case of the as cast structure)
- The second phase particles (composition, size, morphology, distribution and volume fraction)
- The grain structure (size, morphology, distribution, texture)
- The subgrain structure (size, dislocation density, misorientation)

All these variables interact with each other when the microstructure develops during thermo mechanical processing. To be able to model this development, a thorough understanding of all aspects is necessary. Especially in aluminium, the microstructure of the final (cold rolled) sheet depends on the complete thermo

mechanical history. Therefore, the microstructural development throughout the production process needs to be understood. Below this is done for the first processing steps; from the as cast to the transfer gauge structure (i.e. after break down rolling). The further development during the rest of the processing steps is beyond the scope of this work.

2.3.3.1 The as-cast structure

The as-cast structure is dendritic containing about 2 vol.% of second phase particles. The dendrite arm spacing can range from about 10 to 100 microns in a DC ingot [6]. It has also been found to have a power law dependence on the solidification rate:

$$S = AJ^n \tag{2.10}$$

Where S equals the dendrite cell size, A and n are constants and J is the solidification rate. From Morris et al. [22] it can be derived that A equals 50 10^{-6} and n is -0.3. This value of n agrees with that found by Spear and Gardner [23]. The dendrite cell size is used rather then the dendrite arm spacing since in commercial castings the secondary arms are not developed.

The precipitates that are formed during solidification are normally called constituent particles. Most of these particles are β-(FeMn)Al_6 and Mg_2Si [24]. The β-phase surrounds the dendrites as faceted plate like shapes [25]. Their structure depends on the solidification rate. It is finer and less massive when this rate increases [22]. It has also been found that a proportion of the Fe constituent particles is α-Al_{12}(FeMn)Si, where the amount of the α-phase and the Mg_2Si both depend on the Si content. During the solidification sequence, both particles compete for the Si partitioned to the inter-dendritic liquid [24].

Apart from the second phase particles, the degree of supersaturation is also important for subsequent processing. Most of the Mn content and about 5% of the Fe, is supersaturated in solid solution. The exact degree of supersaturation highly depends on the solidification rate [22].

The grain size ranges from about 50 to 500 microns [6] in a grain refined DC-ingot. Master alloys containing heterogeneous nuclei are used to obtain an equi-axed structure.

2.3.3.2 The homogenised structure

The as-cast structure is then homogenised. From a linear regression analysis by Goodrich [26] it can be concluded that this treatment is very important to the microstructure of the final (cold-rolled) sheet. The main objectives of homogenisation are [24] [16] [22] [26] :

- elimination of supersaturation and microsegregation
- transformation of β-(FeMn)Al_6 constituents to α-Al_{12}(FeMn)Si
- spheroidisation and coarsening of the eutectic constituents

The precipitation from the supersaturated state was modelled by Goodrich [26] assuming Avrami kinetics. From this model the amount of dissolved Mn can be calculated for a typical homogenisation treatment. Figure 2.8 shows the result of such a calculation. This model was later refined by Suni et al. [95], who used a set of more physically based equations.

During the homogenisation the β-(FeMn)Al_6 constituents formed after solidification transform into to α-Al_{12}(FeMn)Si via the diffusion of Si atoms [28]. The distribution, size, morphology and physical properties of these second phase particles should be very well controlled to effect a tool cleaning action during deep drawing sufficient to suppress aluminium build-up on the tooling [8].

2.3.3.3 Microstructural development during break-down rolling

During the break-down rolling, both the second phase particles and the grain structure are changed dramatically. The driving force for these changes, originates from the deformation of the slab.

The evolution of the constituent particles in Al-1Mn-1Mg during break-down rolling has been studied by Daaland [29]. In the as-cast structure, these particles exhibit a cell structure. This structure changes with increasing pass number. The cells are broken up into a mixture of layers (in the rolling plane) of sheared particles and

particle free layers. In the microstructure after the last break-down pass, these layers have disappeared. Now, the sheared particles are distributed homogeneously. Obviously, the shearing process influences the average size and the size distribution. In the as-cast structure the average size was found to be 4.7 μm showing a very wide distribution. At the transfer gauge, the average is reduced to 1 μm with a much narrower distribution. However, the particles are still not completely spherical and are aligned in the rolling direction. The development described above, applies to the centre of the slab. At the surface the deformation is very different. There, the material is heavily sheared, resulting in much higher local strains. This accelerates the break up of the constituents. Therefore, the cell and layered structures disappear much faster at the surface. However, at the transfer gauge, the centre has caught up and no difference is found between the surface and the centre.

When the slab is still supersaturated after homogenisation, precipitation can occur during break-down rolling. The combination of an increased dislocation density and the high temperature during the inter-pass times will enhance precipitation.

The structure of the matrix also changes dramatically when the slab is rolled. The shape of the grains changes from spherical to pancake. To accommodate the deformation, the grains have to rotate. Some grains will rotate in more than one way, causing such a grain to break into different regions of different orientation. The boundaries between these regions are normally referred to as transition bands [30]. Especially after the higher strains, the material will also develop shear bands. This phenomenon occurs when a structure has nearly exhausted its storing capacity for dislocations. The material within the shear bands appears to be sharply mis-oriented with respect to the surrounding matrix. It is important to notice that the shear bands are not dictated by considerations of crystallography. Even after heavy rolling, they are running at 35° to the rolling plane. They can cross several grains. However, the mechanism by which these bands are formed is still largely unknown.

Within the grains, the structure changes upon deformation as well. Initially, just the dislocation density increases. Upon higher strains, these forest dislocations will

become ordered into sub-grains. These sub-grains are equi-axed. They stay shaped like this with higher deformation due to repolygonisation.

Not only the shape and size of the (sub) grains changes during deformation, their orientation does so as well. The distribution of the crystallographic orientations of the crystallites in a polycrystalline material is normally referred to as the texture of a material. During a rolling pass a deformation texture develops. Although the details of the underlying mechanisms are beyond the scope of this discussion, it can be shown that certain texture components develop during the rolling of (high stacking fault) fcc metals (For further information see Taylor [31], Aernoudt [32] and Sevillano et al. [33]). It is shown that most orientations assemble along two incomplete fibers in the Euler space: the α-fibre which runs from the goss orientation {011}<100> to the brass (Bs) orientation {011)<211>, and the β-fibre that runs from the copper (Cu) orientation {112}<111> over S {123}<634> to Bs. Both fibres are shown in figure 2.9. These predictions have been validated for Al-1Mn-1Mg by Maurice et al. [34].

After the deformation, the slab is self annealing during the inter-pass time. During this period, the so called static changes occur. The most important one is static recrystallisation. New, dislocation free, grains grow into the deformed old ones. Numerous books have been written about this process (see for instance Haessner [35] or Humphreys and Hatherly [30]) and only some selected aspects will be discussed here.

Upon recrystallisation the texture of the slab changes. The origin of such recrystallisation textures has been a matter of controversy for decades. The main point of discussion is whether oriented nucleation or oriented growth is the dominating mechanism. Vatne [36] has shown for Al-1Mn-1Mg, that no growth selection occurs in AA3104.

The oriented nucleation mechanism implies that the recrystallisation texture is determined by the orientations of the available nuclei in the as-deformed material. It is therefore important to take a close look at the categories of nuclei with a specific orientation. Two of these are discussed in more detail below.

The first category is the cube texture ({001}<100>). This component is very important because of its strong influence on the earing behaviour of the final product. To obtain a cube recrystallisation texture, cube oriented nuclei must be present in the deformed state. It was shown by Daaland [29] that a fraction of the cube crystallites present before the deformation can survive the deformation and form the nuclei for recrystallisation. It has been argued [30] that the surviving cube sites form especially potent nuclei due to extensive recovery. The Burgers vectors of the two most dominant slip systems are orthogonal to each other ($a/2[101]$ and $a/2[\bar{1}01]$) and therefore there is little interaction between them. This yields fast and extensive recovery.

Alternatively, the cube grains can be formed during the deformation. This phenomenon can be explained with the Dillamore-Katoh mechanism [27]. They predicted that during plane strain compression of a high stacking fault, fcc metal, transition bands might develop that contain the cube orientation. The transition bands are surrounded by large orientation rotations and can thus easily gain a high angle character. This situation can thus provide a cube nucleus.

However, it is not just the volume fraction of Cube in the deformed metal that determines the amount of Cube, once recrystallised. Vatne [36] found that a Cube-neighboured by an S-grain forms an especially potent nucleus. This could be interpreted as proof of an oriented growth mechanism. However, it was shown by Vatne that the explanation for this preference lies in the energy of such a grain boundary. S and Cube make a 40°<111> orientation relationship. Such a boundary has a high coincidence site density and thus a low grain boundary energy. Therefore the Gibbs-Thomson radius (= minimum radius for a nucleus to be successful) is relatively small. Thus, a Cube grain surrounded by an S-grain has a higher chance of forming successful nuclei.

The second category discussed here, is the amount of randomly oriented grains. Naturally, this category cannot be represented by any particular volume in Euler-space. However, to generate a random texture, randomly oriented nuclei must be available. From this point of view, random texture can be considered a normal texture component. One of the mechanisms to form randomly oriented nuclei, is

called Particle Stimulated Nucleation (PSN). This mechanism was first described by Humphreys [30]. The idea behind this mechanism is that during the deformation a deformation zone is formed around non-deforming second phase particles. The deformation zones are areas of high stored energy and a progressive lattice rotation from the remote matrix to the particle surface. This situation provides ideal conditions for a nucleus to grow. The critical step is therefore not the consumption of the deformation zone itself, but its growth into the less highly strained matrix. This means that nucleation will only be successful at particles with a deformation zones larger than a critical value in order to provide the growing nuclei with a sufficient size advantage.

An alternative site for randomly oriented nuclei can be found at grain boundaries. Statistically, next to these boundaries, a certain fraction of the subgrains will be large enough to form a nucleus. The combination of such subgrains with a mobile grain boundary provides the possibilities for recrystallisation to start.

To improve the readability, the discussion above, assumes a strict separation between the dynamic and static changes in the microstructure. As far as the shearing of the constituent particles is concerned, this is correct. However, precipitation may occur either during or after the deformation. When looking at the changes in the matrix, the difference between static and dynamic may be even more disputable. Some authors report ([37], [38]) that the recovery process does not stop when the deformation is finished. Also, there have been many publications about dynamic recrystallisation in aluminium during hot working. Those observations can be split into continuous and discontinuous recrystallisation phenomena. The continuous mechanism (CDX) involves grain boundary impingement (geometric dynamic recrystallisation) [30] and is thought to be important in the development of microstructure in superplastic alloys. This process is not a softening mechanism in the sense that it reduces the dislocation density of the material. Discontinuous dynamic recrystallisation (DDX) is a nucleation and growth process that is analogue to the normal static recrystallisation. This phenomenon has been found in two kinds of aluminium alloys. Firstly, in alloys with a very high amount of dissolved elements [30]. This lowers the stacking fault energy, which hinders dislocation climb. Therefore, the stored energy cannot be

lowered easily via recovery, and thus recrystallisation occurs more easily. When the stored energy gets high enough during the deformation, recrystallisation can occur dynamically. Secondly, DDX was found to occur is in exceptionally pure aluminium [39]. The explanation for this lies in the extremely high mobility of the grain boundaries in such alloys. In that case, the minimum stored energy to start recrystallisation during the deformation already is very low. There is one more case of DDX. Huang et al. [40] found that when the strain rate is instantly lowered several orders of magnitude during a deformation, DDX can occur in AA1050. The explanation for this lies in the microstructure that is formed during the first (fast) part of the deformation. This structure has a high stored energy. When the strain rate is lowered, such a structure must change into one that 'belongs' to the lower strain rate. Therefore, the amount of stored energy needs to be reduced which can occur via DDX.

From the discussion above it can be concluded that it is unlikely that dynamic recrystallisation will occur during break-down rolling of AA3104. Whether static recovery occurs, is unclear at the present moment. However, the assumption that the static and dynamic changes are distinctively different seems to be good enough to be used for a first order modelling attempt.

2.4 *Modelling microstructural development during hot rolling*

2.4.1 Introduction

In the previous chapter, a qualitative analyses was given of the microstructural development of AA3104 during casting, homogenisation and break-down rolling. The main focus of this project is the microstructural development during break-down rolling. To control the microstructure during this process, a qualitative approach does not suffice. Therefore some quantitative models from the literature are discussed below.

From an industrial point of view it could be sufficient to know the final microstructure as a function of the thermo-mechanical treatment parameters. However, especially in aluminium, the final structure very much depends on the intermediate structures. Therefore, an approach where the microstructure throughout the rolling schedule is predicted, is more likely to perform better.

Figure 2.10 shows a schematic diagram of the principles of such a multi-pass model [41] [42]. When all relationships within this diagram are known, it is possible to calculate the exact microstructure at the end of each inter-pass time. In figure 2.10, several 'sub-models' can be distinguished. These sub-models describe certain aspects of the behaviour of the material during rolling. For each aspect, several approaches are available from the literature. A selection of these is discussed below. After this, two computer programs that integrate these sub-models are described.

2.4.2 Sub-models

2.4.2.1 Mechanical behaviour

To see if a particular combination of rolling parameters and alloy is feasible within the design limits of the mill, it is necessary to predict the rolling loads. Such prediction is also used as a pre-set value for the mill. The rolling loads depend largely upon the stress-strain behaviour of the material as a function of temperature

and strain rate(amongst other factors like the geometry of the reduction and the friction conditions). The stress-strain behaviour can be described using constitutive equations. Constitutive equations can be derived in two stages; firstly, equations are derived for discrete, characteristic points on the stress-strain curve in terms of the Zener Hollomon parameter (Z) and secondly, complete continuous flow stress curves are calculated based upon the first set of equations.

The equations from the first stage will be referred to in this work as sigma(Z)-equations. Over the last decades, several models to describe such curves have been developed. Here two of them are discussed. First, an empirical approach that uses several characteristic points from a stress-strain curve and then, a more physically based model only describing the steady state situation.

Empirical equations for sigma(Z)

Based on extensive investigations of creep and hot working, Sellars et al. [43] proposed a set of empirical formulae to describe the relationship between the Zener Hollomon parameter and the stress. For low stresses:

$$\sigma^{\#} = \left(\frac{Z}{A_1^{\#}}\right)^{\frac{1}{n_1^{\#}}} \tag{2.11}$$

Where Z is Zener Hollomon parameter which is defined as $Z = \dot{\varepsilon} \exp\frac{Q_{def}}{RT}$, Q_{def} is the activation energy for deformation and R is the universal gas constant. In equation 2.11, $\sigma^{\#}$ denotes the stress at a characteristic point on the stress strain curve and $A_1^{\#}$ and $n_1^{\#}$ are its accompanying constants. For higher stresses it was found that:

$$\sigma^{\#} = \frac{1}{\beta_2^{\#}} \ln\frac{Z}{A_2^{\#}} \tag{2.12}$$

With $\beta_2^{\#}$ and $A_2^{\#}$ being constants for each $\sigma^{\#}$. Equation 2.11 and 2.12 can be combined into:

$$\sigma^{\#} = \frac{n_3^{\#}}{\beta_3^{\#}} \operatorname{arcsinh}\left(\frac{Z}{A_3^{\#}}\right)^{\frac{1}{n_3^{\#}}} \qquad (2.13)$$

Where $\beta_3^{\#}$, $n_3^{\#}$ and $A_3^{\#}$ are constants at the characteristic stresses. These stresses may for instance be chosen as the stress at a fixed value of strain (σ^{ε}) or the steady state stress (σ^{ss}).

The equations 2.11, 2.12 and 2.13 can then be used to describe the actual shape of the stress strain curve. A way of doing this was proposed by Sah et al.:

$$\sigma = \sigma^0 + \left(\sigma^{ss} - \sigma^0\right) \cdot \left(1 - \exp(-C\varepsilon)\right)^m \qquad (2.14)$$

Where C and m are constants that need to be derived from experimental data.

Physically based equations for sigma(Z)

Recently a first attempt has been made by Nes [44] to derive a more physically based constitutive equation. This equation only models the steady state stress and makes no attempts at modelling the work hardening behaviour at lower strains.

This equation was derived from the predicted relationship between the steady state stress (σ^{ss}) and the internal structure parameters ρ_i (dislocation density in the cell interior) and δ (sub-grain size).

$$\sigma^{ss} = \sigma^{i} + \alpha_1 Gb\sqrt{\rho_i} + \alpha_2 Gb\frac{1}{\delta} \qquad (2.15)$$

Where σ^{i} is a frictional stress, G is the shear modulus and b is the Burgers vector, α_1 and α_2 are constants. The last two terms of equation 2.15 can be combined, using the principle of similitude found by Castro Fernandez et al. [45]. This principle predicts that:

$$\sqrt{\rho_i} = C_\delta \cdot \frac{1}{\delta} \qquad (2.16)$$

Combining this relationship with equation 2.15, it follows for the steady state flow stress:

$$\sigma^{ss} = \sigma^{i} + \alpha_3 Gb\frac{1}{\delta} \tag{2.17}$$

Where $\alpha_3 = C_\delta\alpha_1+\alpha_2$

Nes now calculated the subgrain size using the assumption that during steady state the rate of subgrain boundary creation equals the subgrain growth rate from dynamic recovery. This analysis lead to:

$$\frac{1}{\delta} = \frac{C_2\dot{\varepsilon}\exp\left(\frac{Q_i^b}{kT}\right)}{2\sinh\left(\frac{C_1 l_s^b}{\delta kT}\right)} \tag{2.18}$$

With: $C_1 = 6\alpha_4 Gb^3$

$$\alpha_4 = \frac{1}{4\pi(1-\nu)}$$

$$C_2 = 0.07\cdot\frac{M}{\nu_D b C_B}$$

U_i^b the interaction energy between the solute atom and the boundary dislocation core

l_s^b the separation of solute atoms along the boundary dislocation line

ν Poisson's ratio

k Boltzmann's constant

ν_D the Debye frequency

M the Taylor factor

C_B a constant to be determined experimentally

Equation 2.18 can only be solved numerically. For $PV_a^b / kT > 1$ (P is the driving pressure for subgrain growth and V_a^b an activation volume), equation 2.18 takes the form:

$$\frac{1}{\delta} = \frac{kT}{C_1} \ln(Z\delta C_2) \; \forall \; \frac{PV_a^b}{kT} > 1 \tag{2.19}$$

Equation 2.19 is quite similar to the empirical equation found by Castro Fernandez et al. [46]

$$\frac{1}{\delta} = A \ln Z - B \tag{2.20}$$

With A and B being alloy dependent constants. It was shown by Nes [44] that both equations (equation 2.19 and 2.20) describe the experimental results equally well for ln Z > 27. Below this value equation 2.20 results in very large or even negative values for $\frac{1}{\delta}$ which cannot be correct.

The steady state flow stress can now be found by combining equation 2.17 and 2.19 into:

$$\sigma^{ss} = \sigma^{i} + \frac{M\alpha_3 GbkT}{C_1} \ln \frac{Z\alpha_3 MGC_2}{\sigma^{ss} - \sigma^{i}} \tag{2.21}$$

This model is discussed in more detail by Nes [44] and Nes and Furu [47].

From the literature and the discussion above, it can be concluded that the physical equations are able to describe the experimental results equally well as the empirical ones. However, this is also due to the use of several fit parameters in the physical equations (α_1 to α_4, C_δ and C_B). In the present work, both set of equations will be applied and their results compared with each other.

2.4.2.2 Recrystallisation

Recrystallisation kinetics in between passes (static recrystallisation) is normally described, using Avrami kinetics [30].

$$f = 1 - \exp\left(\ln(1 - 0.5)\left(\frac{t}{t_{0.5}}\right)^n \right) \tag{2.22}$$

Where f is the recrystallised fraction and $t_{0.5}$ is the time for 50% recrystallisation. The Avrami exponent, n, describes the time dependency of the nucleation and growth rates. Theoretically, n equals 3 in the case of site saturation and constant growth rate and 4 when nuclei are formed at a constant rate during the recrystallisation [48]. However, a value of n=2 is normally found to describe the experimental results best [29].

The temperature, strain, strain-rate and grain size dependence of the recrystallisation kinetics is described using the time for 50% recrystallisation ($t_{0.5}$) [49]:

$$t_{0.5} = B_1 \cdot Z^{B_2} \cdot \varepsilon^{B_3} \cdot d_0^{B_4} \cdot \exp\left(\frac{Q_{stat}}{RT}\right) \tag{2.23}$$

B_1 to B_4 are constants to be determined experimentally, d_0 is the initial grain size and Q_{stat} is the activation energy for static recrystallisation. When equation 2.22 and 2.23 are applied to industrial hot rolling the problem arises that these processes are not iso-thermal. Such temperature changes can be taken into account by using the principle of temperature compensated time. According to Whittaker [50] and Sellars et al. [51] the temperature compensated time is defined as:

$$W = \sum t_i \cdot \exp\left(\frac{-Q_{stat}}{RT_i}\right) \tag{2.24}$$

Where t_i is the time interval that the slab has a temperature of T_i. Using equation 2.24, equation 2.22 can be modified into:

$$f = 1 - \exp\left(\ln(1-0.5) \cdot \left(\frac{W}{W_{0.5}}\right)^n\right) \tag{2.25}$$

Brand et al. [52] use the temperature compensated time for 95% recrystallisation ($W_{0.95}$) to characterise the recrystallisation behaviour of the material. When $W_{0.95}$ is known, $W_{0.5}$ can be found using:

$$W_{0.5} = W_{0.95} \cdot \sqrt{\frac{\ln(1-0.5)}{\ln(1-0.95)}} \tag{2.26}$$

However, when using light microscopy to determine the recrystallised fraction, the use 95% carries severe experimental disadvantages.

When $t_{0.5}$ is known, $W_{0.5}$ can be found by applying equation 2.24 for isothermal conditions. In that case equation 2.24 becomes:

$$W_{0.5} = t_{0.5} \cdot \exp\left(\frac{-Q_{stat}}{RT}\right) \tag{2.27}$$

and thus (Combining equation 2.23 and 2.27):

$$W_{0.5} = B_1 \cdot \varepsilon^{B_2} \cdot Z^{B_3} \cdot d_0^{B_4} \tag{2.28}$$

Recrystallisation is not only a softening process. It also influences the grain size and grain shape in the material. Directly after the deformation, the grains become pan-cake shaped according to the strain applied. When this structure recrystallises, new equi-axed grains are formed. Again, the literature gives a purely empirical as well as a more physically based solution to describe the final grain size after pass i (D_i) of the recrystallised grains. The empirical equation is of the form [52]:

$$D_i = C_1 \cdot Z^{C_2} \cdot \varepsilon^{C_3} \tag{2.29}$$

Where C_1, C_2 and C_3 are alloy dependent constants.

An alternative approach is given by Vatne [36] where the recrystallised grain size follows from the number of available nuclei (N^i_{TOT}) and the recrystallised fraction.

$$D_i = \left(\frac{f_i}{N^i_{TOT}}\right)^{\frac{1}{3}} \tag{2.30}$$

Equation 2.30 assumes that the number of nuclei is known after each pass. How to achieve this is discussed in section 2.4.3.2 (The NTNU Model) below.

2.4.3 Integrated Models

So far, the models described are dealing with specific aspects of thermo-mechanical processing. Over the last few years a few computer programs have been written to integrate the different aspects. Each program uses its selection of the equations described above.

2.4.3.1 SLIMMER

The Sheffield Leicester Integrated Model for Microstructural Evolution in Rolling was developed by Beynon et al. [53] [54]. It is a computer program that couples a thermal and a microstructural model with the hot rolling theory for calculating operating loads as described by Sims [55]. The input of the model consists of the initial dimensions, grain size and temperature of the slab, some physical parameters and the rolling schedule. The model calculates the temperature, the grain size, the fraction recrystallised and the rolling loads throughout the programmed schedule for up to 20 consecutive passes. The thermal model uses a finite difference technique to calculate the temperature profile on a transverse section of the stock as it progresses down the schedule. The temperature is calculated assuming heat loss to the surrounding air by convection and radiation. During the deformation the slab loses heat to the rolls via conduction. Most of the mechanical energy is assumed to transform into heat.

The microstructural development of the slab is determined by the temperature of each element and the strain and strain-rate to which each is subjected. The strain is assumed to be parabolicly distributed through the thickness using:

$$\varepsilon_x = \varepsilon \cdot \left[1 + 1.76 \sqrt{\frac{h_f}{R_R}} + \left(\frac{x}{h_f} \right)^2 \right] \qquad (2.31)$$

Where ε_x is the strain at a fractional distance x/h_f from the centre of the stock. The recrystallisation kinetics is assumed to follow an Avrami-like equation using the temperature compensated time (equation 2.25). The recrystallised grain size after each pass (D_i) is calculated using equation 2.29.

The mechanical response is calculated using a sigma(Z)-equation of the form of equation 2.13. The stress strain curve is then calculated with a Voce equation. SLIMMER does not model any texture development.

Version 3.1 of SLIMMER [54] offers a choice of different materials to simulate. When a material is selected by the operator, the programme uses a specified set of equations. The only aluminium alloy available is Al-1Mg. The equations for this alloy (measured on transfer gauge material) were based on Puchi et al. [56] [57] and further refined by Beynon [58] [59]. The flow stress is calculated from:

$$\sigma = 1.155 \cdot \sigma^{SS} \cdot \left[1 - \exp(-C\varepsilon)\right]^{0.2} \tag{2.32}$$

With:

$$\sigma^{SS} = 8.20 \ln\left(\frac{Z}{5.5807 \cdot 10^{8}}\right)$$

$$C = 10 \ln\left(\left[1 - \left(\frac{\sigma^{0.05}}{\sigma^{SS}}\right)^{10}\right]^{-1}\right)$$

$$\sigma^{0.05} = 7.02 \ln\left(\frac{Z}{1.4565 \cdot 10^{9}}\right)$$

2.4.3.2 NTNU Model

Recently, a model was developed at NTNU in Trondheim, Norway by Nes and co-workers. This model is described in detail by Vatne [36]. The model predicts the microstructure and texture of a slab during and after multi pass rolling. The following assumptions apply:

(i) The recrystallisation texture is a result of oriented nucleation.

(ii) The final grain structure and texture are a result of the competition between growing grains that originate from a limited number of different types of site categories, where each site category has a density N_i.

(iii) Near site saturation nucleation kinetics applies.

(iv) The nucleation sites are randomly distributed in space.

(v) Johnson-Mehl-Avrami-Kolmogorov kinetics apply

(vi) During all deformation passes, steady state stress is reached.

(vii) The number and size distribution of the second phase particles is constant throughout the entire schedule.

From the first three assumptions it follows that it is necessary to calculate the number of nuclei of each category. The model uses three different categories: PSN, Grain Boundaries and Surviving Cube grains. The first two yield a random texture, while the surviving cube generates the cube fraction.

The amount of cube nuclei is given by:

$$N_C = \bar{\delta}_C \cdot A(\varepsilon) \cdot R_s \cdot (1 - R_C) \cdot S_C^* \tag{2.33}$$

Where $\bar{\delta}_C$ is the average cube subgrain size, A(ε) is the surface area per unit volume of cube grains of initial average size $\bar{D}$, that have undergone a deformation of strain ε.

The average cube sub-grain size is a function of the average overall sub-grain size described by equation 2.34.

$$\bar{\delta}_C = 1.3 \cdot \bar{\delta} \tag{2.34}$$

Where the overall sub-grain size is calculated from equation 2.19

From geometry considerations it follows that:

$$A(\varepsilon) = 2\left[\exp(\varepsilon) + \exp-(\varepsilon) + 1\right]\frac{R_C}{\bar{D}} \tag{2.35}$$

R_c is the instantaneous volume fraction of cube.

R_S is the volume fraction of S-texture, that is given by the empirical relationship:

$$\begin{aligned} R_S &= 0.04 + 0.17\varepsilon \;\forall\; \varepsilon < 2 \\ R_S &= 0.38 \;\forall\; \varepsilon < 2 \end{aligned} \tag{2.36}$$

It is assumed that this fraction also represents the fraction of cube that is surrounded by the S deformation texture component. It reflects the necessity for a cube grain to have an S neighbour to be able to form a nucleus.

Finally S_c^* is the density of subgrains inside the cube regions with diameters larger than a critical value δ^*. This value is given by:

$$S_C^* = \frac{1}{\bar{\delta}_C^3}\exp(-5a)\cdot\left[1+5a+\frac{1}{2!}(5a)^2+\frac{1}{3!}(5a)^3+\frac{1}{4!}(5a)^4\right] \qquad (2.37)$$

$$a = \frac{\delta^*}{\bar{\delta}_3}$$

Now a modelling parameter C_c is introduced, combined with equation 2.35 and 2.36, equation 2.33 becomes:

$$N_C = \frac{2C_C\bar{\delta}_C R_C(1-R_C)R_S S_C^*}{\bar{D}}\left[\exp(\varepsilon)+\exp(-\varepsilon)+1\right] \qquad (2.38)$$

The number of PSN-nuclei is calculated from the number of second phase particles with a diameter bigger than a critical value (η^*) times a modelling constant (C_{PSN})

$$N_{PSN} = C_{PSN}\int_{\eta^*}^{\infty} f(\eta)d\eta \qquad (2.39)$$

The minimum size for a particle to induce PSN is a function of the grain boundary energy (γ_{GB}), the driving force for recrystallisation (P_D) and the Zener-drag (P_Z).

$$\eta^* = \frac{4\gamma_{GB}}{(P_D - P_Z)} \qquad (2.40)$$

Furthermore, the distribution of all the second phase particles is characterised by the empirical equation 2.41.

$$f(\eta) = H\exp(-L\eta) \qquad (2.41)$$

Where H and L are characteristic particle size distribution parameters.

Where H and L are characteristic particle size distribution parameters.

Combining equations 2.39 to 2.41 and setting N_0=H/L the density of PSN sites becomes:

$$N_{PSN} = C_{PSN} N_0 \exp\left(-\frac{4L\gamma_{GB}}{(P_D - P_Z)}\right) \qquad (2.42)$$

A further source of randomly oriented nuclei is produced by subgrains near grain boundaries. The mechanism is analogous to that of the surviving cube grains. Only now the average value of the overall subgrain size is used since there is no extended recovery in randomly oriented subgrains. The total density of grain boundary sites is given by:

$$N_{GB} = \frac{2C_{GB}\bar{\delta}(1-R_C)S^*_{GB}}{\bar{D}}\left[\exp(\varepsilon) + \exp(-\varepsilon) + 1\right] \qquad (2.43)$$

The next step is to keep track of the number of nuclei during the complex situation of a partly recrystallised slab being rolled again. After the first step the situation is relatively simple:

$$N^1_{TOT} = N^1_C + N^1_{GB} + N^1_{PSN} \qquad (2.44)$$

Where the superscript ^{1} indicates that these nuclei arise after the first pass. However after the second pass the situation will be:

$$N^2_{TOT} = (1-X_1)\left(N^{1,2}_C + N^{1,2}_{GB}\right) + X_1\left(N^2_C + N^2_{GB}\right) + N^2_{PSN} \qquad (2.45)$$

Where $N^{1,2}_C$ refers to the cube regions that survived the first pass without recrystallisation, while N^2_C originates from cube areas that recrystallised after the first pass. The nuclei formed around particles are not affected by previous recrystallisation since their number is solely a function of the driving pressure after each pass (assumption vii).

The total number of nuclei after the n^{th} pass is thus given by:

$$N_{TOT}^{n} = N_{PSN}^{n} + X_{n-1}\left(N_{C}^{n} + N_{GB}^{n}\right) + \sum_{i=0}^{n-1}\left(X_{i} \cdot \left[\prod_{j=i+1}^{n-1}(1-X_{i})\right] \cdot \left[N_{C}^{i+1,\ldots,n} + N_{GB}^{i+1,\ldots,n}\right]\right) \qquad (2.46)$$

From assumption (v) it follows that the recrystallisation kinetics can be described as:

$$f_{i}(t) = 1 - \exp\left[-X_{ext}^{i}(t)\right] \qquad (2.47)$$

Where $X_{ext}^{i}(t)$ is the extended volume of the recrystallised fraction, defined as:

$$X_{ext}^{i}(t) = \frac{4}{3}\pi \cdot N_{TOT}^{i}\left(G_{i} \cdot t\right)^{3} \qquad (2.48)$$

In equation 2.48, G_i is the growth rate of the recrystallised grains. The grain size of the recrystallised grains is obtained from equation 2.30.

Above, only the main features of this model are discussed. A detailed description can be found in reference [36]. The model does not predict the temperature or the rolling loads during the rolling process. Also, the model is only applicable to the centre line of a rolled slab. It therefore does not have to take into account any distribution of strain and strain rate through the thickness.

2.5 *Concluding remarks*

From this literature review, the following conclusions can be drawn.

From the analysis of the industrial break-down process, it is clear that only limited data are available. Especially the temperature history of a slab is largely unknown. However, by using off line models like SLIMMER, it seems possible to derive a set of process parameters that describe the industrial situation quite accurately. To simulate this process in a laboratory situation, it is necessary that the geometry of each industrial pass is considered. To mimic the strain and strain-rate distribution through the thickness of the slab it is essential to consider the roll diameter of the industrial mill as well as the strain. Furthermore, it was found that it will be very difficult to mimic the friction conditions, since these are not known for the industrial situation. The best option seems to be to get the lubrication conditions as close as possible.

From the literature about the microstructural evolution it became clear that there is information available about a wide range of specific aspects. For instance the recrystallisation mechanisms associated with PSN have been studied in great detail. However, about the 'combined' microstructural evolution (second phase particles + (sub)grain size + texture), much less work has been done. This is especially the case when the material is subjected to a multi-pass deformation as normally done in industry. This is reflected in the available models which are largely empirical and/or focus on only a few aspects of the microstructure.

3. Experimental

3.1 Material

Most of the work in this project was carried out on AA3104 supplied by Hoogovens Aluminium Duffel NV (Material A). Table 2.3 shows the chemical composition of this material. For the break-down simulations the material was received in the as-cast condition and taken out of the centre of an industrial ingot. For comparison reasons, some break-down simulations were done on (commercial) material from a different supplier. This material is referred to as material B. Its chemical composition is also shown in table 2.3. Material B was also received in the as-cast condition.

Furthermore, some transfer gauge material (taken from an industrial break-down mill) was used to determine its sigma(Z) relationship. This material was also supplied by Hoogovens Aluminium Duffel NV and its chemical composition is identical to that of material A. The transfer gauge material was quenched within 2 minutes after the last break-down pass.

3.2 Laboratory mill rolling

So far, little work has been done on the physical simulation of break-down rolling of aluminium. This is partly because of the absence of a suitable technique. In this project a new technique has been developed to simulate this process. The Sheffield Mill for Aluminium Roughing at Temperature (SMART) combines large total reductions with a high maximum number of passes and a reasonable temperature control. Figures 3.1a,b and 3.2 show a photograph and a sketch of SMART. This installation is described below.

SMART is based on a conventional laboratory mill. Here, a 50 tonne Hille reversible mill was used. Table 3.1 gives the technical details of the mill [60]. It is equipped with a P.C.-based data-logging system that logs time, rolling speed, rolling load and the temperature of the specimen. To avoid too large data-files, these parameters are logged at two different logging rates [61]. During the inter-pass times a log-

frequency of 1 Hz is used. By pushing a button just before each pass, the fast logging (200 Hz) is activated. This way, it is possible to limit the size of the data-files without losing detailed information during the actual rolling.

During some of the experiments on SMART, a lubricant was applied to the mill. This was done with a lubrication system which consists of a sponge that is fitted on top of the top roll. The lubricant is an emulsion of 1 part oil and 3 parts of water. It is fed to the sponge from a squeeze bottle through a flexible tube. In this way there should always be more lubricant and thus less friction in between the top roll and the slab compared with the bottom roll. Therefore the slab should always tend to bend downwards rather than upwards. Since the table of the mill is directly adjacent to the bottom roll (figure 3.3), the slab will be straightened by the table, avoiding it to bend downwards.

One of the essential features of SMART is the possibility to control the temperature of the slab. This is done by two tube furnaces directly adjacent to the rolling mill (figure 3.2). In each furnace, a stainless tube has been inserted. Within these tubes a flat plate was welded, to enable the specimen to slide from the mill table into the furnaces.

Before the first pass, three Nichrome wires are attached to the slab as shown in figure 3.4. Using these wires the slab is pulled from one furnace through the mill into the other furnace. After each pass, the mill is reversed, set to its new gauge and then the slab is pulled back.

From figure 3.4, it is seen that two wires are attached to the 'head-end' of the slab, where the tail-end has only one (central) wire. The rationale behind this arrangement is that one operator can steer the slab while the other just has to provide enough tension in the wires. Figure 3.4 also shows that the slab is chamfered on one side to ensure that it will bite on the first pass. This configuration has been used for the majority of the experiments. However, the experiments on material B used a slightly modified design. This material was only available as a slab of 25 mm thickness. The initial thickness needed was 58.6 mm. Therefore a

tandem-configuration was designed (figure 3.5). Each slab consists of two pieces of metal side by side which are held together by an extra set of wires.

During rolling, the temperature of the slab is monitored via a thermocouple inserted in the centre. Because of the high total reduction, a conventional metal sheeted thermocouple (K-type, ø1.5 mm) cannot be used. The thermocouple itself would be squashed too much, causing it to short-circuit. To overcome this problem, the tip of the thermocouple is put into a stainless tube (I.D. 1.6 mm, O.D. 2.4 mm) to reinforce it. However, just sleaving the thermocouple is not enough to ensure a reliable temperature read out. During the deformation, metal flows around the tip of the thermocouple. When this tip consists of bare wires (as is the case when the thermocouple is re-welded upon its second and further use) , the wires will break. To avoid this problem, the tip of the stainless tube is filled with silver braze, thus protecting the wires of a 'used' thermocouple and ensuring good thermal contact between the slab and the wires (figure 3.6).

The slabs were heated from room temperature in a chamber furnace close to the mill (next to one of the tube furnaces, see arrow in figure 3.1a). After this, they were transferred into the first tube furnace. During this transfer the wires were attached to the slab. To limit the heat-loss during the transfer, the table on which the slab was put to attach the wires was insulated with an alumino-silicate fibre mat [62].

From practical experience, the optimal dimensions for the slabs were derived. To keep the length after the last pass as short as possible, it is desirable to start with the shortest length feasible. It turned out that the length of the slab had to be at least 1.2 times its thickness. Shorter slabs tended to roll rather than slide when pulled through the furnaces. The width of the slabs is governed by the dimensions of the tube furnaces. To ensure plane strain conditions, the slab should be made as wide as possible. It turned out that a width between 4 and 5 cm gave the best results.

3.2.1 Rolling schedules

In this work a range of rolling parameters was used. All the rolling tests can be summarised into 6 series. Series 1 is a 9 pass schedule, series 2a to 2d are 14 pass schedules with specific conditions and series 3 is rolled with a different mill having a different roll radius. Table 3.1 gives the technical details of this Robertson mill.

Table 3.2 shows an overview of the main parameters during all the rolling tests: These are discussed below

3.2.1.1 Series 1

Since there was no practical experience with SMART, a relatively simple schedule was used first. The objective of this test series was to gain experience with SMART. The initial tests were carried out, using a nine pass schedule that will be referred to as series 1. Table 3.3 shows the processing parameters for this schedule. The slabs were homogenised using the temperature history of figure 2.4 and subsequently air-cooled to room temperature before being reheated and rolled. During these experiments no lubricant was applied. The tube-furnaces were set at 750 °C. Figure 3.7 shows the temperature profile throughout the tube-furnaces at this set point. The centre region of the furnaces (695±15 °C) was used to reheat the centre of the slab during the inter-stand times.

3.2.1.2 Series 2

Once the experimental difficulties of SMART had been overcome, a second rolling schedule was derived. This schedule is based on industrial data taken from Vatne, Oscarsson and Ekström [63], [64]. From these data, the initial temperature, strain, strain-rate and mean zone-thickness/contact length ratio (Δ from equation 2.8 were used to calculate the laboratory schedule. This schedule was then used to do four series of experiments. Table 3.4 shows the general processing parameters for series 2a, 2b, 2c and 2d.

The objective of the first series of experiments with this schedule (Series 2a), was to mimic the industrial situation as closely as possible. Therefore, the homogenisation treatment was integrated. This is normally the case in industry where the homogenised slabs are transported to the rolling mill while still hot. In the laboratory this was done by homogenising the as-cast material in a chamber furnace near the mill (arrow in figure 3.1a) followed by a hot transfer to the tube furnace. Furthermore, a lubricant was applied to the mill. The tube furnaces were set at 750 °C. The microstructural development throughout the schedule was studied by quenching slabs at intermediate stages. The slabs were quenched after the inter stand time after the last pass. Also, the recrystallisation kinetics of the material after 10 and 13 passes has been determined. To do this, the material was quenched directly (within 10 s.) after the 10th and the 13th pass. Specimens from these tests were then annealed for different time spans in a salt bath at two different temperatures (330 °C and 450 °C).

Series 2b studies the influence of the homogenisation practice. To do this, the 14-pass schedule was applied to material that was homogenised, air-cooled and then reheated before rolling.

Series 2c looks at the influence of rolling temperature throughout the process. To change this parameter, the set point of the tube furnaces was altered to 650 °C. Again, the central zone was used for annealing. Figure 3.7 shows that the temperature in this zone was 580±15 °C. Some specimens from this series were quenched directly after the 13th pass to be able to study the recrystallisation kinetics.

Finally, the influence of chemical composition was studied (series 2d). To do so, some as-cast commercial material was obtained from a different supplier. This material was then rolled, using the same parameters as for series 2a.

3.2.1.3 Series 3

To check the validity of the spread equations derived from the SMART-results a short test series was carried out on another mill (for technical details, see table 3.1).

This Robertson mill has a different roll radius of 123.8 mm. The Robertson mill is a very simple, reversible rolling mill that can only be operated at one set speed. Table 3.5 shows the rolling parameters for this schedule (series 3). It must be noted that this mill is not equipped with any furnaces that are directly adjacent. The slabs were therefore heated up to 600 °C and then air-cooled to the rolling temperature of 550 °C. After each pass they were quenched. After measuring the dimensions, the slabs were reheated to 600 °C again and then rolled for the next pass. During the rolling no lubricant has been applied. No microstructural characterisation was carried out for this series.

3.3 Plane Strain Compression

The Plane Strain Compression machine as available at the University of Sheffield was used for the derivation of the constitutive equations. This machine has been discussed at length elsewhere [16] [56], hence only a short description is given here.

In figure 3.8a,b,c a schematic drawing of the main components of the Sheffield machine is shown. For a typical test, the specimen (①) is put into two arms (②) that are mounted on a trolley. The trolley is positioned in such a way that the specimen is in the reheat furnace (③) (this furnace can be rolled over a set of rails towards the trolley). Now the specimen is heated (typical heat up rate for an aluminium specimen is 2 °C/s) to the test temperature. The reheat furnace is then rolled back and the arms are put in line with the main furnace. Now the specimen is transported into the test furnace (④) (see figure 3.8c). To carry out a test, the top tool (⑤) comes down at a controlled speed, thus deforming the specimen. The speed is controlled in such a way that it is possible to deform the specimen at any given strain-rate profile. The deformation is stopped when the wedge (⑥) halts the top tool. The exact position at which this happens is controlled by the wedge position that is set for each deformation by the control software. The top tool then moves upwards again and the trolley moves backwards, transporting the specimen into the quench unit (⑦). Now the door of the quench-unit (⑧) closes and the specimen is sprayed with water until it is cooled down to room temperature. During the test, the

temperature of the specimen is logged from a metal sheeted thermocouple that is inserted in a hole in the specimen. This hole is drilled in the deforming centre of the specimen. Furthermore, the time, position of the top tool and the force are logged. Apart from the temperature of the furnaces, the temperature of the tools can be adjusted by means of tool-heaters that are inserted in both the top and the bottom tool. The dimensions of a standard specimen are 10*50*60 mm (h*b*l), the tools are 15 mm wide.

The experimental schedule for the derivation of the sigma(Z) equations is given in table 3.6. Each specimen was deformed to a true strain of 1.5. The strain rate was kept constant during the deformation.

Two types of material were used for these tests. Firstly, the material taken after 10 passes from series 2a on SMART was tested. Secondly, the sigma(Z) equation of the industrial transfer gauge material was determined.

3.4 Microstructural characterisation

The microstructure of the deformed and quenched specimens was analysed using several techniques. The grain structure was studied on specimens that were polished to ¼ μm and subsequently electro-chemically etched using Barkers' Etch (5 % HBF_4 in H_2O, 20 V, 3 min). The size and shape of the different grains was studied, using polarised light. From this, the fraction recrystallised was derived via point counting. When the fraction recrystallised was below 0.5, the spacing between points was chosen in such a way that the average number of points falling in any recrystallised colony did not significantly exceed unity. For higher fractions recrystallised, this rule was applied to the non recrystallised colonies. A minimum of 500 points was used per specimen. These were taken from 5 randomly selected areas at a specified depth below the surface. Each area was analysed with the aid of a grid that was inserted in the microscope, which made it possible to count a 100 points without having to move the stage. To fulfil all the requirements the magnification was adjusted according to the grain size.

The texture of the specimens was determined with a standard X-ray goniometer. The ODF's were calculated from four incomplete pole-figures {220}, {311}, {111} and {200}. From the ODF's the fraction of the main texture components was calculated using the software developed by Van Houtte [65]. The components were allowed to deviate 16.5° from the ideal orientations.

The conductivity was measured with a Sigma-tester [66], using a frequency of 480 Hz. All measurements were done in the centre region of each specimen.

Finally the second phase particle distribution of some selected samples was determined using scanning electron microscopy. The polished samples were analysed in a JEOL 840 SEM interfaced to a LINK image analyser. The SEM image appeared on a 90 X 90 mm^2 CRT screen with 1024 * 1024 pixels. The outcome from this investigation was the area of each particle, the total particle area fraction and the average aspect ratio of the particles. These 2D results were than corrected to represent 3D situation. This was done with the Schwartz-Saltykov analysis (described by Underwood in [67]) as programmed by Furu [48].

4. Results

4.1 On-line measurements

During each experiment on SMART the time, temperature and load are measured. Figure 4.1a and 4.1b show a typical output for a 9 and a 14 pass experiment from series 1 and 2a respectively. The temperature and the rolling loads are plotted as function of the time.

Figure 4.2 shows the temperature profile from a 13 pass experiment from series 2c (lower furnace set-point) as well as the temperature profile from series 2a. This specific specimen from series 2c was quenched directly after the last pass (in this case after the 13th). It is seen from this figure that such a procedure takes only a few seconds after the last deformation.

More details about the specific temperature histories that are shown in figure 4.1b and 4.2 are given in chapter 4.5: "Modelling results".

In figure 4.1b it is seen that some passes (pass no. 8, 10, 11, 13 and 14 in figure 4.1b) have generated none or very little load signal. This happens when the fast logging system has been started too early or too late, thus missing the actual deformation. However, by combining the results of different experiments a load value for each pass has been deduced. From those values, the specific roll force per unit width for each pass i (F^i_{spec}) was calculated using equation 4.1.

$$F^i_{spec} = \frac{F^i_{roll}}{b^{contact}} \qquad (4.1)$$

In this equation $\overline{b^{contact}}$ is the average length of the contact line between the sample and the rolls, during the pass. How $\overline{b^{contact}}$ is obtained is discussed below. Table 4.1 shows the values for the specific roll forces.

However, because of the experimental set up, $b_{end}^{contact}$ (which equals $b_{begin}^{contact}$ for the next pass) is difficult to measure since the specimen is in the furnace. To obtain a value for $\overline{b^{contact}}$ a model was used. This model (equation 5.9) is described in more detail in chapter 5.10. The fit parameters for this model were acquired by measuring $b_{end}^{contact}$ of all the specimens after they were quenched. This was done by measuring the width of the surface that had touched the rolls (see figure 4.3). Figure 4.4 shows the results of these measurements. The data for figure 4.4 were taken from the results of four of the five experimental schedules (series 1, 2a-c, 3). Only the data from series 2d (different chemical composition) were not taken into account. The rather special way, these specimens were machined, is believed to influence the lateral spread in such a way that non representative data are generated from these tests. Therefore, this series has been completely excluded when discussing the lateral spread phenomena. For the same reason, the rolling loads measured during series 2d were not used in the calculation of the specific roll forces.

In figure 4.4 the results of series No. 3, the seven pass schedule on the Robertson mill are shown as a separate series.

4.2 Gauge control

As it is in industrial rolling, gauge control is a problem on the laboratory mill. Especially since the Hille mill is not equipped with an on-line gauge displacement transducer, it is not possible to get on-line information about the distance between the rolls during each pass. The only possibility to obtain this information is by measuring the height of each specimen before and after each experiment. However, this only works accurately for single pass experiments. To get an idea about the accuracy of the gauge control during multi pass SMART experiments, the final thickness of each specimen was compared with the value prescribed by that schedule. It was found that there was no systematic error and that the values showed a standard deviation of 0.17 mm.

4.3 *Characterisation of microstructure*

To study the microstructure of the material during the break-down process, specimens have been quenched at intermediate stages. In the following sections, the microstructure is often displayed as a function of "Pass number" or "Cumulative strain". "Pass number" should be understood as the last pass the specimen has undergone including the inter-stand time after that pass. This means that the results for pass number x represent the microstructure just before the slab would have been deformed for the $(x+1)^{th}$ time if the rolling process had not been interrupted. When x is the final pass, the structure as it would have gone into the tandem mill is quenched. For "Cumulative strain" the same explanation should be followed where the strain is calculated using equation 2.2, with h_f being the final thickness of that specimen.

The results of the microstructural analyses are discussed below. Tables 4.2 to 4.6 show an overview of all the microstructural features that were measured for the different experimental series.

4.3.1 Resistivity

Figure 4.5 shows the resistivity results for the series 2a. Figure 4.6 shows the resistivity measurements for series 2b (separated homogenisation, 14-pass), the eye lines from figure 4.5 are also included. Series 2d (different chemical composition, 14-pass) and the eye lines are shown in figure 4.7. Finally the results from series 1 (9-pass) and 2b are shown in figure 4.8. Since two different pass schedules are compared in this figure, these data are displayed as function of total strain rather than pass number.

4.3.2 Texture

From the nine-pass schedule (series 1), the texture on the centreline has been measured. Figure 4.9 shows the ODF after 9-passes. From each ODF the fraction of the different texture components has been calculated using Van Houtte's software [65]. Figure 4.10 shows the volume fraction of the S-component as it was

calculated by this software. There was no systematic development in the Cube component. This fraction was constant around a level of 0.05 ± 0.01.

Figure 4.11 and 4.12 show the volume fractions S and Cube as a function of pass number for the series 2a,b,c,d.

4.3.3 Optical microscopy

The main result from the investigations with optical microscopy consists of the recrystallised fractions of the slabs throughout the different stages of the rolling schedule.

Figure 4.13 and figure 4.14 show the fraction recrystallised as function of the scaled depth below the top surface. This parameter is calculated by dividing the depth below the top surface by the total thickness of the specimen, i.e. figure 4.13 shows significant asymmetry about the centre line.

Figure 4.15 shows the data of all the specimens that were quenched after x-passes plus inter-stand time.

Furthermore the recrystallisation kinetics of the material directly quenched after 10 and 13 passes for series 2a and directly quenched after 13 passes for series 2c was determined. When the 10 pass material was annealed up to 60 000 s, at a temperature of either 330 °C or 450 °C, no recrystallisation was observed.

Figure 4.16 shows he Avrami curve of the 13 pass material from series 2a, which was quenched directly and then salt bath annealed at 330 °C. The curve for 'the series 2a material' can be described with t_{50}= 1.1 10^4 s and n=0.45.

Annealing '13 pass, series 2a material' at 450 °C, resulted in recrystallisation kinetics that were too fast to be measured in this way.

Figure 4.16 also shows the Avrami curve from the material that was quenched directly after 13 passes of series 2c (rolling schedule at a lower temperature). This curve can be described with t_{50}= 89 s and n=0.83.

Figure 4.17a and 4.17b show the grain structure of the material from series 1a, after 0 and 9 passes.

For series 2a, figure 4.18a,b,c shows some typical microstructures after 5, 10, 12 and 14 passes. The initial grain structure of this series is identical to that shown in figure 4.17a

4.3.4 Size and size distribution of the constituents

The second phase particle distribution of some selected samples was determined using scanning electron microscopy. In figure 4.19ab, 4.20ab and 4.21a the constituent particles after 0, 10 and 14 passes are shown for series 2a and 2d. It must be noted that any Mg_2Si will not be visible in these pictures. By analysing a minimum of 1000 particles for each sample, a size distribution histogram was determined. From these histograms, the values of $\bar{\eta}$, H, L and N_0 from equation 2.41 were calculated. Table 4.7 shows these parameters for the measured samples.

4.4 Plane Strain Compression tests

The on-line output of the plane strain compression machine contains time, temperature, load and displacement. These data have been combined using the algorithms described by Silk and van der Winden [68] to obtain the equivalent stress-equivalent strain graphs (A copy of reference [68] can be found in appendix B). By doing this, the data are corrected for lateral spread and friction. The deformational heating increases the temperature of the specimen during a test. Therefore, it is not correct to assume iso-thermal conditions. To calculate iso-thermal stress-strain curves, the measured stress levels have been corrected using equation 4.2 [69]

$$\sigma^{nominal} = \sigma^{test} + \frac{Q_{def}}{\beta_0 R}\left(\frac{1}{T^{nominal}} - \frac{1}{T^{test}}\right) \qquad (4.2)$$

Where σ^{test} and T^{test} are the experimental values of stress and temperature of each data point. Q_{def} is the activation energy for deformation (156000 J/mol) and R is the

universal gas constant. Furthermore, β_0 is found from curve fitting the exponential law sigma(Z) equation (equation 2.12) to the instantaneous values of Z and σ.

Now the iso-thermal, equivalent stress versus the equivalent strain can be calculated for each test. A typical example of this is shown in figure 4.22. From the results of all the plane strain compression tests, table 4.8 and 4.9 were derived, which show the steady state and ε=0.1 stresses for all testing conditions. Figure 4.23 illustrates these data. They were then used to fit the empirical Sigma(Z) equations (equation 2.12 and 2.13) The results of this exercise are shown in table 4.10 for both the 10-pass and the transfer gauge material. Table 4.11 shows the same results for ε=0.1.

4.5 *Modelling Results*

In table 4.12 the input parameters used by SLIMMER for the industrial situation are given. The thermal history of this run of SLIMMER is seen in figure 4.2. From this figure it is seen that the model predictions of SLIMMER differ considerably from the measured temperature history for series 2a. Therefore, it does not make sense to use the roll force predictions of this run of SLIMMER. To obtain more meaningful roll force predictions, each individual pass was simulated on SLIMMER separately. The input that was used for these runs is taken from table 3.4. However, the version of SLIMMER that was used for this work only comprises Al-1Mg and its constitutive equation. To be able to compare the SLIMMER results of Al-1Mg with the SMART measurements on AA3104, the roll force predictions have been adapted. This could be done easily, since the constitutive equations of both alloys are known (equation 2.32 and table 4.10). This enables us to calculate the ratio between the average flow stress of Al-1Mg and of AA3104. Now a SLIMMER prediction can be obtained for AA3104 by multiplying the Al-1Mg results with this ratio. Table 4.1 shows the results of this exercise.

Table 4.13 shows the modelling constants for the NTNU-model. These were all derived from AA3004/AA3104 data from the literature. The rolling parameters for this model were taken from table 3.4. It must be noted that the NTNU-model assumes the annealing temperature after a pass to be the same as the deformation temperature of that pass. Since the annealing temperature is more important for the NTNU model, this temperature (from table 3.4) was also used as deformation temperature.

From the SEM results (figures 4.19ab, 4.20ab, 4.21a) it is seen that the size distribution of the second phase particles in the slab is (quantified by the parameters H and L of equation (2.41)) is not constant during the entire rolling sequence. However, the model assumes this to be the case. To see how sensitive the model predictions are to the evolution of the second phase particles, the model was run twice more using the data of series 2a. However, for each run a different set of values for H and L was used. The first run of the model used the 'As

homogenised' parameters. The predictions of this run are represented by the red bars in figure 4.24. The second run (the blue bars in figure 4.24) used H and L as they were measured from the material after 14 passes.

The output of the model for these two conditions is shown in figure 24-a,b,c. It must be noted that the recrystallised grain size (figure 24-b) is set to zero if no recrystallisation occurred.

5. Discussion

5.1 Introduction

The discussion of the present work is split into two sections. First all the experimental results will be discussed. This is then followed by a discussion that deals with the validation of the two computer models that were used in this work: SLIMMER and the NTNU-model.

The first section is structured as follows. First the chemical compositions of the present alloys are compared with those found in the literature. This is followed by a discussion about the temperature profiles and rolling loads that were measured during the experiments on SMART. Then the mechanical behaviour of the material as measured during the PSC tests is discussed. This is followed by a discussion about the different aspects of the microstructural evolution of the material during break down rolling. Finally the lateral spread of the specimens during rolling is discussed.

The second section starts with a comparison of the SLIMMER predictions with the experimental results as far as the temperature history and the rolling loads are concerned. Then the NTNU-model is validated against the present experimental results.

5.2 *Chemical composition*

Table 2.3 shows the limits for AA3104 and AA3004 as prescribed by the Aluminium Association [18]. It is seen that the difference between these alloys mainly lies in the limits for Si and Mn. When the literature is studied, a wealth of chemical composition data, measured from material produced by the different aluminium manufacturers can be found. These are also shown in table 2.3. It must be noted that these compositions do not necessary represent the commercial compositions as produced today. However, from table 2.3, it becomes clear that there is very little difference in the actual chemical compositions. Also the label 3004 or 3104 does not indicate any difference in chemical composition. Apart from the chemical composition, very little information is normally given about the processing parameters. Therefore, it can be expected that the differences in properties of 3104 from different suppliers (or even different batches) are not smaller then the difference between 3104 and 3004. This leads to the conclusion that it is allowable to compare the literature values of 3104 and 3004 with each other.

5.3 *Temperature histories*

One of the parameters that needs to be mimicked carefully when simulating hot rolling, is temperature. The control of temperature is a key aspect of SMART. Figure 4.1a shows the temperature history as measured from series 1.

The objective of series 2a,b,c,d was to simulate the industrial process. Therefore, it would have been best to use temperature measurements from industry as the target. However, such measurements were not available. Instead SLIMMER was used to simulate the industrial rolling schedule, thus providing a temperature-time curve that was used as the target for the SMART experiments. This target is shown in figure 4.2, where the red line represents the output of the SLIMMER simulation using the industrial process parameters.

Setting the tube furnaces at 750 °C, the blue temperature history in figure 4.2 was logged for a 14 pass experiment. It is clear from this figure that both the roll-quench during deformation and the heat-up rate during the inter-stand time increase with pass number. This is caused by the decrease of the thickness of the specimen, thus reducing the thermal mass per unit length. Apart from this effect, figure 4.2 also shows some more irregular features. For instance between pass 9 and 10, the temperature is almost stable. This occurs when the specimen is taken to the end of the furnace in order to rotate it around the RD-axis (why this was done is explained in section 5.5). This 'flip' was carried out after each 7^{th}, 9^{th}, 11^{th} and 13^{th} pass. Occasionally it did not go as smoothly as hoped, resulting in a low heat-up rate. After pass number 13 and 14 the temperature levels out at 500 °C. This is caused, by a deliberate move of the centre of the specimen to the edge of the hot-zone. This was done to avoid overheating and possible melting of the specimen.

Comparing the red (SLIMMER-target) and the blue (measured history from series 2a) with each other, it is seen that the experimental temperature lies below the target for the first 12 passes. During the inter stand time between pass 12 and 13, the specimen heats up so much that its temperature rises above the target value.

The data for the green line in figure 4.2 are also measured during an experiment using SMART. However, the experiment that is represented is a 13 pass experiment where the furnaces were set at 650 °C (series 2c). This resulted in a slower heat-up during the inter-stand times, yielding a lower temperature profile. In this test, the temperature at the 13th pass stays below the target value. It may therefore be expected that the industrial microstructure after 13 passes lies in between that from series 2a and 2c.

5.4 *Sigma(Z) behaviour*

Table 4.10 shows the results from the fitting of equation 2.12 and 2.13 to the steady state flow stress that were measured on the PSC-machine for both the 10-pass and the transfer gauge material. These results are graphically represented in figure 5.1.

It is seen from figure 5.1 that both equation 2.12 and equation 2.13 describe the present results equally well. However, a disadvantage of equation 2.12 is that if extrapolated to very low values of Z (ln Z < 20), it results in negative values for the steady state flow stress. Equation 2.13 does not suffer from this since it cannot become smaller than 0 for any value of Z.

From table 4.10 and figure 4.23, it can be concluded that the Sigma(Z) behaviour of the steady state stress of the 10-pass material is not significantly different from that of the transfer gauge material.

Especially during the first passes of break-down rolling, even the average strain per pass is not high enough for the material to reach steady state. Because of the inhomogeneous strain distribution through the thickness, the strains at the centre line of the material will be even lower. Therefore it is not sufficient to consider just the steady state flow stress to characterise the mechanical behaviour of the slab during break-down rolling. To get an idea about the mechanical behaviour at low strains, equation 2.12 is applied to ε=0.1. This value was chosen since it is the lowest strain at which the experimental problems associated with measuring low strains in a compression machine can be avoided (for more details about this see appendix B [68]).

Table 4.11 shows the values for $\beta_2^{0.1}$ for both the 10 pass and the transfer gauge material. It can be seen that the differences between these values are even smaller than those found for the steady state parameters.

Table 4.10 and 4.11 also show some parameters for equation 2.12 that were found in the literature (Andersson et al. [64] and Castro Fernandez et al. [46]). All the results from table 4.10 are graphically illustrated in figure 5.2. It is seen that the

differences in parameters from the different authors do not yield very different flow stress predictions.

Andersson used a rolling schedule that is similar to the present 14-pass schedule and therefore his results can be integrated with the present ones. It is seen that his results confirm that the steady state stress of the material does not change significantly throughout the break down schedule.

Figure 5.2 also shows the model predictions for the steady state flow stress that are taken from Gelin et al. [70]. They use an equation that is somewhat similar to equation 2.13.

$$\sigma = \frac{108.3}{\left(1+\frac{\exp(32.84)}{Z}\right)^{0.21}} + 70\,\mathrm{arcsinh}\left(\frac{Z}{\exp(40.2)}\right)^{1/9.6} 1.3\sqrt{\left[1-\exp\left(-\frac{103.5}{\sigma^{ss}}Z^2\varepsilon\right)\right]} \qquad (5.1)$$

It must be noted that these authors use a uncommon simplification when defining the Zener-Hollomon parameter. Rather than $Z = \dot{\varepsilon}\exp\left(\frac{Q_{def}}{RT}\right)$, they use $Z = \dot{\varepsilon}\exp\left(\frac{Q'}{T}\right)$. Q' is set to 21000. When these results are calculated back to the normal definition of Z, this means that Gelin uses a value for Q_{def} of 21000*8.313= 174 kJ/mol. The results shown in figure 5.2 have been corrected for this, to make them comparable with the other data that apply Q_{def}=156 kJ/mol. It can be concluded that this model predicts comparable values for the steady state flow stresses for the Z-values considered.

From table 4.11 it is seen that the parameters for equation 2.12 that were found for the present work for ε=0.1 do not agree as well with those from Castro-Fernandez [46]. This may be caused by the differences in the fraction recrystallised of the material that was studied in both projects. In the present work, both the 10 pass and the industrial transfer gauge were 20% recrystallised before the PSC-testing. From

the non-deformed shoulder, it could be concluded that this fraction had not changed during the reheating to the test temperatures. Castro-Fernandez used fully recrystallised material to perform his PSC-testing. This difference will result in relatively large differences in stress-strain behaviour upon low strains. When the stress gets closer to steady state, the influence of the initial microstructure will decrease. Another factor that could contribute to the difference in the parameters for ε=0.1 are the experimental difficulties associated with measuring stress values during PSC-testing at low strains.

5.5 *Recrystallised fraction*

The recrystallisation phenomena from the present work, are discussed from three viewpoints. Firstly the recrystallisation within one single specimen is discussed. The fraction recrystallised as a function of the depth below the surface is studied. Then the bulk values of the fraction recrystallised of all the specimens of the different series are compared with each other. Finally, a closer look at the recrystallisation kinetics of some selected samples is made.

Figure 4.14 shows a typical profile of the fraction recrystallised of a partly recrystallised sample taken from SMART. On the x-axis of this figure the scaled depth below the surface is plotted. It is seen that both the top and the bottom surface are fully recrystallised, but much less recrystallisation occurred in the central region of the sample. This can be understood from the slip line field analysis of break-down rolling (see figure 2.6). It is seen that the local strain during break-down rolling is distributed in-homogeneously through the thickness of the slab. The areas near the top and the bottom surface are sheared much more than the area around the centre line. Even when there is no friction between the mill and the slab, the strain path at the surface will be different compared with the centre. With higher (more realistic) friction conditions, an extra shear becomes superimposed upon the compression deformation. Besides the effect of the strain distribution, there is also an effect of temperature distribution. This is caused by the chill effect that the rolls exhibit upon the slab. This means that the surface will chill during the deformation. Therefore it is deformed at a lower temperature compared with the centre of the sample. This means that in the slabs from an industrial mill and those from SMART, the surface areas will have the biggest driving force for recrystallisation and thus recrystallise faster than the centre of the slab. Upon subsequent annealing, the centre region of the slab 'catches up' with the surface regions, with increasing time.

The results from figure 4.14 represent a partly recrystallised structure, where the centre is 20% recrystallised. It is seen that the profile is symmetrical

around the centre line. In figure 4.13, a profile of a specimen that has undergone fewer passes (8 rather than 11). This figure shows a profile that is not symmetrical at all. It turned out that the recrystallisation kinetics was reproducibly faster at the top of the slab compared with the bottom. An explanation for this must be found in some asymmetry in the deformation conditions of SMART. The biggest asymmetry in the specimen is the chamfer that is machined on the head end of the slab (see figure 3.4). However the asymmetry in recrystallisation kinetics occurred to the same extent towards the head as towards the tail end of the slab. Also, experiments where the slab was chamfered on both the top and the bottom showed the same asymmetry. Therefore it is believed that the chamfer is not the cause of the asymmetry in recrystallisation kinetics.

Also, different friction conditions between the top roll and the slab compared with the bottom roll could also cause the bending. If the coefficient of friction on the top side would be much higher compared with the bottom, then this would result in much more localised deformation in the top half. This could then result in a faster recrystallisation near the top surface of the slab. The coefficient of friction is controlled by: the lubricant, the surface condition of the slab and by the surface condition of the rolls. The lubricant is fed from the top (see figure 3.2 and 3.3). Assuming that the coefficient of friction will decrease with the amount of available lubricant makes it unlikely that the lubricant would cause the top roll to have a higher coefficient of friction. The surface quality of the slabs was completely symmetrical and therefore this cannot explain the asymmetry.

This leaves the surface quality of the rolls. From visual inspection, no difference in surface quality could be detected. Also the hardness of both rolls was the same. However, it could be that a more detailed study of the rolls could result in some asymmetry. It was decided that this is beyond the scope of the present research.

Another factor that could influence the distribution of the recrystallisation kinetics through the thickness of the slab is the temperature distribution. Just

before and directly after the deformation, it slides over the cold tables (see figure 3.3). This results in some heat loss towards the bottom that will be bigger than the heat loss to the air that surrounds the top half. Therefore the local deformation temperature could be somewhat lower at the bottom. A further temperature gradient could be introduced by the difference in heat transfer coefficient as a consequence of different lubrication conditions between the top and the bottom roll. This effect could cause an asymmetry in the chill effect of the rolls which might explain the bending. Since the temperature was only measured on the centre line, the present experiments do not provide enough information to judge whether this effect is strong enough to explain the bending. However, more research is necessary to determine whether this temperature effect is big enough to explain such a dramatic asymmetry in the evolution of the microstructure.

It is concluded that no satisfying explanation is yet found for the asymmetry in recrystallisation kinetics and more research in necessary. However, this asymmetry resulted in a very big experimental difficulty. As soon as the specimen started to recrystallise from the top surface, it also started to bend upwards. This even resulted in a specimen being wrapped around the top roll. To overcome this problem, the following solution was implemented. For all experiments of series 2a,b,c,d the specimen was rotated around its longitudinal axis after the 7^{th}, 9^{th}, 11^{th} and 13^{th} pass. This resulted in a symmetrical microstructural evolution and stopped the specimen from bending upwards.

The next viewpoint from which the recrystallisation has been studied, is the fraction recrystallised with which the slab enters the next pass. Series 1 showed no detectable recrystallisation for any of the passes. This is caused by the relatively low temperature of the schedule in combination with the low reductions per pass.

Figure 4.15 shows the recrystallised fractions for series 2a,b,c,d. It must be noted that the measurements for this figure were taken at a scaled depth between 0.4 and 0.6 for all the specimens. There were no samples taken

before the fifth pass for any of the series. However, by relating the grain-thickness (measured in the ND direction) to the total reduction, it could be concluded that no recrystallisation occurred in between any of the first five passes. Furthermore, the results from all the four series using the 14 pass schedule are very similar. This suggests, that neither the two chemical composition, nor change in homogenisation treatment, nor the difference in rolling temperature influence these results very strongly. For all these series, severe recrystallisation starts after the tenth pass where a sufficient cumulative strain is combined with a long enough inter pass time at high enough temperature. However, this result does not necessarily mean that the recrystallisation kinetics of the material is the same for each series.

From a modelling point of view it is necessary to know the recrystallisation kinetics throughout the rolling sequence. To investigate this, some selected samples from series 2a, were quenched directly after the 10^{th} and the 13^{th} pass. For these samples the recrystallisation kinetics were determined using salt bath annealing.

It was found that the 10-pass material does not recrystallise within 60 10^3 s (= 16 hours and 40 min) even at 450 °C. This means that it can be expected that the texture of the slab does not change during this period either. The industrial relevance of this result is that an extended inter-stand time at this stage of the production process (for instance due to a malfunction in the finishing mill) should not influence the microstructure of the final product. It must be noted that this conclusion is only valid if such an interruption does not influence the rolling temperature of any subsequent passes.

When annealed at 330 °C, the 13-pass material does start to recrystallise within a short period after the last pass (see figure 4.16). When comparing the 10-pass material with the 13-pass material, it could be concluded that the recrystallisation kinetics of the material changes dramatically. However, from equation 2.23 it is seen that the time for 50% recrystallisation is not only a function of the annealing temperature but also of the initial density of nuclei and the deformation conditions. These factors can be summarised as the

driving force for recrystallisation. From table 4.3 it can be concluded that from the 10 pass material, only a small fraction has recrystallised during its history. This means that the driving force for recrystallisation has only been reduced via static or dynamic recovery. If one assumes all the material to be sufficiently recovered during the deformation (i.e. no static recovery), it can be concluded that the driving force does not decrease during the inter-stand times of the first 10 passes. Therefore, the total driving force can be estimated by assuming the total reduction of all 10 passes to have happened during one pass. The strain of this pass ($\varepsilon_{1\text{-}10}$) is the sum of the first 10 passes. The average values for the strain rate ($\overline{\dot{\varepsilon}_{1-10}}$) and the temperature ($\overline{T_{1-10}}$) can be calculated by using the fraction $\varepsilon_{1\text{-}10}$ as weight factors. For $\overline{\dot{\varepsilon}_{1-10}}$, equation 5.2 applies.

$$\overline{\dot{\varepsilon}_{1-10}} = \frac{1}{\varepsilon_{10}} \cdot \sum_{i=1}^{10} \varepsilon_i \cdot \dot{\varepsilon}_i \qquad (5.2)$$

An analogue equation applies to the temperature and from these two parameters the average Z-value can then be calculated.

It is seen from equation 2.23, that that the time for 50% recrystallisation not only depends on the deformation conditions, but also on the grain size of the material. To calculate this parameter for the imaginary 1-10 pass is not very straight forward. It could be assumed that in the absence of recrystallisation or the formation of transition bands [30], the total number of grains (and thus the grain size) is constant.

For the 13 pass material, the situation is rather different. This material was almost fully recrystallised before it entered the roll gap for the 13th time (see table 4.3). Therefore, the accumulated driving force just before the 13th pass can be assumed to be zero. This means that only the deformation conditions of the 13th pass need to be considered.

Table 5.1 shows the deformation conditions for the 1-10 pass and the 13th pass. It is seen from this table that the faster recrystallisation of the 13 pass material can only be explained if the dependency of the (temperature

compensated) time for recrystallisation upon Z is much stronger than its dependency on ε. In the literature [52] the power for the Z-dependency is reported to be -0.783 (=A_3 in equation 2.28) for AA3004. No data were found for the dependency upon the strain. The nearest alloy for which the strain and Z dependency was determined is Al-1%Mg. Sellars et al. [71] found for this alloy

$$t_{0.5} = 9.8 \cdot 10^{-6} \cdot Z^{-1.1} \cdot \varepsilon^{-2.7} \cdot d_0^{1.35} \cdot \exp\left(\frac{230000}{RT}\right) \qquad (5.3)$$

Assuming equation 5.3 to be applicable to the present results, a decrease in strain from 1.64 to 0.39 yields a $t_{0.5}$ that is 24 times slower. Increasing Z from 9.82 10^{10} to 1.55 10^{12} yields a $t_{0.5}$ that is 20 times faster. The net result predicted by equation 5.3 would be that the 10 and the 13 pass material would have a very similar $t_{0.5}$. The present experimental results do not agree with this prediction.

This could be caused by the assumption that the influence of the grain size can be ignored. In the present work the initial grain size is 140 μm. After 13 passes this is reduced to 67 μm. From equation 5.3, it can be concluded that a 50% change in grain size can change $t_{0.5}$ by a factor of 10. The $t_{0.5}$ of the 10-pass material is several orders of magnitude slower than the $t_{0.5}$ of the 13 pass material. Furthermore, assuming the average grain size of the 1-10 pass to be equal to the as cast grain size can only result in a lower bound solution for $t_{0.5}$. It is therefore be expected that the real influence of the grain size on the recrystallisation kinetics is much less. Hence it can be concluded that the change in grain size cannot explain the difference in $t_{0.5}$ of the 10 and the 13 pass material.

An explanation of this could be that the coefficients for AA3104 differ greatly from those of Al-1Mg. The manganese present in AA3104 will affect the recrystallisation kinetics. However, it is not expected that the manganese will affect the ratio between the grain size, strain and the Z dependency of the recrystallisation kinetics.

Another explanation could be found by looking at the recovery mechanisms that occur. In the discussion above it was assumed that no static recovery occurs. Reyes et al. [37] found that this assumption is not necessarily correct and that for hot rolling conditions, up to 20% of the retained strain (i.e. retained dislocation density, from which the driving force for recrystallisation is derived) can 'disappear' due to static recovery. Static recovery occurring during the inter-stand times of the first 10 passes could very well explain the much slower recrystallisation kinetics of the 10 pass material. However, more research is necessary to confirm this hypothesis.

In figure 4.16, the recrystallisation kinetics of the slabs taken after 13 passes from series 2a and 2c can be compared. The material from series 2c was rolled at a lower average temperature throughout the schedule (see figure 4.2). It is seen that this shortens t_{50} by two orders of magnitude. This can be explained from the driving force that is generated during the deformation. When this deformation occurs at a lower temperature, the material will be stronger and therefore more work is put into the material. This yields a higher driving force for recrystallisation and thus faster recrystallisation kinetics.

In the literature several sets of data are available for the recrystallisation kinetics of AA3104 in transfer gauge. Brand et al. [52] determined the recrystallisation kinetics from double deformation tests (uni-axial). They analysed their results using the principle of the temperature compensated time. Figure 5.3, shows the Avrami curve which can be deduced from their data for an annealing/deformation temperature of 330 °C and a deformation at a strain rate of 8.3 s^{-1} (i.e. the deformation conditions of the 13th pass). In this figure the Avrami curve as derived by Belling et al. [72] for this alloy under the same conditions is also shown. Finally the recrystallised fractions as measured by Daaland [29] for 3004 after the last hot rolling step (i.e. after finishing) are shown. By comparing these three data sets with each other, it can be concluded that all these values although derived from alloys of different suppliers and measured in different ways, are quite comparable. Comparing these literature data with the present experimental results, it can be concluded that the results from series 2c are in good agreement.

5.6 *Resistivity measurements*

The rationale behind measuring the resistivity of the specimens is found in its relationship to the amount of dissolved elements. Altenpohl [73] found a relationship between the resistivity and the amount of dissolved iron, manganese, silicium and magnesium. This relationship is of the form of equation 5.4.

$$R = 0.0267 + 0.032 \cdot [Fe] + 0.033 \cdot [Mn] + 0.0068 \cdot [Si] + 0.0051 \cdot [Mg] \quad (5.4)$$

Where R is the resistivity and the square brackets indicate the amount of dissolved elements. The factors for the different elements have been refined since the original work of Altenpohl in 1965. The factors shown in equation 5.4 are taken from Trømberg [74].

From equation 5.4 it is seen that the precipitation of Mn and Fe atoms will have the strongest influence on the resistivity. When it is assumed that no precipitation of iron containing particles occurs, equation 5.4 can be used to follow the manganese precipitation.

In this work the relative amount of dissolved Mn is of more interest then the absolute value. Therefore all results are discussed in terms of resistivity values without applying equation 5.4.

In table 4.2 the results from the resistivity measurements from series 1 are shown. These measurements gave excellent reproducibility. The standard deviation within one specimen after 7 passes was 0.11% (3 measurements at different positions), while that of the average of 4 specimens after 7 passes, *i.e.* 12 measurements, was 0.15%. Table 4.2 shows that the resistivity gradually decreases which indicates that the solute content decreases with increasing number of passes. This is in agreement with Sheppard [75], who found for a 3003 (Al-1Mn) alloy, 0.45 wt.% Mn is still in solution after homogenisation. After industrial hot rolling, he found that only 0.34 wt.% manganese was still in solid solution. However, series 1 does not mimic a complete industrial break-down schedule.

Series 2 does mimic a complete break-down schedule. The resistivity results of series 2a are shown in table 4.3 and figure 4.5. It is seen that the resistivity measurements show considerable scatter. It is not quite clear where this originates from since no correlation was found between the scatter and deviations in the experimental conditions of individual specimens. However, with linear regression analysis a trend line was found, which is also shown in figure 4.5. From this, it can be concluded that the resistivity decreases with pass-number, indicating precipitation during the break-down rolling. Figure 4.3 also shows the results from the full scale trial [64] on which the SMART 14-pass schedule was based. These results indicate much less precipitation as the resistivity only slightly decreases with pass number. This difference might be explained either because of differences in chemical composition or homogenisation treatment. Especially the amount of iron in the material in the full scale trial, is much higher (see table 2.3, Gränges material). From equation 5.12 it is seen that this will influence the resistivity strongly. However, assuming that a higher content of iron and manganese can only yield higher values for [Fe] and [Mn], an explanation for the lower resistivity cannot be found in the chemical composition of the alloy. That leaves the homogenisation treatment as possible cause for the lower values. The exact homogenisation treatment for the full scale trial is not known. Therefore, no conclusive evidence can be found for the difference in resistivity level between material A and that used by Andersson [64]. However, the lower slope of the line for the industrial data can be understood, since a lower level of supersaturation in the as homogenised material will result in a lower driving force for precipitation.

For series 2b, the material was homogenised, air-cooled and then reheated before being rolled on the 14 pass schedule. Figure 4.6 shows that this treatment results in a much lower initial resistivity compared with both series 2a and the data from Andersson [64] (in figure 4.6, the trend lines from figure 4.5 are copied). This can be understood by realising that the material was homogenised in rather large blocks (15*15*50 cm). The thermal mass of these blocks is such that the cooling from homogenisation to room temperature takes 5 hours. During this period, precipitation takes place, resulting in a lower initial resistivity. The large difference compared with series 2a, supports the hypothesis that the homogenisation treatment has a

considerable influence on the precipitation behaviour during break-down rolling. This conclusion is in line with the findings of Scott Goodrich [26], who concluded that the homogenisation treatment is of vital importance to the subsequent microstructure. Figure 4.6 also shows that, for series 2b, the resistivity is constant throughout the schedule. This is consistent with the hypothesis that a lower initial value yields a lower driving force for precipitation.

Figure 4.7 shows the resistivity measurements from series 2d (material B) together with the trend lines for series 2a and the industrial data. The homogenisation treatment for 2d was exactly the same as that for 2a. However, the initial resistivity value is lower and very close to that for the industrial data. Also, the chemical composition (see table 2.3) of material B is very similar to that of material A. Only the magnesium content is somewhat different, but according to equation 5.4, this should not influence the resistivity very strongly.

Finally, the nine and fourteen pass schedules are compared with each other in figure 4.8. This comparison is made using series 1 and 2b, since these two series have the same chemical composition and homogenisation treatment. Since figure 4.8 compares two different reduction schedules, Pass number cannot be used to plot the results. Therefore, here the resistivity is plotted as function of cumulative strain. Figure 4.8 shows an excellent agreement between the results from the nine and fourteen pass schedule. This suggests that the actual reduction schedule does not influence the precipitation behaviour. Originally it was concluded that the results from series 1 indicate some concurrent precipitation [76]. However, the results from series 2b enable the measurements to be expanded to higher cumulative strain values. From these it is seen that the resistivity is almost constant and that no concurrent precipitation occurs during this schedule. Again, the low value before the first pass (and thus the low driving force for precipitation) is believed to be the cause.

5.7 *Evolution of the constituent particles*

It is seen from figure 4.19a,b that the particles in the as-homogenised material show a cell-structure which originates from the casting. After 10 passes this structure has changed to one in which the particles are aligned into bands (figure 4.20a,b). Only after 14 passes do the particles appear to be randomly distributed (figure 4.21a). These observations correspond with those made by Daaland [29].

From table 4.7 it could be concluded that the average diameter of the constituent particles is almost invariant throughout the rolling sequence. It is believed that this is an artifact. The micrographs clearly show that the large particles present in the as-cast material are broken up after fourteen passes. The artifact is caused by two things. The first factor is the resolution of the SEM analysis. The image analyser was set to detect all second phase particles with a diameter larger than 1 μm. During the rolling sequence, more and more particles will be broken down into pieces with a diameter below this threshold. When this happens, those particles are ignored in the SEM measurement, which results in a value for $\bar{\eta}$ that is higher than it should be. The measurements are also influenced by the irregular shapes of the as-cast constituent particles. This means that one large particle can appear as two small ones in the SEM picture. When such a particle does shear into two particles, the resulting decrease in average particle diameter will not be recorded by the SEM measurements.

From table 4.7 it can be concluded that the distribution of the second phase particles in the centre of the slab, does not change significantly during the first 10 passes of the rolling schedule. This is caused by the inhomogeneous distribution of strain. Therefore after 10 passes, the material at the centre line (which is shown in the figures 4.20ab) has not been deformed as much as would have been the case if the strain were homogeneously distributed through the thickness.

When material A and material B are compared with each other, it can be said that the distribution parameters for both materials are quite similar. From figure 4.19a.b it could be concluded that the cell structure of the constituents is more clear in material B but this difference seems to have little effect on the particle size distribution.

In the literature, few data are available about the constituent particle size distribution throughout break-down rolling of AA3104. Daaland [29] found for AA3003 at transfer gauge that $L=1.3\ 10^{6}\ m^{-1}$ and $N_0=1.0\ 10^{16}\ m^{-3}$, which correspond quite well with the values found from the present work. Daaland's value for N_0 is slightly higher but this difference can be understood from the difference in chemical composition between AA3003 (Al-1Mn) and AA3104 (Al-1Mn-1Mg).

To sum up, it may be said that the size and size-distribution of the second phase particles as found here do correspond with those from the literature. When modelling the microstructure of the centre line of a slab during a break-down rolling sequence, it is not correct to assume that there is no evolution in the size-distribution of the constituents. Especially after the later passes this distribution changes significantly. Because of the effect of the second phase particles upon the recrystallisation kinetics, this phenomenon must be considered in such a model.

5.8 *Size and morphology of the grains*

Table 4.3 shows the recrystallised grain size for series 2a. It is seen that during the first 6 passes the grain size of the recrystallised grains is reduced from 140 μm to 60 μm. After this the size of the recrystallised grains is approximately constant around 50 μm. Since no abnormal grain growth occurs, the grain size of the recrystallised grains is determined by the number of active recrystallisation nuclei. The fact that the grain size is constant over the last few passes, indicates that the number of successful nuclei is also constant.

Figure 4.17a and 4.18abcd show the microstructures after 0, 5, 10, 12 and 14 passes of series 2a. Even in the completely recrystallised structure the grains are not equi-axed. This is caused by the constituent second phase particles. These particles are formed on the dendrite boundaries during solidification. Although they are broken up during breakdown rolling, they are somewhat aligned into stringers even in the final structure. This retards the growth of the recrystallising crystals in the ND direction (for more details about the constituents see section 5.7). This effect has also been found by Belling et al. [72]. The non recrystallised grains are pan-cake shaped which can be understood from the strain that is applied to the original equi-axed structure.

5.9 *Texture measurements*

The texture measurements of series 1 (table 4.2) show that the volume fraction of the cube component is constant over all nine passes. Since no recrystallisation occurred during this reduction schedule, this could be interpreted as a prove of the meta-stability of the cube component as found in the literature [77]. However, since the volume fraction of the Cube component in the as-cast material is very low, these results provide no definite proof of such a mechanism.

When looking at the S-component, the following can be said. In figure 4.10, the volume fraction S (R_S) measured from series 1, is plotted against the cumulative strain. It is seen that R_S rapidly increases with strains smaller than 0.5. At higher strains ($\varepsilon>1$), R_S seems to level out. Such a profile, can be described by an equation of the form:

$$R_S = A + B\left(1 - \exp(-C \cdot \varepsilon)\right) \tag{5.5}$$

Using a least squares method, equation 5.5 was fitted to the experimental results. It was found that A=0.12, B=0.19 and C=2.7 resulted in the best fit. This fit is shown in figure 4.10

In the NTNU-model, the evolution of the R_S as a function of strain is described as:

$$\begin{aligned} R_S &= 0.04 + 0.17 \cdot \varepsilon \text{ for } \varepsilon < 2 \\ R_S &= 0.38 \text{ for } \varepsilon \geq 2 \end{aligned} \tag{2.36}$$

According to Vatne [36], these equations are based upon the experimental work of Juul Jensen et al. [78] on AA3003. In figure 4.10 the outcome of equation 2.36 is also shown. Comparing the experimental data with equation 2.36, it is seen that the present values are a bit higher than those of Juul-Jensen. This difference could easily be caused by the difference in chemical composition between AA3104 and AA3003.

Comparing equation 5.5 to equation 2.36, it can be concluded that both equations generate a saturation level at high strains. This seems physically sound. After all, although the S-texture is a deformation texture, it will be in competition with the other deformation texture components after high strains. The saturation level of both equations (0.31 vs. 0.38) is in reasonable agreement. However, for $\varepsilon<1$, equation 5.5 predicts considerably higher values of R_S. This prediction is supported by both the present experimental values and by those from Juul Jensen. Another disadvantage of equation 2.36 is the discontinuity at $\varepsilon=2$. It is unlikely that there is change of mechanism at $\varepsilon=2$ which would justify a description like equation 2.36. However, both equation 5.5 and 2.36 are purely empirical.

Figure 4.11 shows the evolution of the S component as a function of pass number from series 2a,b,c,d. It is seen that the as-homogenised structure for all series has an R_S of 0.1. This value is to be expected from a randomly oriented material and in agreement with equation 5.5 which predicts $R_S=0.12$ for $\varepsilon=0$. Upon increasing pass number up to pass 10, the S-component increases. It was found that no recrystallisation occurs during the first 5 passes. Therefore it could be expected that equation 5.5 predicts R_S correctly for the first passes of the 14-pass schedule. The cumulative strain of the first 5 passes is 0.63. Equation 5.5 thus predicts R_S to be 0.28. Equation 2.36 predicts R_S to be 0.15. The experimental value (0.11) is lower than both predictions. It is unclear why the S-component develops so much more slowly for these experiments compared to the 9-pass schedule of series 1. However, figure 4.11 does show that R_S suddenly drops after pass 10-11. This coincides with the start of recrystallisation, as found from the optical microscopy. After passes 12 to 14, R_S even drops below the initial value of the as-cast structure. This supports the hypothesis that the S-component is consumed preferentially during recrystallisation.

When series 2a,b,c,d are compared with each other, it is found that the results from all three series are quite similar. Only after 10 passes the material B from series 2d seems to result is a lower R_S. However, more

experimental work is necessary before any definite conclusions about the differences in the evolution of the S-components can be drawn.

Figure 4.12 shows the evolution of the Cube component as a function of pass number for series 2a,b.c.d. It is seen that for all series the cube stays low and constant up to pass 10. After this the cube is seen to increase to about 5%. Comparing this profile with the fraction recrystallised, it can be concluded that these two profiles are very similar in shape. This suggests that it might be possible to measure the fraction recrystallised from the volume fraction cube. It also confirms the well known fact that the volume fraction cube increases upon recrystallisation.

The small difference between the results of the different series suggests again that neither the exact chemical composition nor the difference in homogenisation treatment, influence the texture evolution strongly.

When the absolute levels of volume fraction cube are compared with those from the literature, the following can be said. The values found by Vatne [36] and Daaland [29] are typically in the order of 15 to 20 percent. The fact that the present values are much lower is caused by the way the volume fractions are calculated. In the present work, these fractions are calculated directly from the ODF's by the software as developed by Van Houtte [65]. Vatne and Daaland used a method that is based on the work of Lücke et al. [79]. So far it is not clear how these two approaches are related.

5.10 *Modelling*

5.10.1 Modelling lateral spread

Below, a short literature overview is given about the modelling of lateral spread. The models that were found in the literature are then applied to the present results together with a new model which is also presented.

Billington et al. [80] state that the amount of lateral spread is a function of:

- alloy characteristics
- roll gap geometry
- rolling speed

Sheppard et al. [81] added the homologous temperature and the interfacial friction between the roll surface and the slab to this list. Over the last decades several equations have been derived to describe this phenomenon using either an analytical or an empirical approach. So far the analytical approaches are not very accurate in describing the spread (see for instance Wilson et al. [82]) and will not be discussed here any further. Some of the empirical equations (based on results from either ferrous or non-ferrous materials), are discussed below. A selection of these equations is then applied to the present experimental work to investigate their validity.

For steel, Helmi and Alexander [83] derived the equation:

$$\frac{\ln\frac{b_f}{b_0}}{\ln\frac{h_f}{h_0}} = 0.95\cdot\left(\frac{b_0}{h_0}\right)^{-1.1}\exp\left[-0.707\left(\frac{b_0}{h_0}\right)^{-0.971}\frac{b_0}{\sqrt{R_R(h_0-h_f)}}\right] \quad (5.6)$$

Sheppard et al. [81] found that for aluminium, the spread can be described by:

$$\ln\left(\frac{b_f}{b_0}\right) = \left(0.11+0.032\cdot T_H-0.01\frac{R_R}{h_0}\right)\cdot\left(\frac{b_0}{\sqrt{R_R\cdot(h_0-h_f)}}\right)^{-3.5}\left(\frac{b_0}{h_0}\right)^{K} \quad (5.7)$$

where $K = 1.375\cdot T_H + 0.233\left(\frac{R_R}{h_0}\right) - 0.1$

and T_H is the homologous temperature. They also found that the amount of spread decreases with decreasing friction coefficient.

Raghunathan et al. [84] derived an alternative equation that was specifically applied to two Al-Mg alloys (AA5056 and AA5083):

$$\ln\left(\frac{b_f}{b_0}\right) = 2.45 \cdot \left(\frac{b_0}{h_0}\right)^{0.71} \cdot \left(\ln\left(\frac{Z}{A_2}\right)\right)^{0.002} \cdot \left(\frac{R_R}{h_0}\right)^{0.04} \cdot \exp\left\{\left(2.72 - 0.125 \cdot \ln\left(\frac{Z}{A_2}\right)\right) \cdot \left(\frac{R_R}{h_0}\right)^{0.55} \cdot \left(\frac{h_0}{\sqrt{R_R \cdot (h_0 - h_f)}}\right)\right\} \quad (5.8)$$

Where A2 is a material constant from the sigma(Z) equation of the form of equation 2.12. From the PSC-tests on the 10-pass material, this value was derived as $A_2 = 10\ 10^6\ s^{-1}$ for Al-1Mn-1Mg (Taken from table 4.10, for more details, see section 5.4, Sigma(Z) behaviour). Furthermore, equation 5.8 uses the Zener Hollomon parameter, Z. Even for a single pass rolling operation, such a value is hard to determine accurately due to steep gradients through the thickness of the slab during the deformation, both in terms of temperature as well as strain rate. To be able to apply equation 5.8 to the present rolling schedule an average value for Z for each pass was calculated, ignoring these gradients.

The present results were also analysed using a new model. The equation for this model was derived by analogy with the spread coefficient as defined by Silk et al. [68] for plane strain compression specimens.

$$\frac{b_f}{b_0} = -C^{spread} \cdot \left(\frac{h_f}{h_0}\right) + \left(1 + C^{spread}\right) \quad (5.9)$$

Where C^{spread} is a modelling constant which is normally referred to as the spread coefficient.

5.10.2 Validation

To validate the models, the predictions of the four models are compared with each other. The results of this exercise are shown in table 5.2 and graphically illustrated in figure 5.4. It must be noted that equations 5.6, 5.7 and 5.8 have been derived for

single pass deformations. Therefore they can only be applied to the present (multi-pass) results if b_0 and b_f are redefined for each pass. For example for the interpretation of a 14 pass rolling experiment, each equation has to be applied 14 times consecutively to predict the final breadth of the sample. The reason for this is two-fold. Firstly, there is the geometry of the roll gap. This geometry changes for each pass and therefore the geometry per pass must be used. The second reason is that during the deformation, a friction stress builds up towards the side of the slab. This stress is relieved at the end of the deformation. The two factors combined, result in a different spread behaviour for a single-pass compared with a multi-pass rolling schedule of equal total reduction.

A consequence of the consecutive application of the spread equations is that any systematic error in the prediction of the models is amplified on the next pass. It is seen (table 5.2, figure 5.4) that the solution for Raghunathan's model (equation 5.8) becomes unstable after pass seven. The reason for this lies in the strong influence of the ratio between b_0 and h_0 upon the predicted width of the slab. Sheppard's model (equation 5.7) predicts very unrealistic values after the twelfth pass. The model suggests that the width of the slab decreases for the last passes. This effect is caused by the first term of equation 5.7 that becomes negative for small values of h_0. A second problem of this model is again the use of b_0/h_0. Here the problem is even bigger compared with Raghunathan's model since the factor K can be as high as 5.9 for the last pass of the 14-pass schedule. From figure 5.4, it is concluded that neither equation 5.7 nor equation 5.8 can be applied to the present multi-pass schedule. Therefore, these two models will not be discussed here any further.

Helmi and Alexander's model seems to generate much better predictions compared with Raghunathan and Sheppard's models. From equation 5.6 it is seen that the dependency of the model-predictions upon b_0/h_0 is much weaker. However, it must be noted that all the constants for these equations are determined from laboratory experiments. For such tests b_0/h_0 is usually in the range from 1 to 6. However, industrially this ratio lies between 20 and 750. Hence, it is highly debatable whether the laboratory values can be extrapolated towards the industrial situation. On the

other hand, from figure 5.4, it is seen that equation 5.6 could describe the present experimental results.

The predictions of equation 5.9 are fitted to the measured values and are therefore bound to predict values that are in reasonable agreement.

To quantify the performance of a model, the Residual Standard Deviation (s) can be used. For models that do not use fit-parameters, s is defined as:

$$s = \sqrt{\frac{\Sigma\left(d^n_{measured} - d^n_{predicted}\right)^2}{(n-1)}} \tag{5.10}$$

where n is the number of data points.

When a model does use fit-parameters, s equals:

$$s = \sqrt{\frac{\Sigma\left(d^n_{measured} - d^n_{predicted}\right)^2}{(n-p-1)}} \tag{5.11}$$

where p is the number of linear fit coefficients.

The two remaining models (Helmi and Alexander and equation 5.6) are now validated using the residual standard deviation. Equation 5.6 is not fitted to the data and therefore equation 5.10 applies. Equation 5.9 has one linear fit parameter and thus equation 5.11 must be applied, where p=1.

Table 5.3 shows the residual standard deviation for the two models applied to the different series of experimental data. Both the absolute and the relative value are shown, where the relative value is calculated as:

$$s_{rel} = \frac{s}{\overline{b_f}} \tag{5.12}$$

where $\overline{b_f}$ equals the average breadth after rolling for all data-points used in this analysis. Table 5.3 is discussed in detail below.

Firstly, all the experiments that were acquired from the Hille mill (i.e. series 1 and 2a-d) are used to compare the performance of equation 5.9 with Helmi and Alexander's equation. In figure 5.5 the goodness of fit of equation 5.9 is illustrated when this equation is applied to the results of series 1 and 2a-c. Here C^{spread} is 0.19.

Figure 5.6 shows the same results when Helmi and Alexander's equation (equation 5.6) is applied. Both from these figures and the s-values from table 5.3, it can be concluded that equation 5.9 describes the present results more accurately than equation 5.6.

Nevertheless, in figure 5.5 the results from both the non-lubricated and the lubricated tests are used together to find the best value for C^{spread}. Sheppard found that the friction conditions influence the spread [81]. If this is the case, it can be expected that equation 5.9 will perform better when the C^{spread} is made dependant upon the (two) friction conditions. Figure 5.7 shows the result of this exercise where $C^{spread}_{lubricated} = 0.20$ and $C^{spread}_{non-lubricated} = 0.14$. It is now seen that this reduces s indeed, which supports the assumption that the friction conditions do have an influence on the amount of lateral spread. Furthermore, the fact that $C^{spread}_{non-lubricated}$ is smaller than $C^{spread}_{lubricated}$, supports Sheppard's observation that the amount of spread increases when the friction decreases. In Helmi and Alexander's equation there is no factor that models the influence of the friction conditions. However, when the two sets of results are shown as separate series as is done in figure 5.8, it is seen that this equation performs much better for the non-lubricated tests compared with the lubricated tests.

Another factor that is believed to influence the spread behaviour is the roll-radius. The influence of this factor was investigated by rolling on two different rolling mills with different roll radii. For this part of the validation, only the results from the non-lubricated tests are used.

Series 1 and 2a-d were carried out on a Hille mill with a roll radius of 68.2 mm. Series 3 was done on a Robertson mill with a roll radius of 123.8 mm. To eliminate the influence of friction, only the non-lubricated tests will be used here (i.e. the results of series 1 and 3). Figure 5.9 shows the model predictions of equation 5.9 when $C^{spread}_{non-lubricated}$ is applied to all tests. It is seen that the predictions for series 3 are very poor. When the spread coefficient is made to be dependant on the roll-radius, the predictions become much better (figure 5.10). This confirms the influence of the roll radius. Helmi and Alexander's equation models this effect. This is illustrated in figure 5.11. It is seen that the model performs quite reasonably for the results from

both mills. This suggests that the dependency of spread upon roll radius is modelled correctly by equation 5.6.

5.10.3 Lateral spread and von Mises criterion

So far, it has been assumed that lateral spread can be described by the change in the length of the contact line in the width direction $b^{contact}$. It is quite clear that $b^{contact}$, affects the rolling loads and should therefore be taken into account in roll force models. However, there is a second effect caused by lateral flow that should be considered in such models. This is the way in which the equivalent strains and stresses occurring in a roll pass. The calculation of equivalent strains and stresses is important because the constitutive equation used in roll force model, describes the relationship between equivalent tensile strain and equivalent tensile stress. This can only be applied to rolling if the occurring strains are converted into equivalent strains.

When plane strain conditions apply (i.e. assuming no lateral spread), the equivalent strain is calculated from the initial and final thickness of the slab using equation 2.2.

$$\varepsilon = \frac{2}{\sqrt{3}} \cdot \ln\left(\frac{h_f}{h_0}\right) \tag{2.2}$$

When the lateral spread is taken into account, the equivalent strain is calculated from:

$$\varepsilon = \frac{2}{\sqrt{3}} \cdot \sqrt{\left(\varepsilon_2^{\,2} + \varepsilon_2\varepsilon_3 + \varepsilon_3^{\,2}\right)} \tag{5.13}$$

where:

$$\varepsilon_2 = \ln\left(\frac{b_f^{vonMises}}{b_0}\right) \tag{5.14}$$

and

$$\varepsilon_3 = \ln\left(\frac{h_f}{h_0}\right) \tag{5.15}$$

It must be noted that equation 5.14 uses $b_f^{vonMises}$ rather than $b_f^{contact}$. The parameter $b_f^{vonMises}$ is defined as the average (averaged over the thickness of the specimen) width of the specimen. However, the calculation of $b_f^{vonMises}$ is not completely trivial. Due to due to the inhomogeneous strain distribution through thickness the initial square cross section of the slab will not stay square during break-down rolling. Typically, a double barreled shape occurs. A schematic representation of a typical cross section of a specimen is shown in figure 4.3 This shape is typical for all specimens rolled as part of series 1 and 2a-c. The double barreled shape persists throughout the complete break-down schedule. Furthermore, the specimens showed no signs of side folding as described by Sheppard et al. [81]. The most accurate way to calculate $b_f^{vonMises}$ would be to photograph cross sections of all specimen and then calculate $b_f^{vonMises}$ using digital image analysis techniques. A less laborious way to obtain an estimate of $b_f^{vonMises}$ is presented below. In the present work $b_f^{vonMises}$ of all double barreled samples has been calculated from two widths (b^{max} and b^{half}). These values are graphically illustrated in figure 4.3 They are combined into $b_f^{vonMises}$, using equation 5.16.

$$b_f^{vonMises} = \frac{2 \cdot b^{max} + b^{half}}{3} \tag{5.16}$$

The specimens of series 3 exhibited a convex profile. For these samples only $b^{contact}$ has been measured.

From the measurements it was found that the actual value of $b_f^{vonMises}$ is the same as that of $b_f^{contact}$. This can be understood as follows. During the first passes b^{max} increases much more than $b^{contact}$. However, this effect is compensated by the fact that b^{half} does not increase at all during these passes due to inhomogeneous strain distribution. During the later passes, b^{half} does increase but in its turn this is compensated by a slower increase in b^{max}. Therefore, from a modelling point of view, it is acceptable to use the same model for both $b^{vonMises}$ and $b^{contact}$.

5.10.4 Concluding remarks

From the discussion above, it can be concluded that the models as presented by Sheppard (equation 5.7) and Raghunathan (equation 5.8) cannot describe to the present experimental results. The (older) model of Helmi and Alexander (equation 5.6) results in a much better correlation. From the experiments on a second rolling mill, it can be concluded that the way this equation models the influence of the roll radius appears to be correct. However, more research is necessary since, here only two roll radii have been used.

In this work a new, completely empirical, equation has been presented. This model describes the spread behaviour, using one single constant, the spread coefficient. This coefficient has been shown to depend on the friction conditions and on the roll radius. However, once the spread coefficient is known, equation 5.9 describes the experimental results better than Helmi and Alexander's model.

From a scientific point of view, equations such as equation 5.9 are of no great significance, since they do not aid in gathering any more insight into the underlying mechanisms. However, from an industrial point of view, equation 5.9 could be useful. In a production environment, the roll radius is invariable and therefore it is not a problem that equation 5.9 does not model this effect. Concerning the friction conditions, a similar argument applies. Lubrication conditions do differ between different mills but are very rarely changed strongly for a single mill. Nevertheless, it is still necessary to determine C^{spread} for each mill individually. However, since equation 5.9 can be easily applied to either single- or multi-pass rolling schedules, this should be feasible. This leaves the influence of temperature, rolling speed and alloy characteristics. These three features can be taken together since all of them influence the spread behaviour through their influence on the flow stress of the material. Most factories process a range of products that will exhibit a range of flow stresses during rolling. However, the fact that equation of Helmi and Alexander (which was originally derived for steel!) describes the present results on aluminium reasonably well, suggests that the influence of the flow stress on the spread behaviour is not very strong and can be ignored.

5.11 SLIMMER

The main aim for which SLIMMER was used in the present project is to predict the temperature history of an industrial slab during break-down rolling. Since very few industrial accurate measurements of this parameter are available, it is not possible to validate the SLIMMER predictions on this aspect. However, from figure 4.2 it can be concluded that the predicted history seems reasonable. The slab only cools down on the final deformations where the surface to volume ratio becomes such that considerable heat loss to the surroundings is possible during the inter-pass periods.

Furthermore, SLIMMER provides a roll force calculation. The measured roll forces on SMART can be used to validate these roll force predictions. This is done below. Industrially it is very important to have an accurate roll force model. The first application of such a model lies in the prediction of pre-set values for the mill spring. However, a second possibility might be to calculate the temperature of the slab by comparing the measured loads with those predicted by the model. This would be advantageous since even state of the art pyrometers are still not very accurate and need very extensive calibrating. The only way to acquire an accurate reading of the surface temperature of the slab is via contact thermometers. These are not very practical in a production environment. Therefore, it might be better to use the load readings from a mill to calculate the temperature. This cannot generate an absolute temperature but (assuming that friction conditions do not change too much with temperature) it should be possible to calculate the temperature differences between some reference pass and the pass which is considered.

From the discussion above it is clear that an accurate roll force model is very beneficial. Especially within the aluminium industry, such models are still in a very empirical stage.

The most widely used expression to calculate the roll force has been derived by Sims [55]. Assuming plane strain conditions, the specific roll force F'_{spec} follows from equation (5.17):

$$F^{i}_{spec} = \frac{F^{i}_{roll}}{b^{contact}} = \frac{2}{\sqrt{3}} \cdot \bar{\sigma} \cdot \sqrt{R_R (h_0 h_f)} \cdot Q \qquad (5.17)$$

In equation 5.17, the roll radius R_R signifies the roll radius as it is during the deformation. The relationship between this value and the radius of rolls when not in contact with the slab, depends on the rolling load. However, this aspect is beyond the scope of the present discussion. Here, the rolls are considered to be infinitely stiff and therefore the deformed roll radius is equal to the non deformed roll radius.

Q in equation 5.17, is a complex function of the roll radius, the final thickness, the reduction and the friction conditions. $b^{contact}$ is the width of the slab as discussed in chapter 4.1. In equation 5.17, $\bar{\sigma}$ is the mean true flow stress during the deformation. This value can be calculated from equation 5.18 [85].

$$\bar{\sigma} = \frac{1}{\theta_0} \int_0^{\theta_0} \sigma(\varepsilon, \dot{\varepsilon}, T) \cdot d\theta \qquad (5.18)$$

Where θ_0 and θ are the angles as shown in figure 2.5.

The relationship that describes the flow stress as a function of strain, strain rate and temperature is normally referred to as a constitutive equation.

The algorithm that is used by SLIMMER to calculate the roll forces is based upon equation 5.17 and 5.18. Table 4.1 shows the roll forces as they were predicted by SLIMMER (see chapter 4.1 for more detailed information on how these values were calculated). These data are graphically represented in figure 5.12. From this figure it can be concluded that the roll force predictions do not agree with the measured values. Especially for the first passes the agreement is very poor.

A first possible explanation could be the way in which SLIMMER models the lateral spread. SLIMMER allows the user to enter a 'spread percentage'. However, the programme only uses this value to calculate the initial width for the next pass. Since here only specific roll forces are validated, the change in $b^{contact}$ is not relevant. However, how closely the deformation fulfils the plane strain conditions could be important since this affects the way in which the reduction is translated into

equivalent tensile strains that can be handled by the constitutive equation. SLIMMER assumes equation 2.2 to be valid. It would be more accurate to replace this equation with equation 5.13. The difference in the outcome of these two equations becomes larger with larger strains. During the 14-pass rolling schedule (series 2), the maximum reduction occurs during pass 12. During this pass, the thickness of the slab is decreased from 7.6 to 4.7 mm (table 3.4). According to equation 2.2, this results in an equivalent tensile strain of 0.55. When equation 5.13 is applied combined with equation 5.9, the equivalent tensile strain becomes: 0.67. Such a relative small change in the strains that are fed to the constitutive equation will make very little differences in the average flow stress calculated from equation 5.18 because of the absence of strain hardening in these alloys. This means that for the relative small reductions the effect of lateral spread on the calculation of the equivalent tensile strain can be ignored for this material. It is thus concluded that applying equation 2.2 in stead of 5.13 cannot explain the poor performance of the roll force calculations.

A possible explanation could be found by looking at the Δ-factors of the first passes of the present schedule. Studies by Beese and others [85] have shown that measured rolling forces for passes with a Δ-factor of 2 and higher generate much higher roll forces than would be predicted by equation 5.17. Accordingly, Beese suggested a multiplying term n. The values of this term are shown in figure 5.13. These values are based on the shear-line field theory for the variation of indenting pressure with increasing Δ (=thickness to length of the arc of contact'-ratio). From table 3.4 it is seen that the maximal Δ-factor for the 14-pass rolling schedules is 0.91. This means that the modifying term as it was proposed by Beese cannot correct the present roll force predictions.

A possible explanation could be the way in which SLIMMER deals with friction. This phenomenon is all 'hidden' inside the Q factor in equation 5.17 and it is very well possible that the Q used does not apply to the present experimental conditions. If we assume the error caused by this to be constant for all passes, the performance of SLIMMER should improve when the roll forces are scaled. This is shown in figure 5.14. In this figure both the measured and the predicted roll forces are scaled,

where the first pass is set to 1. Comparing this figure with figure 5.12, it can be concluded that the relative roll forces are closer to the measured ones. This suggests that a better handling of the friction phenomenon would improve the roll force predictions.

However, another source of errors could be the way in which the average starting temperature of the slab is obtained. This value (shown in table 3.4) is taken from the thermocouple readings. The thermocouple was inserted in the middle of the specimen and therefore the temperature readings represent the centre line temperature. It is seen from figure 4.2 that, especially during the last passes, the temperature drops due to the chilling effect of the cold rolls. This chilling effect will cause very steep temperature gradients. However, since no information about these gradients was available, they were ignored in the SLIMMER simulation. For each pass, a separate run of SLIMMER was programmed where the initial (homogeneous) temperature was taken from the thermocouple reading. This results in an overestimation of the average temperature since the centre line can be expected to be the hottest. The effect of temperature on the average flow stress (and thus on the roll force prediction) is quite strong. Therefore, it can be expected that the roll force predictions would improve if a more accurate estimate of the temperature gradients was used as input for SLIMMER.

5.12 NTNU-model

Below the NTNU-model, as it is described in chapter 2.4.3.2 is evaluated. In the first part of this section the model is validated against the present experimental results obtained from SMART. Especially the influence of the size distribution on the model predictions is discussed. This is then followed by a discussion about the other important assumptions that lie behind this model. This discussion then results in a series of suggestions that could be included in future versions of this model.

The NTNU-model was validated against the results from series 2a. Both the microstructural predictions (fraction recrystallised, recrystallised grain size) and the

texture predictions have been compared with the experimental results. Below, these model predictions are discussed.

Table 5.4 shows the microstructural features from series 2a (taken from table 4.3) and the predictions of the first run of the model. These data are graphically illustrated in figure 4.24a,b,c. From this it is seen that the model predicts the recrystallisation to start after the sixth pass. This is confirmed by the experimental results. Also the predicted fraction recrystallised and the grain size of the recrystallised grains are in quite good agreement with the experimental observations.

The predicted Cube fraction of the first run of the NTNU model are shown in figure 4.24c together with the experimental observations. It is seen that the model overestimates the Cube-fraction for pass 7, 8 and 14 and underestimates it for pass 10, 11 and 12. Only after the 6^{th}, the 9^{th} and the 13^{th} pass, the predictions agree with the experimental values.

To improve the performance of a model, one has to reconsider its assumptions. One of the assumptions that was proven inaccurate by the present experimental results, is the assumption that the size and number of constituent particles is constant throughout the rolling sequence (assumption vii in paragraph 2.4.3.2). To study the influence of this upon the model predictions, the model was run once more. This time the parameters that describe the second phase particle distribution; H and L (from equation 2.41) were taken from the SEM measurements of the as homogenised material (table 4.7). All the other modelling constants were kept constant compared with the first run. Below, the first run is referred to as '14' since it uses H an L from the transfer gauge, 14 pass material and the second run is referred to 'AH' (As Homogenised). When the two runs of the model are compared with each other the following can be seen. Figure 4.24a,b shows that AH results in a slightly faster recrystallisation and a smaller recrystallised grain size. Furthermore, for the initial passes, AH yields a significantly higher predicted cube fraction.

Comparison of both runs with the experimental results gives rise to the following conclusions. Up to pass nine, the model predicts the fraction recrystallised quite

well. The same applies to passes 12, 13 and 14. Figure 4.24a and 4.24b show that when the fraction recyrstallised is predicted accurately, the predicted recrystallised grain size is also quite close to the experimental results.

The texture predictions of both runs of the model are also quite reasonable. However, due to the small variation in the experimental results, this dataset is not particularly suitable for validating this aspect of the model. Also, the experimental conditions during the experiments on SMART are quite difficult to model, compared with for instance plane strain compression tests which offer a better temperature control. Especially the temperature drop during the deformation on SMART is difficult to model.

Assuming the as-homogenised particle distribution throughout the rolling schedule, it is expected that the model predictions are more accurate towards the first rolling passes compared with '14'. From figure 4.24a and 4.24b it is seen that this is the case for the prediction of the fraction recrystallised and grain size. However this does not apply to the prediction of the Cube fraction. For all passes but the ninth pass, the 14-run performs better than the AH-run. This indicates that the assumptions concerning the development of the cube fraction that lie behind the model are not yet fully understood.

Besides validating the model against experimental results, it is also important to review the assumptions of the model critically. The assumptions of the NTNU-model are repeated below:

(i) The recrystallisation texture is a result of oriented nucleation.

(ii) The final grain structure and texture are a result of the competition between growing grains that originate from a limited number of different types of site categories, where each site category has a density N_i.

(iii) Near site saturation nucleation kinetics apply.

(iv) The nucleation sites are randomly distributed in space.

(v) Johnson-Mehl-Avrami-Kolmogorov kinetics apply

(vi) During all deformation passes, steady state stress is reached.

(vii) The number and size distribution of the second phase particles are constant throughout the entire schedule.

The first assumption has been checked extensively by for instance Vatne [36]. Nevertheless it is still been subject of many discussions. It is also the main principle of the NTNU-model. However, in this project this aspect has not been studied any further and therefore this assumption must be accepted.

Assumption (ii) is not according to reality. From the texture measurements it is clear that there are many different texture components that the model assumes to be part of 'random'. However, from an industrial point of view, the cube texture is the most interesting component due to its strong influence on the earing behaviour. It is therefore quite justifiable to build a model that focuses on this component. Besides that, the structure of the model is such that a next component can be added easily when the amount of nuclei can be described.

Assumption (iii) and (v) are supported by the present results. However, the model assumes a constant growth rate throughout the schedule (G in equation 2.48). This assumption was checked in the present work by determining the recrystallisation kinetics after 10 and 13 passes. It was found that $t_{0.5}$ after 10 passes differs greatly from $t_{0.5}$ after 13 passes. The most likely explanation for this is the change in driving force for recrystallisation due to static recovery in between the passes. The present model assumes the driving force to accumulate when no recrystallisation occurs during the inter-pass times. The model could be improved by adding a static recovery term that describes the decrease in driving force for recrystallisation even when the material does not recrystallise during that particular inter pass time.

Whether or not steady state is reached in the first passes, is debatable (assumption (vi)). From the slip line field analysis (see figure 2.6), it is seen that the local strain on the first passes is almost zero at the centre line (see figure 2.6). However, at that

stage, no recrystallisation occurs. Therefore, the strain of the first 6 passes can be regarded as if it were from one big pass that does satisfy assumption (vi).

Another important aspect during break-down rolling is the Zener drag from dispersoids and small precipitates. Numerous investigations have shown that a 3104 alloy contains small dispersoids after homogenisation and small particles will also precipitate during the rolling sequence. This aspect is covered in the model by a constant Zener drag, which of course is a simplification. The Zener drag should increase throughout the rolling schedule due to precipitation during rolling.

There are several tuning parameters in the model. Ideally, a complete model should not contain such parameters, but our current knowledge is not sufficient to achieve this. Some of the model constants are purely empirically determined, like A and B (subgrain size, equation 2.20), H and L (particle size distribution, equation 2.41).and the parameters that describe the evolution of the S-component as a function of the strain (equation 2.36) In future, models for casting, homogenisation and substructure evolution may make such empirical relationships unnecessary. However, when such equations are not available, the present model can be improved by 'sophisticating' the present empirical equations.

For instance equation 2.41 cannot describe the particle distribution accurately since it assumes the number of particles to increase with decreasing particle radius. Although the present model does not use the particles that have a radius which is smaller than the critical value η^* (see equation 2.39) it is still advisable to describe the whole second phase particle distribution as accurately as possible. This makes it possible to include the influence of the smaller particles (for instance on the Zener drag) in future versions of the model. A more physically based approach would be to assume the second phase constituents to be log normally distributed. For a log normal distribution the probability density function is given as [86]:

$$f(x) = \frac{1}{x \cdot \Omega \cdot \sqrt{2\pi}} \exp\left\{\frac{-\left[\log\left(\frac{x}{m}\right)\right]^2}{2\Omega^2}\right\} \tag{5.19}$$

With: x = Probability density

m = median

Ω = shape parameter

From the median and the shape diameter, the mean (μ) and the standard deviation (σ) can be calculated, using equation 5.20.

$$\mu = m\exp\left(\frac{1}{2}\sigma^2\right) \tag{5.20}$$

$$\sigma = m\sqrt{\exp\left(\Omega^2\right)^2 - \exp\left(\Omega^2\right)} \tag{5.21}$$

In the NTNU-model, equation 2.39 is used to calculate the number of PSN-nuclei.

$$N_{PSN} = C_{PSN}\int_{\eta^*}^{\infty} f(\eta)d\eta \tag{2.39}$$

Where $f(\eta) = H\exp(-L\eta)$.

To implement the log normal distribution equation 5.19 must be rewritten from a probability density function into one that describes the actual number of particles. To do this, the total number of particles (η^{tot}) has to be calculated from the volume fraction (v_f) and their average diameter (μ).

$$\eta^{tot} = \frac{6 \cdot v_f}{\pi \cdot \mu^3} \tag{5.22}$$

Multiplying equation 5.19 with equation 5.22 yields the distribution function $f(\eta)$.

$$f(\eta) = \left[\frac{1}{x \cdot \Omega \cdot \sqrt{2\pi}} \exp\left\{ \frac{-\left[\log\left(\frac{x}{m}\right)\right]^2}{2\Omega^2} \right\} \right] \cdot \left[\frac{6 \cdot v_f}{\pi \cdot \mu^3} \right] \qquad (5.23)$$

When equation 5.23 is used, equation 2.39 cannot be solved analytically. Possibly, this could be solved by including the results of equation 5.23 in a look up table in the source code of the model. Naturally, the parameters in equation 5.23 should be made dependent on the amount of strain applied throughout the rolling schedule.

Furthermore, the present experimental results indicate that equation 2.36 can also be improved. The suggested equation 5.6 seems to be suitable to describe the S-component quite accurately. Apart from the equation, there is another problem with the usage of R_s. The NTNU model assumes that the volume fraction of S of a specimen equals the volume fraction of the cube grains that is surrounded by an S-grain (R_S in equation 2.36). This assumption implies that both the cube and the S-grains are (in respect to each other) randomly distributed in space. This may be the case when looking at single pass experiments, it cannot be true for a multi-pass deformation when there is recrystallisation during inter stand times. This can be understood as follows. During recrystallisation the S-grains that are adjacent to Cube-grains, are consumed preferentially compared with non adjacent S-grains. Therefore, there will be fewer adjacent S-grains after recrystallisation than to be expected from the S-fraction. During the next pass when new randomly distributed S-grains are generated, the old, non-adjacent S-grains will still exist. Therefore the overall S-fraction will be bigger than the fraction of cube-grains surrounded by the S-component. A future version of the model should therefore differentiate between the total volume fraction of the S-texture and the fraction of 'adjacent to Cube'-S texture.

Finally, the model relies on a set of modelling constants. For instance C_C, C_{PSN} and C_{GB} are pure tuning constants that have to be introduced because the quantitative nature of the nucleation sites for recrystallisation are not fully understood. Ideally, these should be of the order 1. In the present case they are typically 0.1, which is

lower than expected. As already pointed out, this discrepancy can to a large extent be attributed to lack of physical understanding. PSN is an illustrative example of the difficulty in gaining such understanding. The mechanism has been well established and intensively studied for 20 years, while our present knowledge of the mechanism is still only on a semi-quantitative level.

In summary, the model can be improved by:

(i) including a realistic size distribution function of the second phase particles that considers the change in distribution during the rolling sequence
(ii) an extra factor that deals with static recovery which reduces the driving force for recrystallisation
(iii) an improved treatment of deformation texture evolution and distribution

However, despite the potential for improvements, it should not be neglected that the model in its present form already provides reasonable predictions. The basic assumptions, physical understanding and applied model constants appear to be founded on a sound basis.

6. Conclusions and Further Work

6.1 Conclusions

- The conclusions from the present work are given below. To enhance readability, all conclusions are summed up as bullet points. Further comments about some of these points are given in chapter 6.2; 'Further work'.
- It was shown that the chemical compositions for AA3104 reported in the literature are similar to those reported for AA3004. Therefore, the results measured from these two alloys can be compared with each other directly.
- A new experimental method was developed to simulate the break-down rolling of aluminium. The Sheffield Mill for Aluminium Roughing at Temperature offers:
  - high total reduction and number of passes
  - realistic deformation paths and strain distribution
  - temperature control
  - possibility to quench samples at any stage throughout the rolling sequence
- For the alloy studied here, the constitutive equation derived from transfer gauge material can also be applied to the material further upstream.
- The fraction recrystallised is strongly affected by the strain distribution through the thickness of the plate.
- Within the range studied, the recrystallisation *kinetics* is not influenced by the rolling temperature, exact chemical composition (that is supplier of the material) or the rolling temperature.
- The concept of retained strain, which ignores any static recovery during the inter pass times, is not supported by the present experimental results.
- The extent to which precipitation occurs during the break-down rolling of AA3104, is a strong function of the homogenisation treatment. Air-cooling

to room temperature before a pre-heat reduces the amount of precipitation substantially.

- The shape and size of the constituent particles changes considerably during the rolling sequence. However, due to the strain distribution through the thickness of the slab, the constituent particles at the centre line only start shearing off after 10 of the 14 passes in the case studied.
- During multi-pass laboratory rolling, considerable lateral spread occurs. To be able to convert the measured rolling loads into realistic predictions for an industrial situation, it is necessary to take this phenomenon into account.
- A new model is proposed to describe the amount of lateral spread during multi-pass rolling. This model describes the present experimental results more accurately then any of the models found in the literature.
- The roll force predictions from SLIMMER show reasonable agreement with the present rolling experiments as long as its initial predictions are corrected for the constitutive equation that applies to the material being rolled.
- The NTNU-model as developed by Vatne et al. [36], can be applied to the break-down rolling of AA3104. The predicted fraction recrystallised, recrystallised grain size and textures show good agreement with the experimental results.
- From the present experimental data, it can be concluded that a more realistic description of the evolution of the S-component will improve the performance of the NTNU-model. An equation of the form of 5.6 is suggested.

6.2 *Further work*

The recommendations for further work can be split into two groups. Firstly, the experimental technique that has been developed is discussed. This is followed by some recommendations on how the experimental results can be used.

6.2.1 Making SMART smarter

Since this work provided a new experimental technique, a very wide range of possible applications of SMART could be mentioned here as further work. However, below only some specific recommendations are given to improve SMART itself.

The main disadvantage of SMART is the high number of operators that are necessary carry out an experiment. This can be overcome by improving the level of automation of the rolling mill. Especially the reversing of the mill and the setting of the new gauge can be automated relatively easily. Together with an automated logging system, this would reduce the number of operators from 6 to 3, while further improving the reproducibility of the experiments.

A further improvement of SMART can be achieved by using better temperature controllers in the tube furnaces. From figure 4.2, it is seen that the temperature increases very rapidly when the specimen gets below 5 mm. gauge. This results in overheating of the sample. If the tube furnaces were equipped with programmable controllers, it would be possible to reduce the furnace temperature during the rolling sequence.

Finally, the problem of the asymmetry in the strain distribution through the thickness of the slab must be solved. This may be achieved by replacing the work rolls on the laboratory mill.

6.2.2 Modelling recommendations

In the present work, several models were used. The main one is the NTNU-model. For this model the following modifications are suggested.

A modelling approach where the driving force for recrystallisation decreases even in the absence of inter stand recrystallisation can further improve the multi-pass recrystallisation models.

From the present work, two equations were derived that can be implemented into the NTNU model. These are equation 5.5 which describes the evolution of the S-component and equation 5.23 which describes the size of the constituent particles. The implementation of these equations into the source code of the model has been beyond the scope of the present work but could further improve the performance of the model.

To improve the possibilities to validate the NTNU model, the predicted fraction of the S-component should be included in the standard output.

A problem that is encountered when validating any texture model is that there is no accepted standard by which the volume fraction of the different texture components is calculated. It was found in the present work that the absolute values depend very much on the way (that is by which software package) they were calculated. To improve the possibilities to compare data from different research centres, it is very desirable that such a standard is developed.

A similar argument applies to SLIMMER. Firstly, the constitutive equation and the recrystallisation kinetics found for AA3104 can be inserted into the source code of SLIMMER. Furthermore, it was concluded that the modelling of lateral spread is essential to obtain correct roll force predictions for laboratory rolling. If equation 5.9 were to be built into SLIMMER, further validation work of the roll force predictions would become easier. To be able to apply the roll force predictions of SLIMMER for break-down geometries, it is also necessary that the multiplying term derived by Beese is incorporated in the model.

It is expected that a further improvement could be achieved when SLIMMER would be extended with a more sophisticated friction model.

7. References

[1] Von Nestler C.G.; **Aluminium;** *Neue Technik, Leicht Verständlich, VEB Deutscher Verlag für Grundstoffindustrie, Leipzig 1961*

[2] Hirsch J.; **Aluminium alloys for automotive application;** *Materials Science Forum, Volumes 242,1997,pp 33-50, ISBN 0-87849-757-9*

[3] Engler O., Mülders B., Hirsch J.; **Influence of deformation temperature and strain rate on the recrystallization nucleation in Al-Mn1-Mg1;** *Z.Metallkd. 87 (1996) 6 pp 454-464*

[4] Hirsch J., Grenz R.; **Microstructure control on an aluminium hot reversing finishing mill;** *Proceedings of the Second Symposium, held at The 1998 TMS Fall Meeting, Rosemont, Illinois, October 11-15, 1998, ISBN 0-87339-412-7, pp 305-316*

[5] Ennor; **U.S. Patent 2 301 027**

[6] Granger D.A.; **Ingot casting in the aluminium industry;** *in Aluminium Alloys-Contemporary Research and Applications, Treatise on materials science and technology vol 31, eds: Vasudevan A.K, Doherty R.D., Academic Press Inc, (1989), ISBN 0-12-341831-3 pp 109-134*

[7] Green J.; **Mill description & Layout;** *The technology of flat rolling course, The University of Sheffield, 5-16 September 1994, week 1*

[8] Hoyle W.C., Setlak F.R.; **Trends and Needs in Can Stock: A Packaging Company's perspective;** *JOM, 1996 November, pp 33-36*

[9] Miller W.S., Holstein R.D., Buerger A., v.d. Hoeven J., Neutjens P.; **The effect of alloy chemistry on the strength and recovery characteristics of Al-Mn-Mg-Cu alloys;** *The 4th international Conference on: Aluminum alloys Their Physical and Mechanical properties, eds. Sanders T.H. Jr. , Starke E.A. Jr., The Georgia Institute of Technology, Atlanta, GA, July, 1994, pp 484-491*

[10] Richardson G.J., Hawkins D.N., Sellars C.M.; **Worked examples in metalworking;** *The Institute of Metals, May 1985, ISBN 0-904357-77-5*

[11] Ingham P.M.; **Mechanics of Hot Rolling;** *The technology of flat rolling course, The University of Sheffield, 5-16 September 1994, week 1*

[12] Backofen, W.A.; **Deformation Processing;** *Addison-Wesley publishing company; 1972; ISBN 0-201-00388-0*

[13] Timothy S.P., Yiu H.L., Fine J.M., Ricks R.A.; **Simulation of single pass of hot rolling deformation of aluminium alloy by plane strain compression;** *Materials Science and Technology, March 1991, vol 7, pp 255-261*

[14] Yiu H.L., Fine J.M., Timothy S.P., Rogers S., Ricks R.A.; **The use of plane-strain compression testing to simulate the evolution of hot-rolled microstructures in aluminium alloys;** *Hot Deformation of Aluminium Alloys, eds. Langdon T.G., Merchant H.D., Morris J.G., Zaidi M.A., The Minerals, Metals & Materials Society, 1991, pp 509-525*

[15] Watts A.B., Ford H.; **An experimental investigation of the yielding of strip between smooth dies;** *Proceedings Institute of Mechanical Engineers, 1952, pp 448-453*

[16] Beynon J.H.; **Structural changes during Hot Working of Aluminium alloys;** *PhD-thesis, The University of Sheffield, 1979*

[17] Sellars C.M.; **Discussion on mechanical working;** *chairman Kennedy A.J., in Metals Technology August 1976, pp 387-389*

[18] Hufnagel W.; **Key to Aluminium alloys, 4th Edition;** *Aluminium Verlag Dusseldorf, 1991, ISBN 3-87017-218-5*

[19] Van Horn K.R.; **Aluminum;** *Metals Park : American society for Metals, 1967*

[20] Usui E., Inabe T., Shinano N.; **Influence of Mn and Mg additions on Hot Deformation of Aluminium and Aluminium Alloys;** *Zeitschrift fuer Metallkunde, Bd 77 (1986) H. 3 Hot Deformation of Al and Al alloys, pp 179-187*

[21] Westerman E.J.; **Silicon: a vital alloying element in aluminium beverage can body stock;** *in Aluminium alloys for packaging, ed Morris, J.G., Merchant H.D., Westerman E.J., Morris P.L., The Minerals, Metals & Materials Society, 1993, pp 1-16*

[22] Morris J.G., Li Z., Chen L., Das S.K.; **A further analysis of the earing behavior of AA3004 aluminium alloy;** *Aluminium 66. Jahrgang 1990, 11, pp 1069-1073*

[23] Spear R.E., Gardner G.R.; **Dendrite Cell Size;** *Transactions of the Amer. Foundrymen's Society 71 (1963), pp 209-215*

[24] Marshall G.J.; **Microstructural control during processing of aluminium canning alloys;** *Materials Science Forum, Volumes 217-222 (1996) ISSN 0255-5476, pp 19-30*

[25] Merchant H.D., Morris J.G., Hodgson D.S.; **Characterization of Intermetallics in Aluminium Alloy 3004;** *Materials Characterization 25:339-373 (1990)*

[26] Scott Goodrich H.; **A model for the precipitation/dissolution of Mn during commercial homogenization of Aluminium Alloy 3104;** *in Aluminium alloys for packaging, eds. Morris, J.G., Merchant H.D., Westerman E.J., Morris P.L., The Minerals, Metals & Materials Society, 1993, pp 47-60*

[27] Dillamore I.L., Katoh H.; **The mechanisms of recrystallization in cubic metals with particular reference to their orientation dependence;** *Met. Sci, 8, (1974), pp 73-83*

[28] Sanders jr. R.E., Lege D.J., Hartman T.L.; **Aluminium rigid container sheet for the packaging industry;** *Aluminium 65, Jahrgang 1989 9 pp 941-947*

[29] Daaland, O; **Development of microstructure and texture during rolling and annealing of commercial Al-Mn-Mg alloys;** *PhD-thesis The Norwegian Institute of Technology, Trondheim, Norway, 1993*

[30] Humphreys F.J., Hatherly M.; **Recrystallization and related annealing phenomena;** *Pergamon Press 1996; ISBN 008 0426859*

[31] Taylor G.I.; *Inst. Met., 62, 307, (1938)*

[32] Aernoudt E.; *Proceedings ICOTOM 5, (eds Gottstein and Luecke), Aachen, 1, 45, Springer Verlag, Berlin (1978)*

[33] Sevillano Gil J., Van Houtte P., Aernoudt E.; **Large strain work hardening and textures;** *Progress in materials science, (eds. Haasen and Masalski, 25, (1980), pp 69-412*

[34] Maurice Cl., Driver J.H.; **Hot rolling textures of f.c.c. metals-Part II Numerical simulations;** *Acta Mater. Vol 45, No 11, 1997, pp 4639-4649*

[35] Haessner F.; **Recrystallization of metallic materials;** *Stuttgart, Riederer 1978*

[36] Vatne, H.E.; **Experimental investigations and modelling of recrystallisation in two hot deformed aluminium alloys;** *PhD-thesis The Norwegian Institute of Technology, Trondheim, Norway, 1995*

[37] Reyes G.C., Beynon J.H.; **Retained strain in the modelling of the hot rolling of aluminium;** *Hot Deformation of Aluminium Alloys, eds. Langdon T.G., Merchant H.D., Morris J.G., Zaidi M.A., The Minerals, Metals & Materials Society, 1991, pp 491-508*

[38] Styles G.C.; **Static recovery in hot rolling;** *PhD.-thesis University of Leicester, November 1996.*

[39] Yamagata, H.; **Dynamic recrystallization and dynamic recovery in pure aluminium at 583 K;** *Acta Metall. Mater., 1995, 43, 723*

[40] Huang Y., Humphreys F.J.; **Transient dynamic recrystallization in an aluminium alloy subjected to large reductions in strain rate;** *Acta Mater. vol 45, No 11, 1997, pp. 4491-4503*

[41] Sellars C.M.; **Modelling microstructural development during hot rolling;** *Materials Science and Technology, November 1990, vol 6, pp 1072-1081*

[42] Sellars C.M.; **An internal state variable approach to modelling microstructural evolution during thermomechanical processing;** *proceedings of Thermec '97, Wollongong Australia, July 1997*

[43] Sellars C.M., McG. Tegart W.J.; **Hot Workability;** *Int. metals Review 1972, Review 158, vol 17, pp1-24*

[44] Nes E.; **Constitutive laws for steady state deformation of metals, a microstructural model;** *Scripta metallurgica et materialia, Vol. 33, No 2, 1995, pp 225-231*

[45] Castro-Fernandez F.R., Sellars C.M.; **Relationship between room-temperature proof stress, dislocation density and subgrain size;** *Philosophical Magazine A, 1989, Vol. 60, No 4, pp 487-506*

[46] Castro-Fernandez F.R., Sellars C.M., Whiteman J.A.; **Changes of flow stress and microstructure during hot deformation of Al-1Mg-1Mn;** *Materials Science and Technology, May 1990 Vol 6, pp 453 - 460*

[47] Nes E., Furu T.; **Application of microstructurally based constitutive laws to hot deformation of aluminium alloys;** *Scripta metallurgica et materialia, Vol. 33, No 1, 1995, pp 87-92*

[48] Furu T.; **Modelling of recrystallisation applied to commercial aluminium alloys;** *PhD-thesis The Norwegian Institute of Technology, Trondheim, Norway, 1992, ISBN 82-7119-413-5*

[49] Sellars C.M., Whiteman J.A.; **Principles of hot deformation;** *in proceedings of: Controlled Processing of HSLA steels, York 28th - 30th September 1976*

[50] Whittaker H.J.; **Hot working and recrystallisation of 3% silicon steel;** *PhD-thesis University of Sheffield, 1973, ISBN z0893593*

[51] Sellars C.M., Whiteman J.A.; **Recrystallization and grain growth in hot rolling;** *Metal Science March-April 1979, pp 187-194*

[52] Brand A.J., Bernrath G., Theisen S., Kopp R.; **Quantitative beschreibung statischer entfestigungsvorgange von aluminiumlegierungen mit hilfe von einzel- und doppelstauchversuchen;** *Aluminium 73, Jahrgang 1997,1/2, pp 76-83*

[53] Beynon J.H., Sellars C.M.; **Modelling microstructure and its effects during multipass hot rolling;** *ISIJ International. Vol 32 (1992), No. 3, pp 359-367*

[54] Caglayan H., Beynon J.H.; **SLIMMER: Sheffield Leicester integrated model for microstructural evolution in hot rolling;** *1st International Conference on Modelling of metal rolling processes, London, UK, 21-23 September 1993, pp 274-282*

[55] Sims R.B.; **The calculation of roll force and torque in hot rolling mills;** *Proc. Int. Mech. Eng., 1954, pp 191-200*

[56] Puchi Cabrera E.S.; **Effect of deformation history on the recrystallisation kinetics of Al-1%Mg alloy;** *PhD-thesis, University of Sheffield (1983)*

[57] Puchi E.S., Beynon J.H., Sellars C.M.; **Simulation of hot rolling operations on commercial aluminium alloys;** *Int. Conf. on Phys. Metallurgy of processing steels and other metals, Thermec 88, Tokyo, Iron and Steel institute of Japan, June 1988, pp 572-579*

[58] Beynon J.H.; **SLIMMER for Windows;** *Manual, version 1.03, University of Leicester 1992*

[59] Beynon J.H.; **Private communication;**

[60] Orsetti Rossi P.L.; **The 50 tonne Hille Rolling Mill;** *internal report The University of Sheffield, November 1993*

[61] Orsetti Rossi P.L.; **Effect of multi-pass deformation on te recrystallisation behaviour of commercial aluminium alloys during thermomechanical processing;** *PhD-thesis, The University of Sheffield, May 1995*

[62] Intermet; **BIMEX 400 Vacuum Formed Shape;** *Intermet Refractory Products, Oughtibridge, Sheffield S30 3HP, UK*

[63] Vatne H.E., Oscarsson A., Ekström H.E.; **Industrial hot rolling of an AA3004 alloy; experimental investigations and modelling of recrystallisation;** *Proceedings of the 6th Int. Conference on Aluminium Alloys ICAA-6, eds Sato T., Kumai S., Kobayashi T., Murakami Y., The Japan Institute of Light metals, 1998, pp 1263-1268*

[64] Oscarsson A., Ekstroem H.E., Remmelg G., Hutchinson W.B.; **Struktur och texturutveckling under varmvalsning av AA3004 och dess inverkan på Öronbildningen;** *Swedish Institute for Metals Research, sept 1993 (in Swedish)*

[65] Van Houtte P.; **The 'MTM-FHM' software system;** *Version 2, 1995, Katholieke Universiteit Leuven, Belgium*

[66] Foerster; **Sigmatest d 2.068 Software V 2.0;** *Institut Dr. Forster, Bedienungsanleitung*

[67] Underwood G.W.; **Quantitative Stereology;** *Addison Westley publ. 1970, pp 119-123*

[68] Silk N.J., van der Winden M.R.; **Interpretation of hot plane strain compression testing of aluminium specimens;** *Materials Science and Technology, March 1999 Vol 15 pp 295-300*

[69] Davenport S.B., Sparks C.N., Sellars C.M.; **Modelling Hot Rolling of C-Mn Steel using constitutive equations;** *Thermomechanical Processing in Theory, Modelling & Practice, ed W.B. Hutchinson, 1997*

[70] Gelin J.C., Ghouati O., Shahani R.; **Identification and modelling of constitutive equations for hot rolling of aluminium alloys from the plane strain compression test;** *Modelling of Metal rolling processes, ed Beynon J.H., London, Institute of Metals, 1993, p 239-255*

[71] Sellars C.M., Irisarri A.M., Puchi E.S.; **Recrystallization characteristics of aluminium - 1% magnesium under hot working conditions;** *Microstructural control in Aluminum Alloys: Deformation, Recovery and Recrystallization, eds Chia E.H., McQueen H.J., February 1985, pp 179-196*

[72] Belling J.M., McQueen H.J., Crawford B., Malin A.S.; **Static recrystallization of an Al-Mg-Mn alloy after hot torsion testing;** *Recrystallization '90, ed. Chandra T., The Minerals, metals & Materials Society, 1990, pp 655-660*

[73] Altenpohl D.G.; **Aluminium und aluminiumlegierungen,;** *New York, Springer-Verlag, 1965, library of congress catalogue card nr. 64-23061*

[74] Trømberg E.; **Phase transformations during homogenization of commercial AlMn-alloys;** *PhD-thesis The Norwegian Institute of Technology, Trondheim, Norway, February 1994*

[75] Sheppard T.; **Homogenisation;** *Course given at Hoogovens 18th/19th May 1994*

[76] Van der Winden M.R., Sellars C.M.; **Laboratory simulation of breakdown rolling of AA3104;** *Materials Science Forum, Volumes 217-222, 1996, ISSN 0255-5476, pp 385-390*

[77] Vatne H.E., Shahani R., Nes E.; **Deformation of Cube oriented grains and formation of recrystallised grains in a hot deformed commercial aluminium alloy;** *Acta met., 44,(1996), pp. 4447-61*

[78] Juul Jensen D., Shi H., Bolingbroke R.K.; **Texture development in Al 3003 during hot plane strain compression;** *Materials Science Forum Vol. 157-162 (1994) pp 745-752*

[79] Luecke K., Pospiech J., Jura J., Hirsch J.; **On the presentation of orientation distribution functions by model functions;** *Z.Metallkde Bd. 77 (1986) H. 5, pp 312-321*

[80] Billington D.E., Lees J.; **Elements of rolling practice;** *Elements of rolling practice; Sheffield, The United Steel Companies LTD, 1949, printed by Lund Humphries*

[81] Sheppard T., Wright D.S.; **Parameters affecting lateral deformation in slabbing mills;** *Metals Technology, February 1981 pp 46-57*

[82] Wilson W.R.D., Kennedy K.F.; **An analytical model for side spread in rolling of flat products;** *Proceedings 6th NAMRC Conference, pp 119-126*

[83] Helmi A., Alexander J.M.; **Geometric factors affecting spread in hot flat rolling of steel;** *Journal of The Iron and Steel Institute November 1968*

[84] Raghunathan N., Sheppard T.; **Lateral spread during slab rolling;** *Materials Science and Technology, October 1989 Vol 5 pp 1021-1026*

[85] Roberts W.L.; **Hot rolling of steel;** *Marcel Dekker, inc 1993 ISBN 0-8247-1345-1*

[86] Hastings N.A.J., Peacock J.B.; **Statistical distributions;** *London Butterworths 1975, ISBN 0-408-70568-X*

[87] Hollinshead P.A.; **Texture and mechanical property developments in aluminium alloy during hot rolling;** *PhD-thesis London University 1986*

[88] Hollinshead P.A., Sheppard T.; **Substructure morphology in aluminium alloys AA3003 and AA3004;** *Materials Science and Technology December 1987 Vol. 3 pp 1019-1024*

[89] Fukada K., Mizouchi M., Kajiyama T.; **Effect of heating rate and temperature on annealing textures of 3004 Aluminium alloy;** *Aluminium Alloys Physical and Mechanical properties pp 483-497*

[90] Andersson B., Naess S.E.; **Earing and texture in alloys AA5052 and AA3004;** *Aluminium Alloys Physical and Mechanical properties pp 499-511*

[91] Duval J.L., Teodosiu C., Courbon J.; **Microstructure-based models of the plastic behaviour of 3104 aluminium alloys;** *Materials Science Forum, Volumes 217-222, (1996) pp 1007-1012*

[92] Marshall G.J., Meredith M.W., Bolingbroke R.K.; **The effect on initial microstructure on the evolution of crystallographic texture in AA3104 during simulation of hot rolling;** *Aluminum Alloys for Packaging II, eds. Morris J.G., Das S.K., Goodrich H.S., The Minerals Metals & Materials Society, 1996, pp 73-83*

[93] Asami S., Doko T., Yagi K.; **Recrystallisation behavior during hot rolling of 3004 aluminium alloy;** *Journal Japanese Institute of Light Metals, vol 39, 1989 pp 94-100 (in Japanese)*

[94] Es-Said O.S., Morris J.G.; **The effect of second phase particles on the recrystallization behavior, texture and earing behavior of strip cast 3004 alloy;** *Aluminum Alloys - Physical and mechanical properties pp 451-470*

[95] Suni J.P. Shuey R.T., Doherty R.D.; **Dispersoid modelling in 3XXX alloys;** *Aluminum Alloys for Packaging II, eds. Morris J.G., Das S.K., Goodrich H.S., The Minerals Metals & Materials Society, 1996, pp 145-195*

8. Acknowledgements

During this work, I tried to combine laboratory simulation of break-down rolling with the computer modelling of this process. It turned out that I needed lots of help to able to do either of these. Especially the experimental work required the assistance of very many people (typically 6 for each experiment). Therefore a big thank you to: Gavin Baxter, Dave Braine, Darren Burke, John Clarke, Bruce Davenport, Dave Hanlon, Richard Kangley, Iain Todd, Ian Watts and Dimphy Wilms. Not only were these people brave enough to assist me with the rolling experiments on SMART, they also contributed greatly to the development of the experimental procedures. For instance the idea to rotate the sample after every few passes was not mine but Richard's. I would also like to thank Leo Woning from Hoogovens R&D for carrying out the texture measurements.

However, also with the modelling work, I have received a lot of help, especially from Trond Furu and Hans Erik Vatne who are now at Hydro Aluminium in Norway.

Although I do realise that the reader may become under the impression that I did not actually do a lot of work myself, there are a few other people that I want to mention here. I would like to acknowledge professor Mike Sellars, professor John Beynon and Bill Miller for the useful discussions during the course of this work.

Furthermore, financial support from Hoogovens R&D in The Netherlands is gratefully acknowledged.

I would like to specifically thank all those people who made my stay in Sheffield into a very pleasant one. Especially the support that I received from all the people in and outside the department when things got somewhat terrible, has been very important to me.

The last thank you is for Anouschka Versleijen.

Menno van der Winden

Appendix A Detailed description of SMART

Below some technical details of SMART are summarised. The technical details of the tube furnaces are as follows:

Make:	Carbolite
Controller:	Eurotherm 91e
Model:	CTF 12/150/190
Max. Temp:	1200 °C
Tube inside dia:	150 mm
Heated length:	1090 mm
Overall length:	1270 mm
Max. power:	7.0 kW
Weight:	60 kg

The working tubes have an outer diameter of 15.24 cm (6"). In these tubes a table is fixed which is welded at one end of the tube. At this end a flange is bolted onto the tube. The tube, the table and the flange are of 304 stainless and are 2.6 mm thick.

The furnaces are hung in a cradle. Figure 8.1 shows a sketch of the cradle together with its sizes. It is made from 1" Speedframe™. In the cradle there are two shelves. The bottom shelve carries the controller of the furnace and the top shelve protects the controller from any tools, specimen, etc. that might fall down. The cradles are put on castors. Firstly these enable easy positioning of the cradles. Secondly they serve as a safety feature. When the sample misses the entry of the furnace, it will hit the flange and push the furnace backwards, thus preventing the specimen from being caught in between the mill and the furnaces.

Around each furnace two steel bands are clamped (see figure 8.2). Four bolds are screw through these bands, they centre the furnace inside the band and isolate the bands from the heat of the furnace. Each band is connected to two wires (Bordon™ wire) of 2 mm diameter (i.e. 4 wires per furnace). Between the cradle and the wires there is a barrel-spanner which allows the height of the furnaces to be adjusted. Around these spanners, a spring carries most but not all of the load of the furnaces.

Figure 8.3 shows a sketch of this arrangement. The rationale behind this suspension system is as follows. Assume a specimen to bend upwards after it has entered the furnace. As soon as this happens the furnace is lifted. When the specimen tail leaves the mill the furnace will come down again. If the furnace would be on a table, the ceramic insulation and the heating elements would break when the furnace hits the table. The suspension system prevents this from happening since the springs slow down the furnace on its way down. The Bordon wires together with the barrel spanners ensure that the height of the furnace when in rest is always the same. Due to the fact that the cradle is wider than the furnace, the furnace is also self aligning in the horizontal direction.

Therefore the furnaces will align themselves automatically after each pass, and they will be ready for the next pass without any operator interference.

The wires used to move the specimen from one furnace through the mill into the opposite furnace, are made from NiCrAlloy™. To make a strong yet flexible wire, the wires are made out of two twined filaments of 0.5 mm.

The sponge used in the lubrication system is a cellulose sponge. This material proved to have the best 'heat-resisting' capacities. It typically survives 5 testing days before starting to burn away. The sponge is positioned on top of the top roll by inserting two copper tubes. These tubes are then fitted to the frame of the mill with NiCr-wires. Figure 8.4 shows a sketch of this arrangement. The lubricant is fed to the sponge via a flexible tube that is connected to a squash-bottle that holds the lubricant. From practical experience the amount of lubricant was determined. It turned out that a 'just wet' top roll, resulted in the flattest specimens.

Appendix B Interpretation of PSC results

Interpretation of hot plane strain compression testing of aluminium specimens

N. J. Silk and M. R. van der Winden

Plane strain compression (PSC) testing is now generally accepted as one of the most reliable methods for the generation of flow stress data and microstructural investigation of thermomechanical processing. It has been known for some time that extremely reproducible measurements may be made across different laboratories if a standardised procedure is used. However, particular care must be taken with both the experimental procedure and the interpretation of the measured force–displacement data. The present paper reports investigations that have built on previous work and looked further at the effects of spread of the specimen and friction. In deriving reliable flow stress data, the importance of tool and specimen geometry and consideration of the effects of lubrication and friction are clearly demonstrated. Furthermore, the paper demonstrates the current status of the work by presenting the algorithms behind new software that has been developed for interpretation of raw force–displacement data in a logical and consistent way. MST/3960

At the time the work was carried out, the authors were with IMMPETUS, The University of Sheffield, UK. Dr Silk is now with Kvaerner Metals, Prince of Wales Road, Sheffield S9 4EX, UK, and Mr van der Winden is with Hoogovens Research and Development, PO Box 10000, 1970 CA IJmuiden, The Netherlands. *Manuscript received 17 November 1997; in final form 19 June 1998.*

Introduction

There is ongoing interest in the measurement of reliable flow stress data for a wide range of materials for use in the modelling of thermomechanical processing. The plane strain compression (PSC) test was originally developed to relate to the rolling of wide plate or strip, in which (as with a number of other metal forming processes) the deformation closely relates to plane strain conditions. The test is useful for any investigation in which high strains are generated, the use of uniaxial tension would be restricted by the onset of necking, and the use of axisymmetric compression is limited by the occurrence of barrelling. Furthermore, PSC testing has the added advantage that a reasonably large volume of material is deformed in plane strain, which is suitable for microstructural investigation. The PSC test is now used extensively for flow stress determination and the investigation of microstructural development during thermomechanical processing.

At Sheffield, numerous detailed studies of a wide range of material types have been performed during the past 25 years. These have demanded the continuous evolution of both the control software and the methodology adopted to 'post-process' the data. For instance, Guerrero[1] has recently analysed the PSC test using a thermally coupled finite element model of the test. Furthermore, a great deal is understood about the interpretation of the test results, and a current project[2] at the National Physical Laboratory, Teddington, UK is concerned with formalising the test method with the aim of producing a standardised procedure.

Shi *et al.*[3] highlighted various details concerning the way corrections are made to account for friction and spread effects in the specimen. The present work has looked in more detail at these aspects, and the opportunity was taken to develop new software for post-processing the data. Several critical aspects of the test method and its interpretation are discussed, followed by a short description of the software.

Specimen and tool geometry

During hot rolling of wide plate and strip, the deformation mode is very close to ideal plane strain conditions. For this reason and from a modelling point of view, it is highly desirable to obtain this deformation mode during laboratory testing. Using slipline field analysis,[4] it has been shown that the ratio of the width of the tools to the thickness of the specimen w/h_0 needs to be at least 1·5. However, as this ratio increases, the frictional contribution increases and, although specimens are lubricated to reduce friction to a minimum, it is necessary to make careful allowance for frictional effects.

A second point of concern is the amount of lateral spread. Ideally, this should be zero, but the only way to avoid lateral spread is to use the so called channel die compression configuration[5] (*see* Fig. 1). When this configuration is used, the contact area between tools and specimen increases dramatically, compared to a traditional PSC configuration (Fig. 2), and thus the influence of friction also increases. As it is now relatively straightforward to account accurately for lateral spread, a deviation from ideal plane strain is preferred to the strong friction effects and the difficulties of rapidly quenching specimens after deformation that are associated with channel die compression. For traditional PSC testing, however, it is necessary to correct the raw data for both friction and spread effects. Both corrections are discussed in more detail below.

Spread correction

Owing to load restrictions, it is frequently impractical to use a specimen geometry for which the tool width is not a significant fraction of the specimen breadth. This leads to lateral spread of the specimen and uncertainty in the contact area over which the stress is applied. Therefore, the changing contact area between the tools and specimen throughout the test must be taken into account by using the 'instantaneous' breadth. As instantaneous breadth can not be recorded during the test, an empirical relationship must be used to interpolate between initial and final breadth. A satisfactory empirical relationship has previously been reported by Sellars *et al.*,[6] which defines a 'spread coefficient' C from the specimen dimensions before and after a test

$$C = \frac{(b_f/b_0) - 1}{1 - (h_f/h_0)^{0.5}} \quad \ldots\ldots\ldots\ldots\ldots (1)$$

ISSN 0267-0836

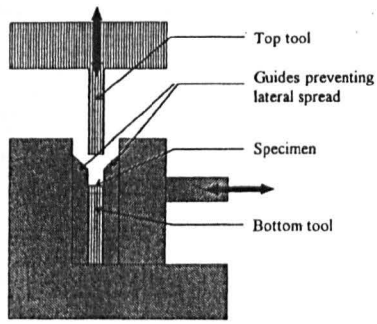

1 Schematic representation of channel die plane strain compression machine (after Ref. 5)

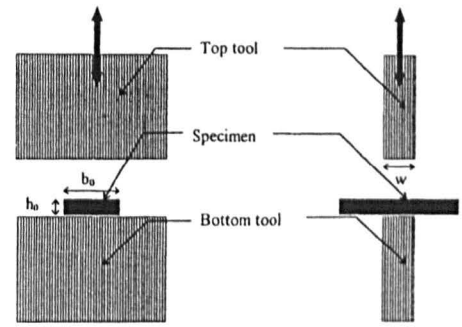

2 Schematic front and side views of 'traditional' plane strain compression setup

where b_f is the average breadth after deformation, b_0 is the average breadth before deformation, h_f is the average thickness after deformation, and h_0 is the average thickness before deformation.

More recently, Shi *et al.*[3] indicated that the exponent in equation (1) should be nearer 0·2 for aluminium specimens lubricated with graphite. Numerical analysis of a large number of aluminium specimens tested to different strains using water based graphite lubricants in place of the original oil based lubricants has required the exponent in equation (1) to be modified to 0·18. Using the adjusted equation, the instantaneous breadth b_{inst} is currently estimated using

$$b_{inst} = b_0 \left[1 + C - C\,(h_{inst}/h_0)^{0.18}\right] \quad . \quad . \quad . \quad . \quad . \quad . \quad . \quad (2)$$

where h_{inst} is the instantaneous thickness, calculated from the output of the displacement transducer during the test.

Lubrication and friction

Ideally, there should be no friction between the tools and the specimen. This would result in a measured load response that is solely determined by the resistance of the specimen to deformation. Teflon (PTFE) tape approaches this situation most closely, but its temperature stability is limited to 350°C and, in practice, a water based graphite lubricant is found to be most suitable for the testing of aluminium.

Originally, it was believed that only oil based graphite lubricants were suitable,[6,7] but more recent experiments have shown that modern water based lubricants yield acceptable and reproducible lubrication, without the problems associated with oil burning off when reheating the specimen. A problem with any form of lubrication is that the lubricant increases the effective thickness of the specimen, which makes it difficult to determine the start of deformation unambiguously. This aspect will be discussed in the section below concerning 'Origin correction'.

To determine the flow stress of the material, the instantaneous pressure must first be calculated from the instantaneous load. The load exerted by the ram L_{inst} is converted to an average instantaneous pressure $\bar{p}_{inst}$ using the instantaneous breadth b_{inst}

$$\bar{p}_{inst} = L_{inst}/wb_{inst} \quad . \quad . \quad . \quad . \quad . \quad . \quad . \quad . \quad . \quad . \quad . \quad . \quad (3)$$

The maximum shear flow stress can then be deduced from the instantaneous pressure depending on whether the friction conditions are predominantly sliding friction, sticking friction, or a combination of the two. Sliding friction assumes a constant Coulomb friction coefficient, whereas sticking friction assumes the contact stress at the tool/specimen interface to be equal to the material flow stress in pure shear. Different friction conditions may occur in different regions of the contact area at the same time. In this case, it is assumed that the lubrication causes each type of behaviour to occur in distinct bands across the width of the specimen.

As mentioned above, a ratio w/h of greater than 1·5 is required to ensure plane strain conditions but, as this ratio increases, so the effect of friction increases. Increased friction between the tools and the specimen increases the pressure required to produce yielding.

Hill[8] derived an approximation for the conditions during rolling that may also be applied to PSC testing. Assuming small values of μ (sliding friction) and $w > h$, Rowe derived an expression to describe the average pressure exerted by the tools in terms of the shear flow stress k (Ref. 9)

$$\frac{\bar{p}}{2k} = \frac{h}{\mu w}\left[\exp\left(\frac{\mu w}{h}\right) - 1\right] \quad . \quad . \quad . \quad . \quad . \quad . \quad . \quad . \quad . \quad . \quad (4)$$

where μ is the friction coefficient. For sticking friction conditions, relative movement of the specimen and tools is by shearing of the material at the interface rather than sliding between the specimen surface and the tool surface. However, a modified form of the analysis enables a similar expression for sticking friction conditions to be derived

$$\frac{\bar{p}}{2k} = 1 + \frac{w}{4h} \quad . \quad . \quad . \quad . \quad . \quad . \quad . \quad . \quad . \quad . \quad . \quad . \quad . \quad . \quad (5)$$

It is to be noted that equations (4) and (5) are only valid when either sliding or sticking friction conditions apply over the entire tool face. However, there may be an intermediate situation when the sticking condition exists only in the central region and the outer edges have sliding friction conditions. The position where the friction changes from sliding to sticking friction conditions z_0 may be found by equating the dp/dx terms of the equations for sliding and sticking friction. This yields

$$z_0 = \left(\frac{h}{2\mu}\right)\ln\left(\frac{1}{2\mu}\right) \quad . \quad . \quad . \quad . \quad . \quad . \quad . \quad . \quad . \quad . \quad . \quad . \quad (6)$$

The friction conditions become 'partially sticking' if $w > 2z_0 > 0$. It is notable that z_0 is dependent on the thickness of the specimen. The average pressure in terms of shear stress is then

$$\frac{\bar{p}}{2k} = \frac{h}{\mu w}\left(\frac{1}{2\mu} - 1\right) + \frac{(w/2) - z_0}{\mu w} + \frac{[(w/2) - z_0]^2}{hw} \quad . \quad . \quad . \quad . \quad . \quad . \quad . \quad . \quad . \quad (7)$$

In practice, there will always be some spread which relaxes the frictional effects at the edges of the specimen. Orowan and Pascoe[10] accounted for this effect for the case of sticking friction. They suggested that, at large specimen breadths, the correction is relatively insignificant, but if the breadth is less than six to eight times the specimen thickness, such a correction becomes essential. Owing to the constraints of the present testing setup, the correction for spread of the specimen can not be ignored as, typically, $b = 5h$.

The method used by Orowan and Pascoe can be extended to derive expressions for all frictional conditions, and this leads to additional terms in each of the friction equations, which may be summarised as follows.[11]

If $2z_0 > w$ (sliding friction)

$$\frac{\bar{p}}{2k} = \frac{1}{bw}\left[\frac{2h^2}{\mu^2} + \frac{(b-w)h}{\mu}\right]\left[\exp\left(\frac{\mu w}{h}\right) - 1\right] - \frac{2h}{\mu b} \quad \ldots\ldots\ldots (8)$$

If $w > 2z_0 > 0$ (partial sticking friction)

$$\frac{\bar{p}}{2k} = \frac{h}{\mu w}\left(\frac{1}{2\mu} - 1\right) + \frac{(w/2) - z_0}{\mu w} + \frac{[(w/2) - z_0]^2}{hw} + \frac{1}{\mu b}\left(\frac{2z_0^2}{w} - z_0 - \frac{2hz_0}{\mu w} + \frac{h}{2\mu} - h + \frac{h^2}{w\mu^2} - \frac{2h^2}{\mu w}\right) + \frac{1}{hb}\left(z_0^2 - \frac{4z_0^3}{3w} - \frac{w^2}{12}\right) \quad \ldots\ldots\ldots (9)$$

If $0 > 2z_0$ (sticking friction)

$$\frac{\bar{p}}{2k} = 1 + \frac{w}{4h} - \frac{w^2}{12hb} \quad \ldots\ldots\ldots (10)$$

Modern computers enable these calculations to be performed routinely at very high speed; thus, the new program includes the full friction equations as described above, z_0 being computed at each increment throughout the test using the instantaneous thickness. The value of z_0 is then used to determine which friction conditions prevail, and instantaneous values of breadth and thickness are substituted into equations (8), (9), or (10) to determine the instantaneous mean pressure.

The flow stress σ of the material is then calculated using the same empirical correction factor f as for strain, discussed below, from

$$\sigma = \frac{2k}{f}(3/2)^{1/2} \quad \ldots\ldots\ldots (11)$$

Origin correction

As stated above, the application of lubricants complicates the determination of the start of specimen deformation. The PSC machine at the University of Sheffield was initially used mainly for deformation of steel specimens at high temperature (>800°C). In this temperature region, graphite can not be used and, normally, glass lubricants are applied, which are up to 0·2 mm in thickness before deformation. To correct for the effect of excess glass being squeezed from the specimen/tool interface at the very beginning of the deformation, a method was originally proposed by Colas-Ortiz.[12] This method corrects for the initial curvature in the load–displacement plot and has also been applied to aluminium tests.[13]

In recent tests conducted entirely on aluminium specimens with and without graphite lubricant, it was found that the graphite layers are so thin (<0·02 mm) that 'squeezing out' does not significantly influence the load response. Indeed, it was found that there was some uncertainty in the origin even when testing unlubricated specimens. These experiments showed that any ambiguity in the origin arises from the tools being slightly misaligned from front to back (i.e. the tool faces not being perfectly parallel, *see* Fig. 2), and/or the specimen not being perfectly parallel across its width. The error introduced by these phenomena is ~0·05 mm (for a specimen 50 mm in width). Therefore, it is believed that the method appropriate to correct for the squeezing out of the lubricant, which 'artificially' cleans up any effect of misalignment, is not justified for graphite lubrication. Obviously, the effect of this 'misalignment' disappears on subsequent deformations of the same specimen, where the specimen has deformed to the shape of the tools, as can be seen in Fig. 3.

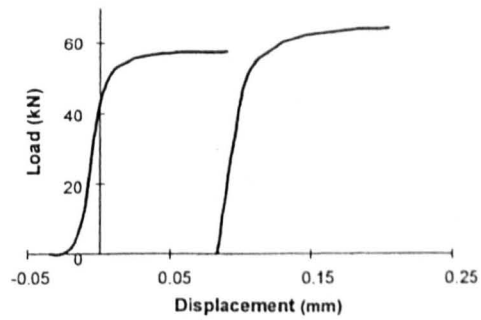

3 Example of load–elongation curve for double deformation test carried out at 450°C and 2·5 s^{-1}

Therefore, the only correction applied to the raw data should be for possible errors in the zero position. This is done by measuring the mean thickness of the specimen after deformation at a minimum of eight points across the width. This value is then corrected for the thermal expansion of the specimen. (Thermal expansion must also be taken into account when calculating the initial thickness of the specimen from the 'cold' measurements.) From the initial and final 'hot' thicknesses, the maximum displacement of the tool $d_{measured}$ is derived. This is compared with the maximum displacement recorded by the displacement transducer on the PSC machine d_{raw}^{max}. Any discrepancy between these two values is now corrected for by shifting the load–displacement curve in such a way that the maximum actuator displacement is equal to the maximum measured displacement

$$d_{corr} = d_{raw} + (d_{raw}^{max} - d_{measured}) \quad \ldots\ldots\ldots (12)$$

Either procedure implies that any elastic deformation and the precise stress at the onset of plastic deformation σ_0 is difficult to determine accurately. Although the method proposed by Colas-Ortiz suggests a less ambiguous σ_0, it is not applicable to graphite lubricated tests.

Calculation of strain

If the equivalent tensile strain $\bar{\varepsilon}$ in the specimen after deformation is calculated assuming ideal plane strain conditions, i.e. $\varepsilon_1 = -\varepsilon_3$ and $\varepsilon_2 = 0$, then

$$\bar{\varepsilon} = \frac{\sqrt{2}}{3}[(\varepsilon_1 - \varepsilon_2)^2 + (\varepsilon_2 - \varepsilon_3)^2 + (\varepsilon_3 - \varepsilon_1)^2]^{1/2} \quad \ldots (13)$$

That is

$$\bar{\varepsilon}^{ideal} = \frac{2}{\sqrt{3}} \ln \frac{h}{h_0} \quad \ldots\ldots\ldots (14)$$

However, $\varepsilon_3 = \ln(h/h_0)$, $\varepsilon_2 = \ln(b/b_0)$, and $\varepsilon_1 = -\varepsilon_2 - \varepsilon_3$, accounting for lateral spread. Substituting gives

$$\bar{\varepsilon} = \frac{\sqrt{2}}{3}[(2\varepsilon_2 + \varepsilon_3)^2 + (\varepsilon_2 - \varepsilon_3)^2 + (\varepsilon_2 + 2\varepsilon_3)^2]^{1/2} \quad (15)$$

Therefore, the equivalent tensile strain is

$$\bar{\varepsilon} = \frac{2}{\sqrt{3}}(\varepsilon_2^2 + \varepsilon_2\varepsilon_3 + \varepsilon_3^2)^{1/2} \quad (16)$$

i.e. because ε_2 is related to ε_3 by equation (2), f can be defined by

$$\bar{\varepsilon} = f\left(\frac{2}{\sqrt{3}}\varepsilon_3\right) \quad (17)$$

Equation (17) can be used after the test to convert the values of instantaneous thickness into equivalent strain. However, during a test, it is necessary to calculate the instantaneous equivalent strain online. This requires a very simple algorithm, as (even very modern) control systems can not process the 'log function' quickly enough. Therefore, a nominal factor f' is calculated for use during the test from the initial breadth of the specimen and the tool width

$$f' = \frac{2/\sqrt{3}(b-w) + w}{b}\frac{\sqrt{3}}{2} \quad (18)$$

This first estimate is then replaced by f from equation (17) during the post-processing of the data (offline). The stress–strain curve derived from the load–displacement data of Fig. 3 is shown in Fig. 4*a*.

Instantaneous strain rate

Many existing PSC machines do not have a velocity transducer and the ram velocity can not be measured online. In this case, the instantaneous strain rate at each time increment is calculated from the derivative of the polynomial fitted to the strain–time curve. Using the Gauss method, an individual second order polynomial is fitted for each point on the curve, using the five points before and after the defined point.

At the beginning of the dataset, there are insufficient points that lie before the first few points; thus, the curve is fitted to the nine points following. A similar problem occurs at the end of the file where the previous nine points are fitted but, in both cases, the initial data points are recorded before (or after) the tools come into contact with the specimen and, thus, they have no influence on the strain rate calculation during the deformation itself.

Load–elongation compensation

The PSC testing machine with the PSC tools at Sheffield has an actual machine stiffness of $\sim 330\,\mathrm{kN\,mm^{-1}}$ (although this varies slightly as a function of temperature), which implies that, at maximum load, the machine frame and tooling will stretch more than 1·5 mm. The control system incorporates an electronic circuit that automatically accounts for the stretch in the machine frame and adjusts the ram displacement as load is applied. The magnitude of the correction to the displacement readings is proportional to the instantaneous load and, in general, analog correction for this effect is made online during the test by applying load–elongation compensation (LEC). However, for stress relaxation testing, it is essential to perform tests without LEC, which makes the machine appear infinitely different, and to correct the displacement readings during subsequent data analysis. This has been allowed for in the new analysis software.

This load–elongation compensation circuit is calibrated by bringing the tools together without a specimen between them. The machine is gradually loaded to its full capacity and the change in displacement reading is noted as a function of load. The amount of compensation is varied through a helipot, and the required amount of compensation is that which does not lead to any variation in the displacement readings as the machine is loaded to full capacity. When properly compensated in this way, the machine effectively becomes infinitely stiff. The calibration is found to be moderately sensitive to the test temperature and must be repeated each time a new temperature is used.

Temperature measurement

Temperature is usually measured by implanting a metal sheathed, ceramic insulated thermocouple in the specimen. All thermocouples are calibrated against a secondary standard before each test at the temperature of interest. Ideally, the thermocouple is located directly in the centre of the deformation zone during the test, although it may be shifted during the course of deformation. At the beginning of a test, the tip of the thermocouple may not be in perfect thermal contact with the specimen and the recorded temperature may 'lag' slightly behind the true local temperature. However, in most cases, the deformation ensures very close thermal contact is established at strains of less than 0·2.

However, a thermocouple only measures the temperature at one specific place in the specimen. To obtain an overview of the temperature throughout the specimen, a validated finite difference model has been developed.[13] The model is capable of predicting the gradients of temperature within the testpiece, which are important when considering the temperature along the slipline field and the effects on the local microstructure. The relevance when interpreting PSC data is to realise that deformation takes place at the mean temperature of the volume undergoing deformation, rather than simply at the temperature recorded by the thermocouple.

New software

The methods used to interpret PSC data discussed above form the basis of a new Visual Basic software program. The program is primarily concerned with fast, reliable interpretation of raw data on a step by step basis, but is also useful when interpreting data produced using non-standard testing procedures.

The output files from the PSC machine contain input data and the output signals in an encoded form. The input information describes the details of the test such as the strain, strain rate, and temperature. The output signals are the load, displacement, command signal, and temperature. The output signals are recorded at a constant clock frequency and, thus, real time is not recorded, but inferred from the clock frequency.

On loading the file, the output signals are loaded into arrays and then immediately decoded into a further four arrays. Each time the data in an array are modified, a new array is created leaving the original array unmodified. All arrays are reported in the output file from the program. This has the advantage that the effect of all corrections can be observed and any errors, such as entering incorrect values of machine compliance, activation energy for deformation Q_{def}, or final specimen thickness, can be detected.

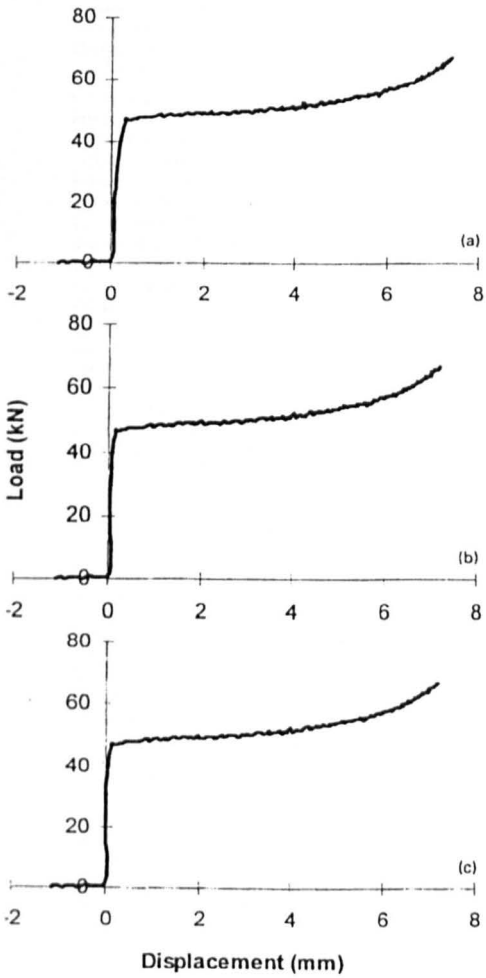

a raw; *b* corrected for machine compliance; *c* after origin correction

4 Load–displacement data for aluminium alloy 6082, at 350°C and 0·5 s^{-1}

The temperature signal recorded online is in microvolts, which are converted to degrees Celsius assuming use of a K type thermocouple during testing. As the calibrated thermocouple used during the test may incorporate a small error, provision has been made to account for this as a global modification to the decoded temperature signal.

Selection of a 'material type' assumes default values for the thermal expansion coefficient (typically $\sim 23 \times 10^{-6}\,K^{-1}$, for aluminium alloys) and Q_{def} (typically 156 kJ mol^{-1}), both of which can be modified. Using the cold final dimensions of the testpiece, the thermal expansion coefficient enables automatic calculation of the hot dimensions and, subsequently, the spread coefficient, which is a function of the hot mean breadth and hot final thickness.

Each of the corrections to the raw data is made in fixed order then 'disabled' once completed by the user. This ensures that the user can not repeat a correction accidentally or perform corrections out of order. Following each correction, the user is able to observe its effect by comparing graphically the values before and after correction. Examples

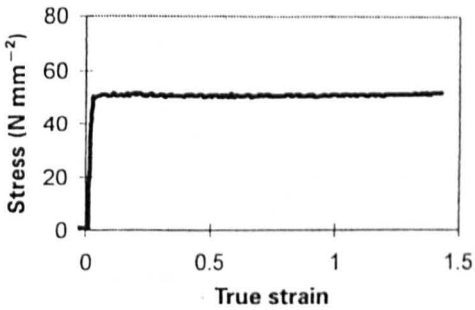

5 Stress–strain curve for aluminium alloy 6082, at 350°C and 0·5 s^{-1}

of these plots are shown in Fig. 4 for a single deformation test, performed at 350°C and a strain rate of 0·5 s^{-1} and to a nominal strain of 1·5. Figure 4*a* shows the raw load–displacement data before any correction.

The LEC is performed first if this was not made online during the test. This corrects the displacement readings for stretch of the machine frame in proportion to the instantaneous load, as can be seen in Fig. 4*b*. Next, the 'origin' correction is made, which ensures that measured final specimen thickness and recorded maximum displacement signal coincide. This is shown in Fig. 4*c*. Using the spread coefficient, displacement data can be used to compute the instantaneous breadth at each time increment throughout the test. This in turn enables calculation of the f factor, which accounts for the deviation from ideal plane strain conditions, and, thus, the equivalent tensile strain can be determined.

The instantaneous breadth is also used to determine the instantaneous pressure. From determination of z_0 at each increment throughout the test, the friction conditions that prevail may be calculated. This enables the instantaneous pressure to be converted into a shear stress, which in turn can be used to calculate the equivalent tensile stress using the f factor. The stress–strain curve is shown in Fig. 5, the distinct rise in the flow stress being as a result of the specimen rapidly losing heat to the tools.

The instantaneous strain rate is computed by fitting a second order polynomial to the strain–time curve over five data points each side of the reference point. This curve is then differentiated to give the strain rate evolution.

Using Q_{def}, the activation energy for deformation, instantaneous values of the Zener–Hollomon parameter Z may be calculated, using

$$Z = \dot{\varepsilon} \exp\left(\frac{Q_{def}}{RT}\right) \quad \ldots\ldots\ldots\ldots\ldots\ldots \quad (19)$$

where R is the universal gas constant and T is temperature. A further array of the smoothed $\partial\sigma/\partial\varepsilon$ function is also calculated. This describes the instantaneous slope of the stress–strain curve, which may be used to create Kocks–Mecking plots, and permits estimation of the steady state value of flow stress. This information is used to enable fitting of constitutive equations to the data as described elsewhere.[14,15]

The output file is written in comma separated format suitable for use in spreadsheet packages. It includes all of the information contained in the original output file from the machine, both scalar and output signals unmodified along with each array created by the program. A 'macro' has been written which allows the output files to be loaded into Microsoft Excel, and which generates graphical output from the information.

Conclusions

Some important aspects that should be considered during interpretation of plane strain compression (PSC) data for aluminium alloys have been discussed. In particular, these include correction of raw data for the effects of lateral spread and friction, which shows the importance of using carefully aligned tools and accurately ground specimens to minimise the uncertainty in determining the start of deformation. The details of the interpretation form the basis for new software which can be used to 'post-process' raw plane strain compression data in a systematic and reliable manner. This incorporates new features whereby the operator can 'post-process' a load–elongation compensation (LEC) for tests where this has not been performed online. Furthermore, any calibration errors in the thermocouple readout can be corrected during post-processing.

The friction equations have been analysed in three dimensions, taking into account the finite breadth of the specimen. Modified equations for slipping, sticking, and partial sticking friction are presented.

To account for lateral spread of the specimen during testing, a modified form of the empirical 'spread' equation has been developed which more closely fits experimental data.

The procedure proposed by Colas-Ortiz to determine the start of deformation of the specimen was shown not to be applicable to water based graphite lubricants. In this case, the initial slope of the stress–strain curve has been shown not to be caused by the squeezing out of the lubricant, as is the case for glass lubricants, but instead, the result of a slight front to back misalignment of the tools. As it represents the actual deformation of (parts of) the specimen, it is believed to be better not to correct for this effect. Obviously, this will make the precise determination of the stress at very low or zero strain difficult.

Finally, the f factor used to determine the deviation from ideal plane strain conditions has been redefined. When the deformation is plane strain, $f = 1$. Furthermore, the value of f used during the post-processing of the data is now based on the von Mises criterion rather than upon empiricism. The empirical equation incorporating f' is still used online.

Acknowledgements

The authors would like to thank Professor C. M. Sellars for many useful discussions during the course of this work and Dr G. J. Baxter for his contribution to the understanding of spread effects. The authors would also like to acknowledge the financial support of Materials Forum (NJS) and that of Hoogovens Research and Development, The Netherlands (MRvdW).

References

1. M. GUERRERO: PhD thesis, University of Sheffield, UK, 1996.
2. 'Materials measurements which affect processability, 1996–1999', MMP4, 'Thermomechanical behaviour during metals processing', Department of Trade and Industry, London, 1996.
3. H. SHI, A. J. McLAREN, C. M. SELLARS, R. SHAHANI, and R. BOLINGBROKE: *J. Test. Eval.*, 1997, **2**, 61–73.
4. W. A. BACKOFEN: 'Fundamentals of deformation processing', 1972, London, Addison-Wesley.
5. C. MAURICE and J. H. DRIVER: *Acta Metall. Mater.*, 1993, **41**, 1653–1664.
6. C. M. SELLARS, J. P. SAH, J. H. BEYNON, and S. R. FOSTER: Report on research work supported by SRC Grant B/RG/1481, University of Sheffield, UK, 1976.
7. J. H. BEYNON: PhD thesis, University of Sheffield, UK, 1978.
8. R. HILL: 'The mathematical theory of plasticity'; 1950, Oxford, Clarendon Press.
9. G. W. ROWE: 'An introduction to the principles of metalworking'; 1965, London, Edward Arnold.
10. E. OROWAN and K. J. PASCOE: Iron and Steel Institute Special Report No. 34, London, 1946, 124.
11. N. J. SILK: 'Derivation of friction equations for plane strain compression testing', Internal report, University of Sheffield, UK, September 1997.
12. R. COLAS-ORTIZ: PhD thesis, University of Sheffield, UK, 1983.
13. S. R. FOSTER: PhD thesis, University of Sheffield, UK, 1981.
14. S. B. DAVENPORT, C. N. SPARKS, and C. M. SELLARS: in 'Thermomechanical processing in theory, modelling and practice (TMP) 2', (ed. W. B. Hutchinson *et al.*), 249–257; 1997, Stockholm, Swedish Society for Materials Technology.
15. S. B. DAVENPORT, N. J. SILK, C. N. SPARKS, and C. M. SELLARS: 'Development of constitutive equations for the modelling of hot rolling', to be published.

Table 2.1 Typical data for industrial break-down rolling

Capacity [7]	400 000 tpa
Start Temperature	550 °C
Final Temperature	450 °C
Number of passes	12-25
Roll diameter	580-970 mm
Initial thickness of the slab	550 mm
Final thickness of the slab	30 mm
Strain per pass	(-)0.06 to (-)0.5
Total Accumulated strain	(-)3.5
Average strain rate	1-10 s^{-1}
Inter pass time	12-180 s

Table 2.2 Typical parameters for tandem rolling

Capacity [4]	up to 600 000 tpa
Entrance Temperature	400 - 450 °C
Exit Temperature	300 - 350 °C
Number of passes	2 - 5
Initial thickness of the slab	15 - 25 mm
Final thickness of the slab	2 - 3 mm
Typical strain per pass	1
Max. accumulated strain	3
Average strain rate	10-100 s^{-1}
Inter stand time	1-3 s

Table 2.3 Window of chemical compositions of Al-1Mn-1Mg and published compositions from different suppliers

Supplier	Ref.	code	Si	Fe	Cu	Mn	Mg	Ti	Zn	Al
Limits of AA3104	[18]	3104	<0.6	<0.8	0.05-0.25	0.8-1.4	0.8-1.3	<0.10	<0.25	bal
Limits of AA3004	[18]	3004	<0.30	<0.70	<0.25	1.0-1.5	0.8-1.3		<0.25	bal
Hoogovens Material A (this work)		3104	0.19	0.29	0.20	0.89	1.05	0.008	0.01	97.37
Material B (this work)		n/a	0.23	0.35	0.16	0.91	1.24			97.1
Hydro	[36]	3004	0.21	0.30	0.15	0.91	1.15			bal
Gränges	[64]	3004	0.20	0.50	0.17	1.00	1.29	0.019	0.03	bal
Ravenswood aluminium	[26]	3104	0.2	0.4	0.15	1.00	1.05			bal
ALCOA	[87] [88]	3004	0.18	0.41	0.12	1.10	1.01	0.04		bal
Sky Aluminium	[89]	3004	0.20	0.45	n/a	1.05	1.20			bal
ÅSV Nordisk Aluminium	[90]	3004	0.14	0.50	0.17	1.05	0.92			bal
Pechiney	[91]	3104	0.2	0.2	0.15	1	1			bal
Alunorf	[92]	3104	0.2	0.4	0.18	0.9	1.2			bal
Alcan	[16]	n/a	0.14	0.48	0.24	1.00	1.08			bal
Furukawa Aluminium Co.	[93]	3004	0.16	0.50	0.14	1.07	1.07	0.01	0.01	bal
VAW	[3]	3004	0.15	0.4	0.15	1	1			bal
RWTH	[52]	3004	0.21	0.14	4.16	0.54	1.37	0.02	0.04	bal
Comalco	[72]	3004	n/a	0.37	0.22	0.96	1.23			bal
Alloy for stripcasting	[94]	3004	0.25	0.43	n/a	1.05	1.04			bal

Table 3.1 Technical details of the laboratory mills

Mill	Hille 50	Robertson
Maximum load	50 tonnes	N/A
Maximum gauge	50.1 mm	30 mm
Maximum width	200 mm	200 mm
Maximum torque	3366 Nm	N/A
Roll radius	68.2 mm	123.8 mm
Speed	2-63 rpm	30 rpm
Minimum reversing time when running at max. speed	12 s	30 s

Table 3.2 Overview of the different experimental series

Series	Material	Schedule	Homogenisation treatment	Lubrication	Set point tube furnace	Objective
1	A	9-pass	separated	No	750 °C	Introductory tests
2a	A	14-pass	integrated	Yes	750 °C	Industrial schedule
2b	A	14-pass	separated	Yes	750 °C	Influence of homogenisation treatment
2c	A	14-pass	integrated	Yes	650 °C	Influence of rolling temperature
2d	B	14-pass	integrated	Yes	750 °C	Influence of chemical composition
3	A	7-pass	separated	No	n/a	Check validity of spread equations for a different roll radius

Table 3.3 Nine pass rolling schedule (Test series 1)

Pass no.	Final gauge [mm]	Strain of last pass	Average strain rate [s^{-1}]	Inter-stand time after n^{th} pass [s]
0	39.2	--	--	--
1	35.9	0.10	2.90	15
2	32.7	0.11	3.12	15
3	29.4	0.12	3.50	15
4	26.1	0.14	3.92	15
5	22.9	0.15	4.37	15
6	19.6	0.18	5.12	15
7	16.3	0.21	6.07	15
8	13.1	0.25	7.31	15
9	9.8	0.34	9.56	15
cumu -lative		1.6		135

Table 3.4 Fourteen pass rolling schedule (Test series 2a-2d)

Pass no.	Final gauge [mm]	Strain	Average strain rate [s-1]	Δ	Average Deformation temperature [°C]	Interstand time after nth pass [s]	Average Annealing temperature [°C]
equation		(2.2)	(2.7)	(2.8)			
0	58.6	--	--	--		--	550
1	50.1	0.18	1.13	0.91	540	12	540
2	48.2	0.05	1.14	0.87	535	12	540
3	43.4	0.12	1.26	0.78	530	12	530
4	38.7	0.13	1.40	0.70	525	12	525
5	34.0	0.15	1.58	0.62	520	12	520
6	29.3	0.17	1.82	0.54	518	15	515
7	24.6	0.20	2.14	0.46	512	15	505
8	19.8	0.25	2.60	0.38	505	15	490
9	15.1	0.31	3.31	0.31	470	15	460
10	11.3	0.33	3.91	0.25	457	30	450
11	7.6	0.46	5.52	0.19	455	50	450
12	4.7	0.55	7.39	0.15	425	100	460
13	3.2	0.44	8.30	0.13	450	180	470
14	2.2	0.43	10.14	0.08	450	120	470
cumulative		3.79				600	

Table 3.5 Seven pass rolling schedule, Robertson Mill (Test series 3)

Pass no.	Final gauge [mm]	Strain of last pass	Δ
0	20	--	--
1	19	0.06	1.75
2	18	0.06	1.66
3	17	0.07	1.57
4	15	0.14	1.01
5	13	0.17	0.89
6	10	0.30	0.59
7	7	0.41	0.43

Table 3.6 Experimental conditions for Plane strain compression tests

No	Temperature [°C]	Strain rate [s^{-1}]	Z [s^{-1}]
1	280	0.01	5.46E+12
2	280	1	5.46E+14
3	280	50	2.73E+16
4	330	0.01	3.28E+11
5	330	1	3.28E+13
6	330	50	1.64E+15
7	380	0.01	3.02E+10
8	380	1	3.02E+12
9	380	50	1.51E+14

Table 4.1 Specific roll force measurements and predictions

Pass no.	Measured roll force [kN/m]	Slimmer prediction (for Al-1Mg) [kN/m]	Corrected Slimmer for AA3104 [kN/m]
1	1302	442	854
2	795	229	443
3	1229	349	674
4	1166	369	711
5	1069	396	762
6	1276	418	803
7	1280	546	1048
8	1407	509	975
9	1462	647	1233
10	1536	668	1272
11	1915	752	1417
12	2174	887	1664
13	1476	612	1156
14	1529	555	1048

Table 4.2 Microstructural characterisation during the 9 pass schedule (series 1)

Pass no.	Resistivity [Ωm]	Fraction Cube	Fraction S
0	4.67E-08	3.50%	10.03%
1	4.69E-08	4.34%	19.10%
2	4.69E-08	3.95%	21.65%
3	4.68E-08	3.73%	22.21%
4	4.67E-08	4.27%	24.85%
5	4.65E-08	4.35%	26.34%
6	4.65E-08	4.95%	27.99%
7	4.64E-08	3.80%	28.54%
8	4.64E-08	3.80%	31.03%
9	4.58E-08	3.39%	31.81%

Table 4.3 Microstructural characterisation during the standard 14 pass schedule (series 2a)

Pass no	recr. [%]	Average grain size of the recrystallised grains [µm]	Resistivity [Ωm]	Cube	S
0	0	140	5.52E-08	1.00%	6.90%
5	0	-	5.19E-08	1.30%	7.10%
6	5	70	5.23E-08	1.30%	7.40%
7	10	60	5.18E-08	1.31%	6.53%
8	7	50	5.01E-08	1.23%	5.99%
9	3	-	5.38E-08	1.40%	6.99%
10	20	60	5.13E-08	2.09%	8.90%
11	60	40	5.19E-08	1.73%	7.14%
12	90	52	5.02E-08	3.83%	7.28%
13	100	67	5.10E-08	4.13%	15.18%
14	100	33	4.74E-08	3.54%	15.97%

Table 4.4 Microstructural characterisation during low temperature 14 pass schedule (series 2b)

Pass no	Recrystallised [%]	Resistivity [Ωm]	Cube	S
0	0	4.67E-08	1.00%	6.90%
8	3.33%	4.66E-08	1.70%	14.40%
10	7.33%	4.50E-08	1.60%	12.60%
12	81.67%	4.58E-08	5.80%	4.80%
14	100%	4.53E-08	3.90%	5.40%

Table 4.5 Microstructural characterisation during 14 pass schedule with separate homogenisation treatment (series 2c)

Pass no	Recrystallised [%]	Resistivity [Ωm]	Cube	S
0		5.52E-08	1.00%	6.90%
13	100%	5.05E-08	5.10%	6.30%

Table 4.6 Microstructural characterisation during 14 pass schedule on Material b (series 2d)

Pass no	Recrystallised [%]	Resistivity [Ωm]	Cube	S
0	0 %	5.08E-08	2.45%	8.95%
8	5 %	5.08E-08		
10	7 %	5.06E-08	2.05%	8.25%
11	100 %	5.03E-08		
12	100 %	5.00E-08	2.70%	4.30%

Table 4.7 Size distribution parameters of the constituent particles

		$\bar{\eta}$ [m]	H [m^{-3}]	L [m^{-1}]	N_0 [m^{-3}]
Material A (series 2a)	as-homogenised	1.96E-06	1.97E+15	8.13E+05	1.23E+15
	after 10 passes	2.03E-06	6.23E+14	5.54E+05	5.53E+14
	after 14 passes	2.36E-06	8.00E+15	1.18E+06	2.86E+15
Material B (series 2d)	as-homogenised	1.94E-06	1.37E+15	6.74E+05	1.05E+15
	after 10 passes	1.57E-06	1.45E+15	9.13E+05	1.01E+15

Table 4.8 Flow stress data 10-pass material

Temperature [°C]	Strain rate [s^{-1}]	Iso-thermal Flow stress at ε=0.1 [MPa]	Iso-thermal steady state flow stress [MPa]
270	0.01	110	110
320	0.01	80	79
370	0.01	54	53
270	1	137	154
320	1	99	112
370	1	88	91
270	50	144	165
320	50	128	141
370	50	113	123

Table 4.9 Flow stress data transfer gauge material

Temperature [°C]	Strain rate [s^{-1}]	Iso-thermal Flow stress at ε=0.1 [MPa]	Iso-thermal steady state flow stress [MPa]
300	0.25	111	117
400	0.25	64	66
300	2.5	128	137
400	2.5	82	85
300	25	135	150
400	25	97	104

Table 4.10 Sigma(Z) (steady state) parameters for the present experimental results and some values from the literature

Parameter	Equation	Present work		Castro-Fernandez [46]	Andersson et al. [64]	
		10-pass	Transfer	Transfer	Cast	11-pass
β_2^{ss} [m^2/MN]	2.12	0.129	0.096	0.09	0.122	0.111
$\ln A_2^{ss}$	2.12	16.12	19.58	21.5	18.17	19.19
β_3^{ss} [m^2 /MN]	2.13	0.051	0.077			
n_3^{ss}	2.13	1.88	1.15			
$\ln A_3^{ss}$	2.13	22.8	20.96			

Table 4.11 Sigma(Z) (ε=0.1) parameters for the present experimental results and some values from the literature

Parameter	Equation	Present work		Castro-Fernandez [46]
		10-pass	Transfer	Transfer
$\beta_2^{0.1}$ [m^2/MN]	2.12	0.252	0.251	0.13
$\ln A_2^{0.1}$	2.12	18.75	18.75	20.4

Table 4.12 Data used for the SLIMMER simulations

Material properties	
Alloy	Al-1Mg
Convection coefficient	0.00267 kW/m^{2}K
Emissivity	0.63
Roll properties	
Heat transfer coefficient	12.5 kW/m^{2}K
Temperature	50 °C

Table 4.13 Modelling constants used in the NTNU-model

Equation	Parameter	Value
2.19	C_1	0.026
2.19	C_2	0.06
2.38	C_C	0.24
2.39	C_{PSN}	0.18
2.42	C_{GB}	0.09

Table 5.1 Deformation parameters of the 1-10 pass and the 13th pass

Pass	ε	$\bar{\dot{\varepsilon}}$ [s^{-1}]	$\bar{T}_{def}$ [°C]	$\bar{Z}$ [s^{-1}]
1-10	1.64	2.41	495	9.82E+10
13	0.39	8.30	450	1.55E+12

Table 5.2 Four models (equations 5.6, 5.7, 5.8 and 5.9 applied to the fourteen pass rolling schedule

Model			Raghunathan	Sheppard	Helmi	present work
equation			5.5	5.7	5.6	5.9
pass no	h_0	h_f	$b_{predicted}/b_0$	$b_{predicted}/b_0$	$b_{predicted}/b_0$	$b_{predicted}/b_0$
	[mm]	[mm]				
0	--	--	1.000	1.000	1.000	1.000
1	58.6	0.050	1.035	1.006	1.032	1.028
2	50.1	0.048	1.036	1.007	1.033	1.035
3	48.2	0.043	1.052	1.009	1.047	1.051
4	43.4	0.039	1.074	1.013	1.063	1.066
5	38.7	0.034	1.107	1.016	1.083	1.082
6	34.0	0.029	1.157	1.020	1.106	1.097
7	29.3	0.025	1.239	1.026	1.133	1.113
8	24.6	0.020	1.394	1.034	1.168	1.129
9	19.8	0.015	1.720	1.045	1.208	1.145
10	15.1	0.011	2.358	1.062	1.244	1.157
11	11.3	0.008	4.870	1.104	1.286	1.170
12	7.6	0.005	34.021	1.298	1.323	1.179
13	4.7	0.003	79592.10	0.311	1.341	1.184
14	3.2	2.2	#NUM!	0.000	1.353	1.188

Table 5.3 Performance indicators of two spread models

Model	Remarks	Equation	s	s_{rel}
			[mm]	[%]
Present work	$C^{spread} = 0.19$	5.9	1.29	1.98
	$C^{spread}_{nonlubricated} = 0.14$ $C^{spread}_{lubricated} = 0.20$	5.9	1.08	1.66
	$C^{spread}_{nonlubricated} = 0.14$ applied to the results of the Hille and the Robertson mill	5.9	2.28	3.51
	$C^{spread}_{nonlubricated} = 0.14$ $C^{spread,Robertson}_{nonlubricated} = 0.29$	5.9	1.44	2.22
Helmi and Alexander. [83]		5.6	3.89	5.53
	applied to the results of the (non-lubricated tests) on the Hille and the Robertson mill	5.6	2.80	5.96

Table 5.4 Model predictions of both runs of the NTNU-model

	Assuming As homogenised constituent particles					Assuming '14 pass' constituent particles				
		Distribution of nuclei					Distribution of nuclei			
Pass no	f_{rex} [%]	Cube [%]	PSN [%]	Grain boundaries [%]	D_{rex} [μm]	f_{rex} [%]	Cube [%]	PSN [%]	Grain boundaries [%]	D_{rex} [μm]
0	0	1	0	0	140	0	1	0	0	140
1	0	0	0	0	--	0	0	0	0	--
2	0	0	0	0	--	0	0	0	0	--
3	0	0	0	0	--	0	0	0	0	--
4	0	0	0	0	--	0	0	0	0	--
5	0	0	0	0	--	0	0	0	0	--
6	5.8	4.5	60.8	34.7	50.1	0	1	0	0	--
7	12.7	4.4	65.9	29.7	55.4	8.2	3	3	94	55.9
8	18.5	4.3	74.2	21.5	48.3	9.7	2.9	7.3	89.7	49.1
9	5.2	4.1	83.3	12.5	20.3	0	1	0	0	--
10	0	1	0	0	--	0	1	0	0	--
11	0	1	0	0	--	0	1	0	0	--
12	100	4.5	64.6	30.9	45.5	100	2.7	10.4	86.8	48.3
13	100	5.5	77.5	17	55.2	100	4.2	20.4	75.4	74.5
14	100	5.1	84.4	10.6	43.9	100	4.8	46.2	49	65.1

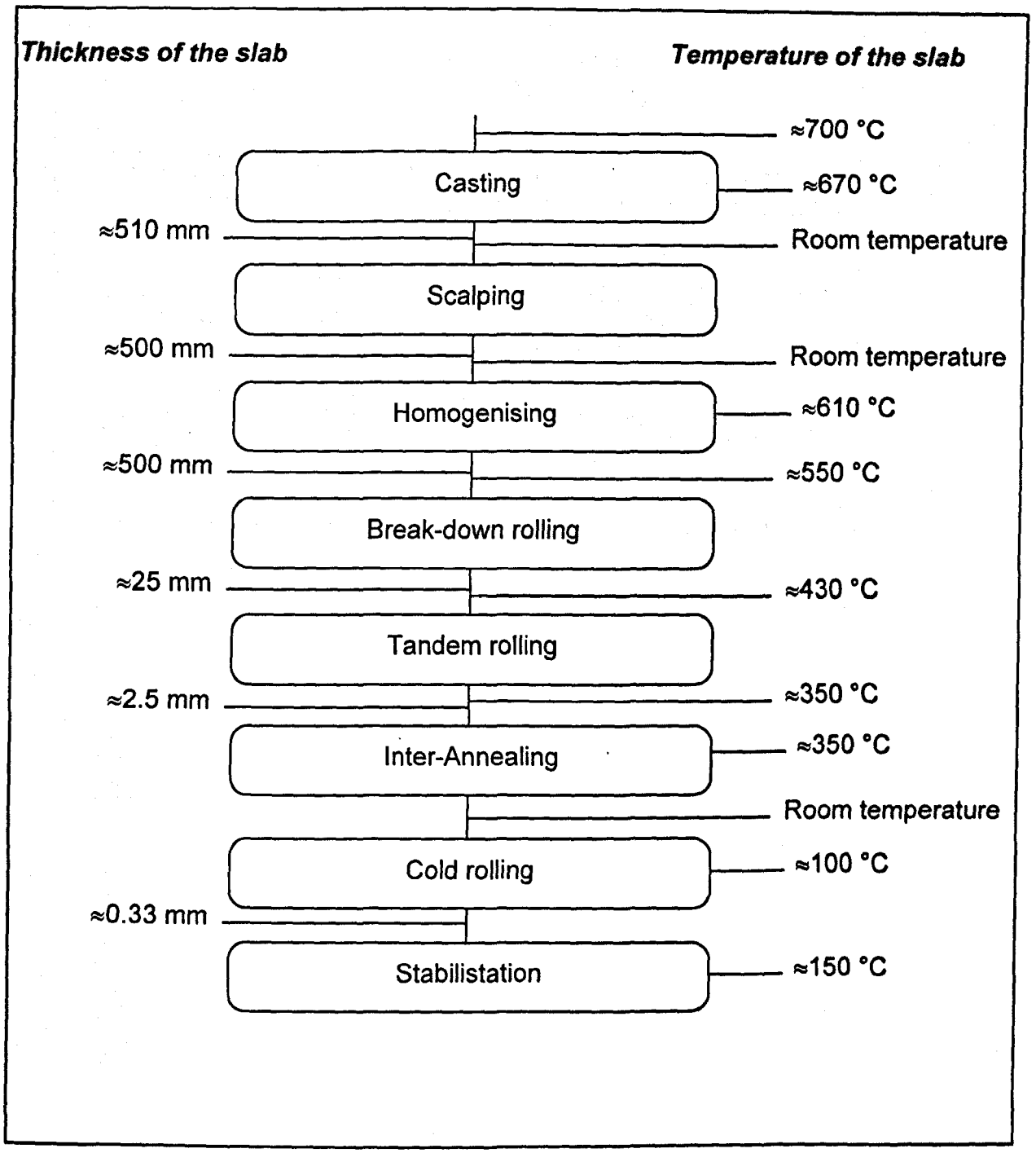

Figure 2.1: Typical flow chart of the production process of can body stock

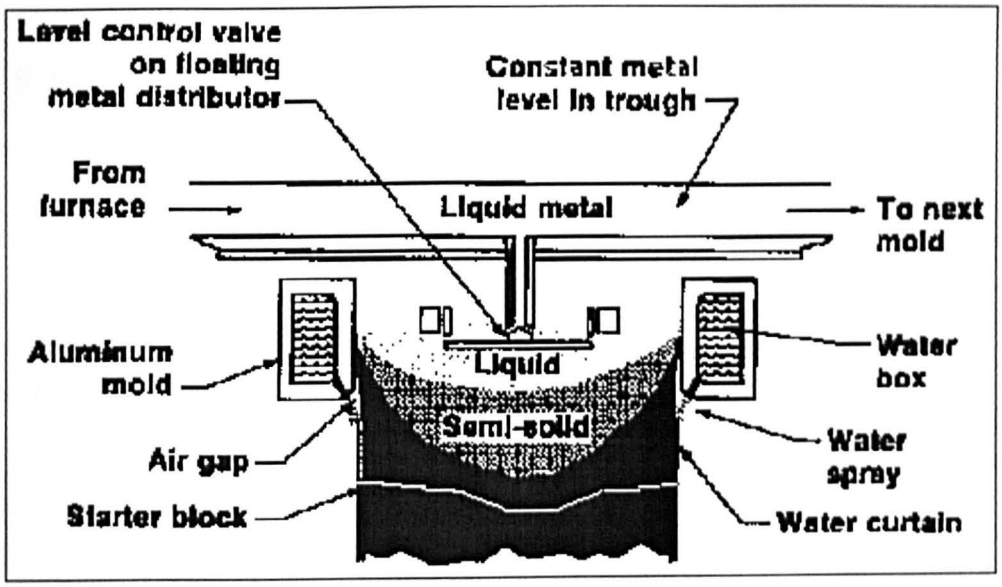

Figure 2.2 Schematic section of the top end of a DC caster (taken from [6])

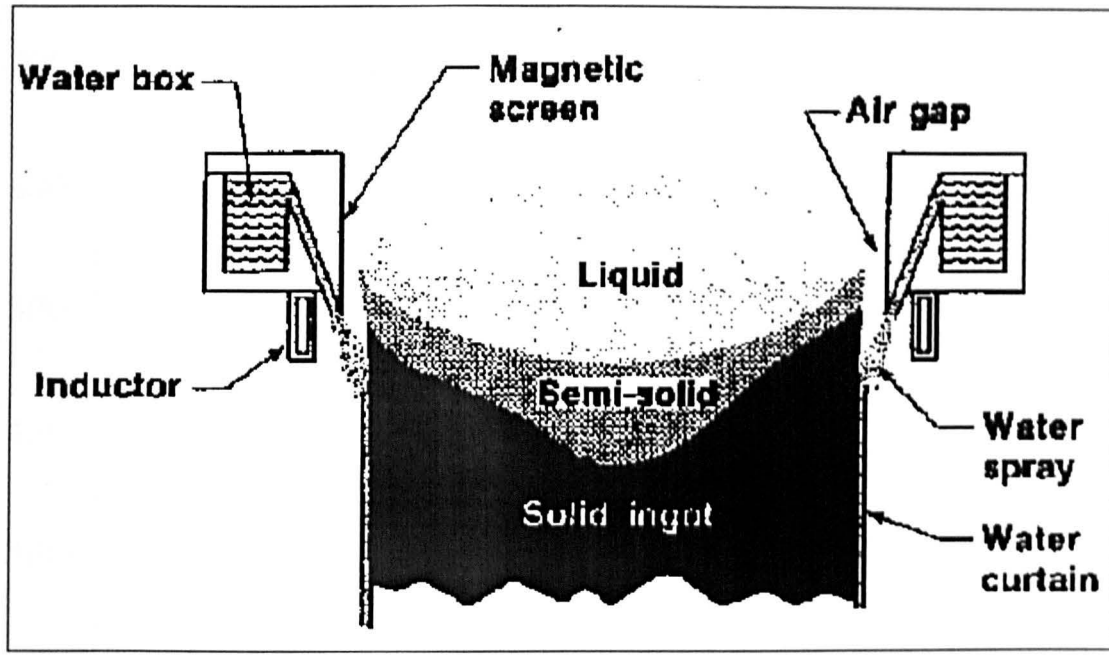

Figure 2.3 Schematic section of an EMC caster (taken from [6])

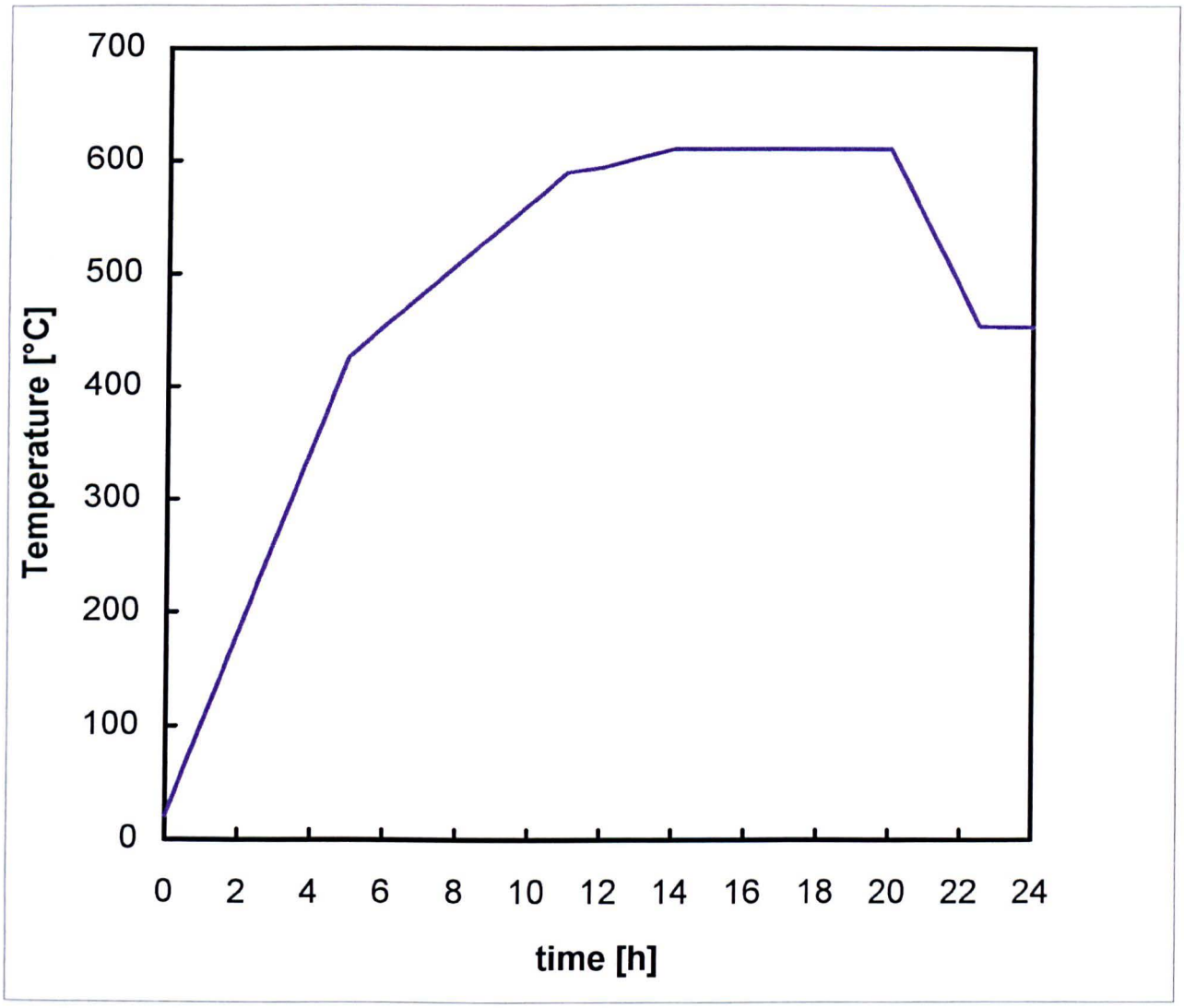

Figure 2.4 Typical temperature history during homogenisation of AA3104

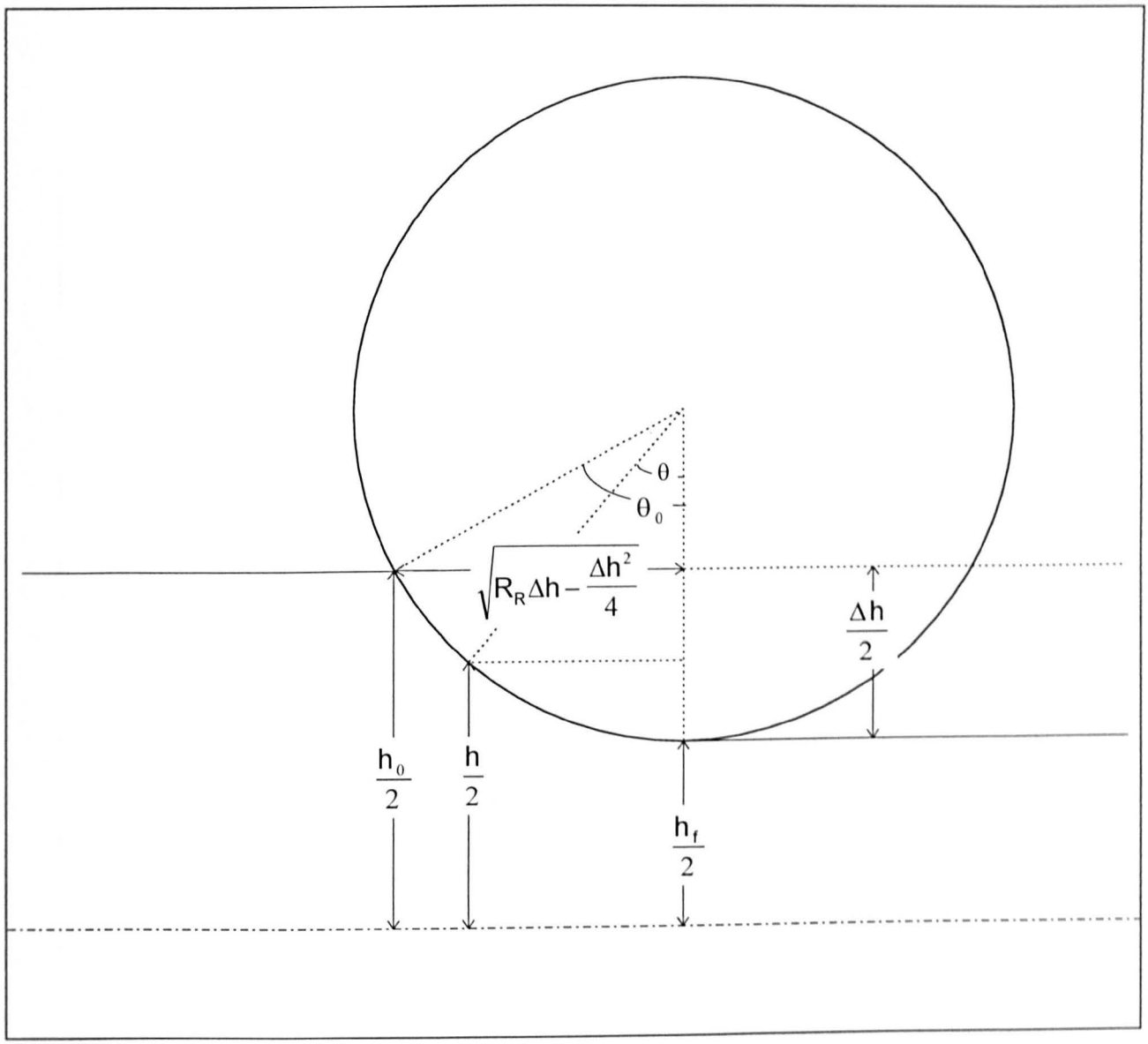

Figure 2.5 Roll gap geometry, after [10]

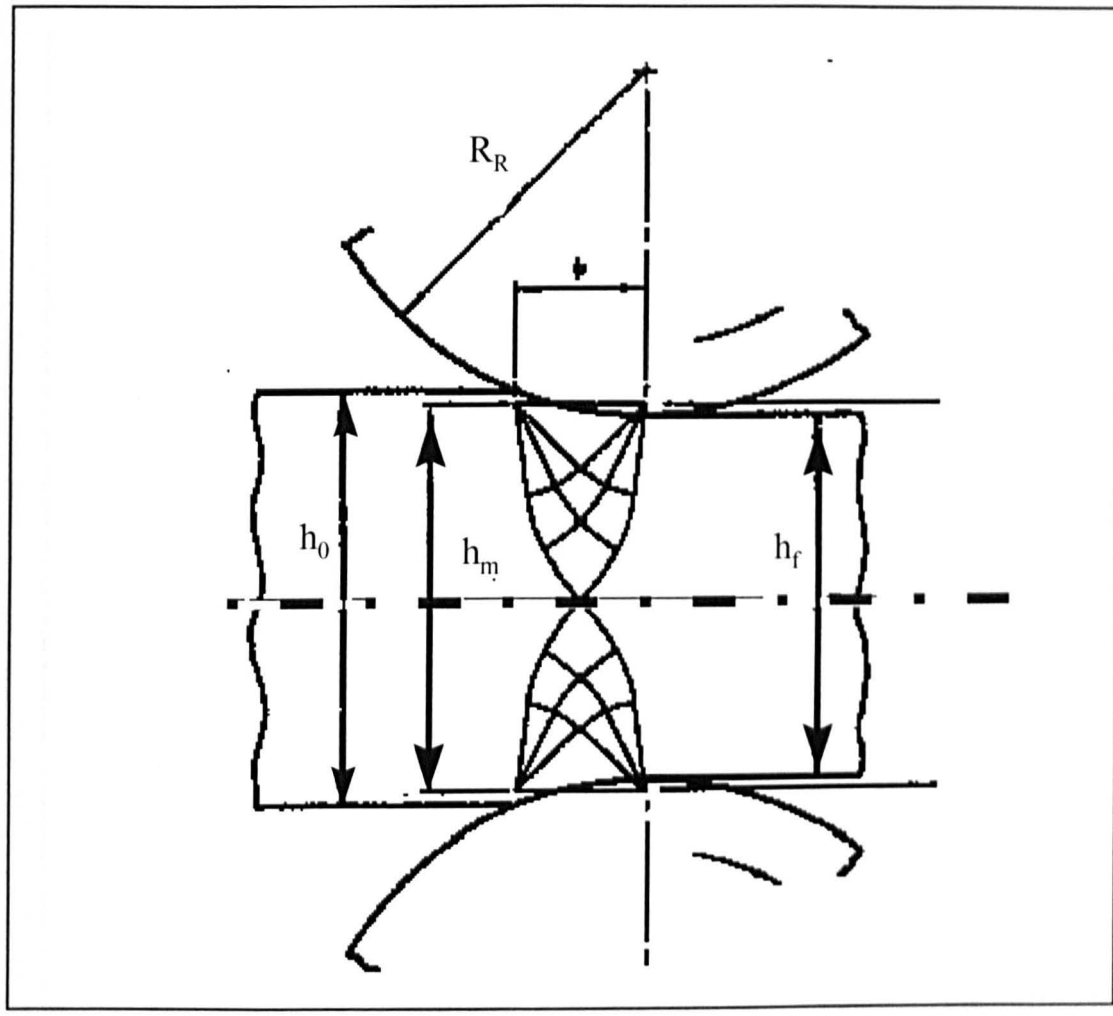

Figure 2.6 Slip line field analysis of break-down rolling (after [11])

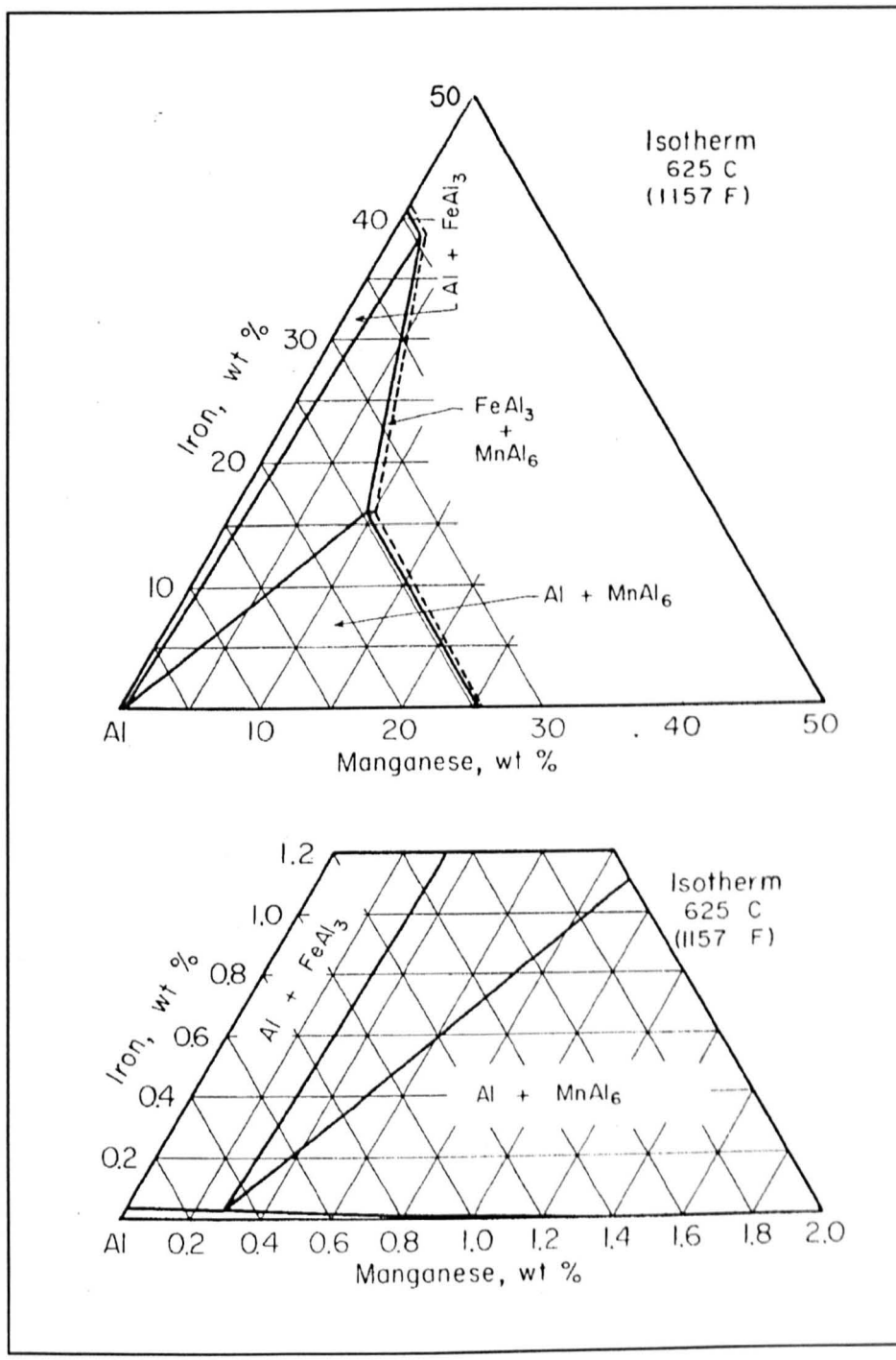

Figure 2.7 Al-Mn-Fe Phase diagram, taken from [19]

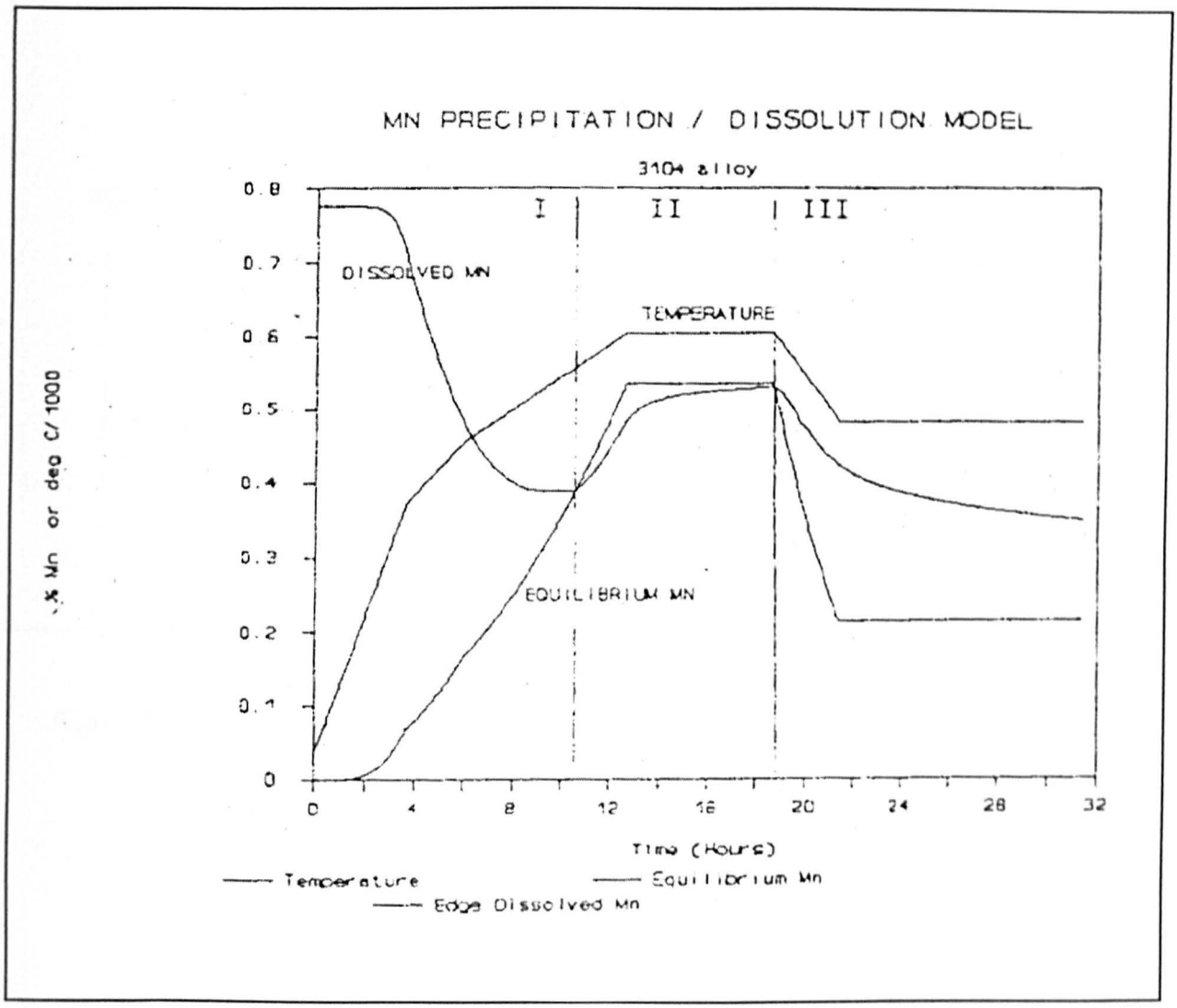

Figure 2.8 Mn precipitation as function of the homogenisation conditions (taken from [26])

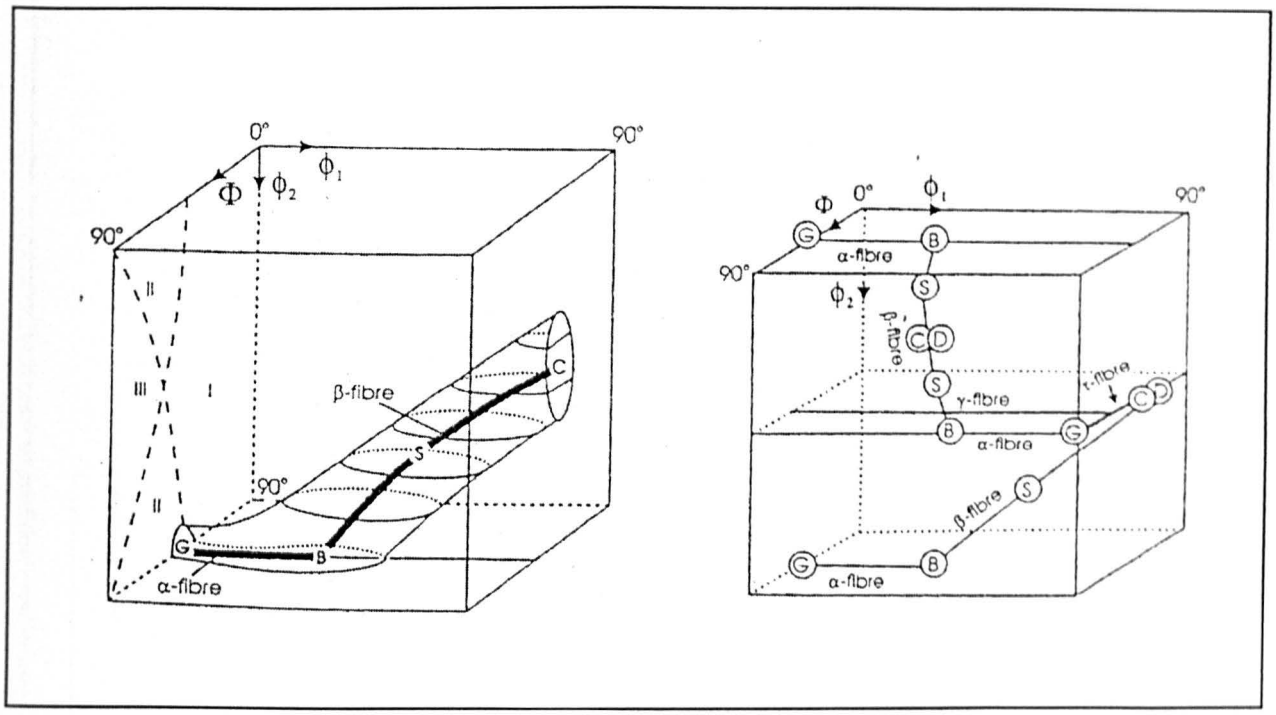

Figure 2.9 Fibre orientations in the Euler space

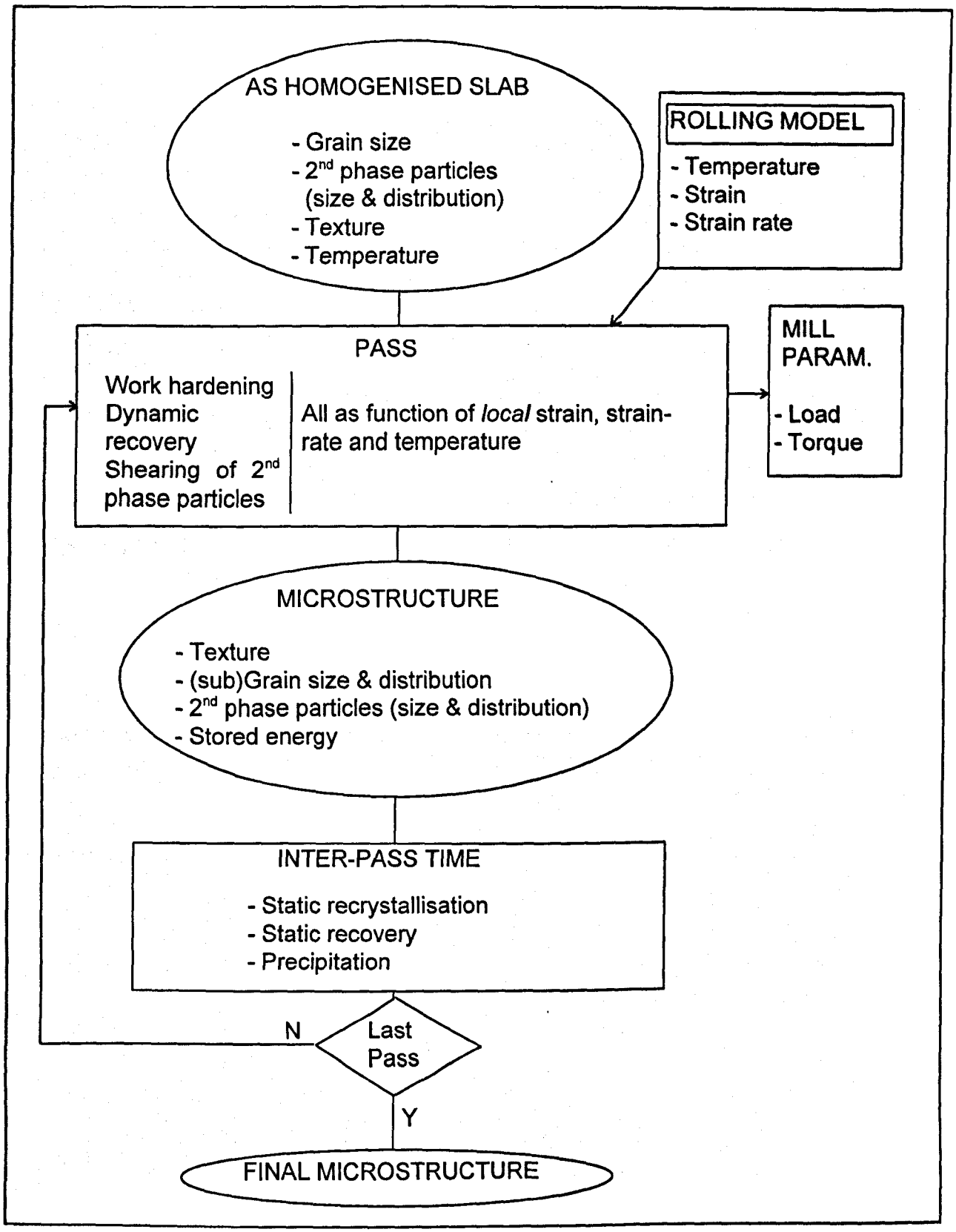

Figure 2.10 Flow chart of a multi-pass model that describes the microstructural evolution during break-down rolling

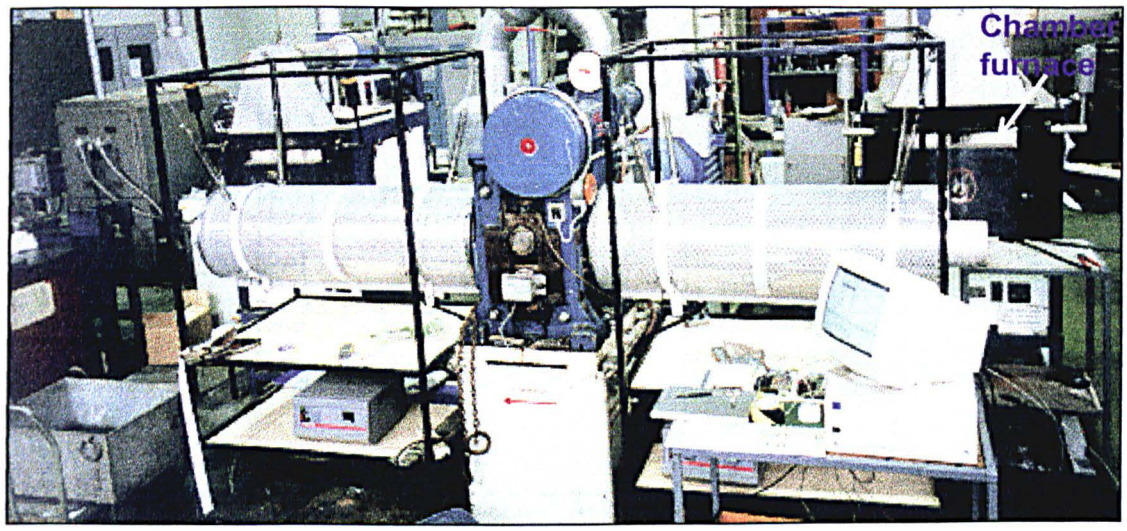

Figure 3.1a Photograph of the Sheffield Mill for Aluminium Roughing at Temperature (SMART)

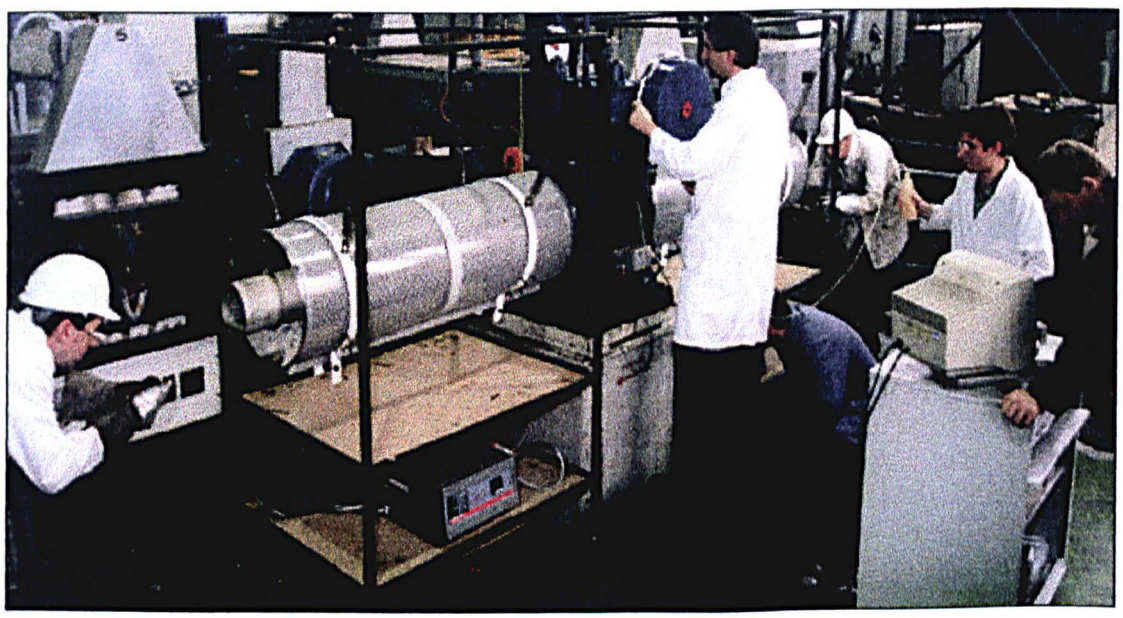

Figure 3.1b Photograph of SMART being used

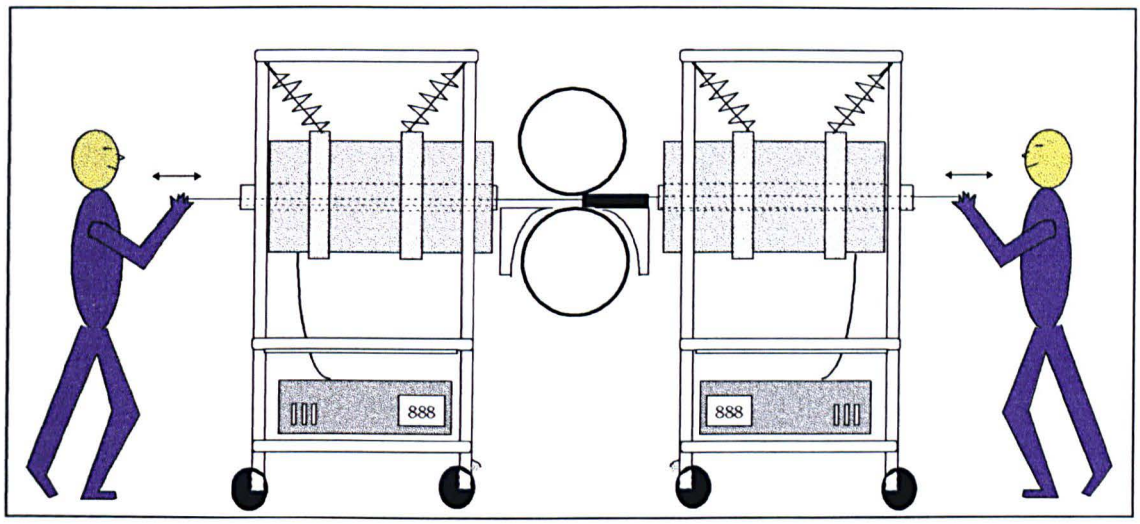

Figure 3.2 Schematic drawing of the Sheffield Mill for Aluminium Roughing at Temperature

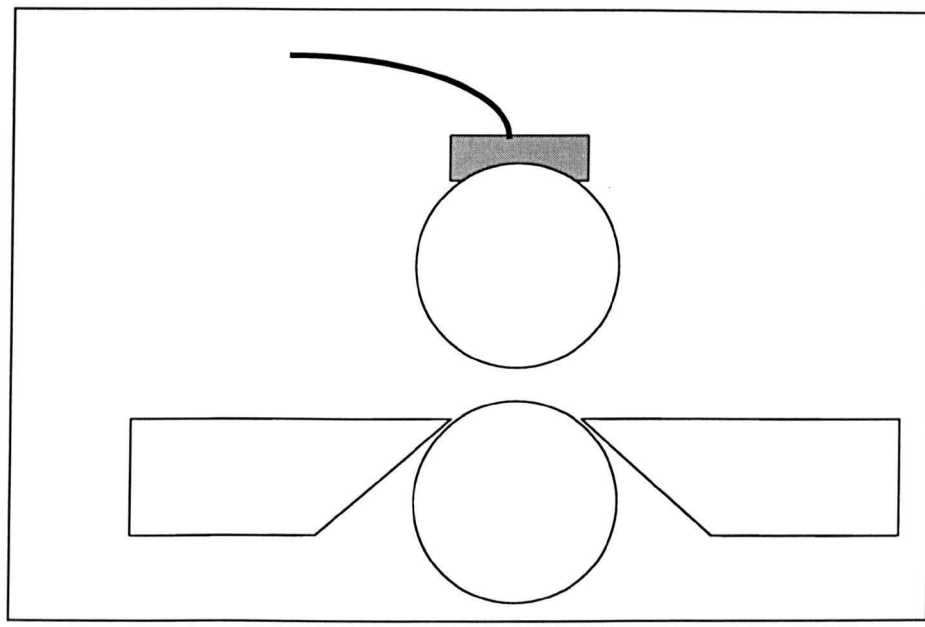

Figure 3.3 Schematic representation of the rolling mill. Also shown, the adjacent tables and the sponge through which the lubricant is fed onto the top roll.

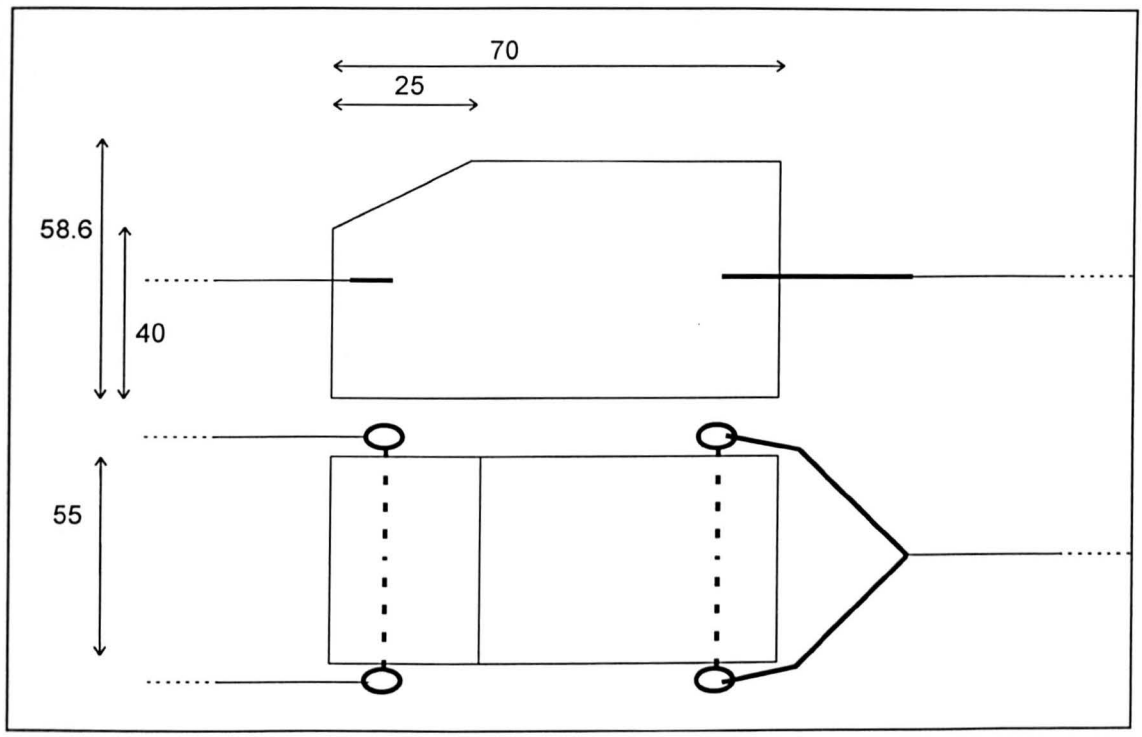

All sizes in mm.

Figure 3.4 Drawing of the specimen before the first deformation, including attached Nichrome wires.

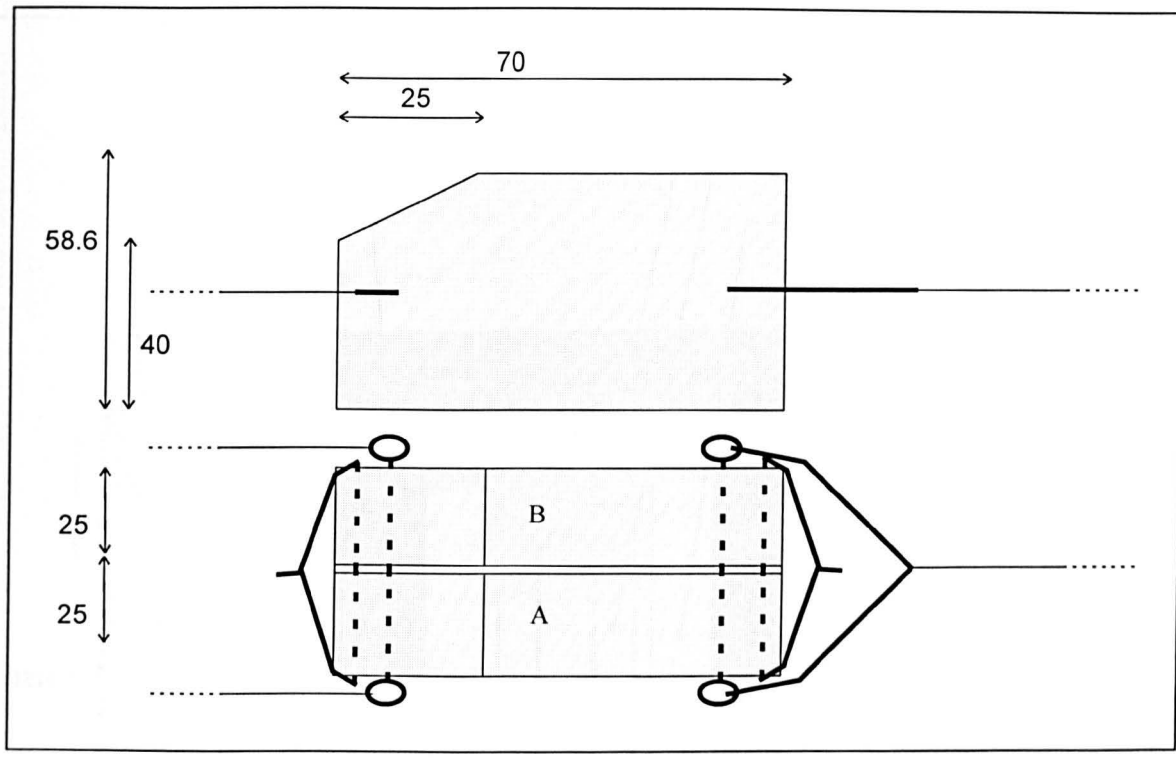

All sizes in mm.

Figure 3.5 Drawing of the tandem configuration as used for material B. Each sample consists of two pieces of metal (A and B) which are held together by an extra set of Nichrome wires.

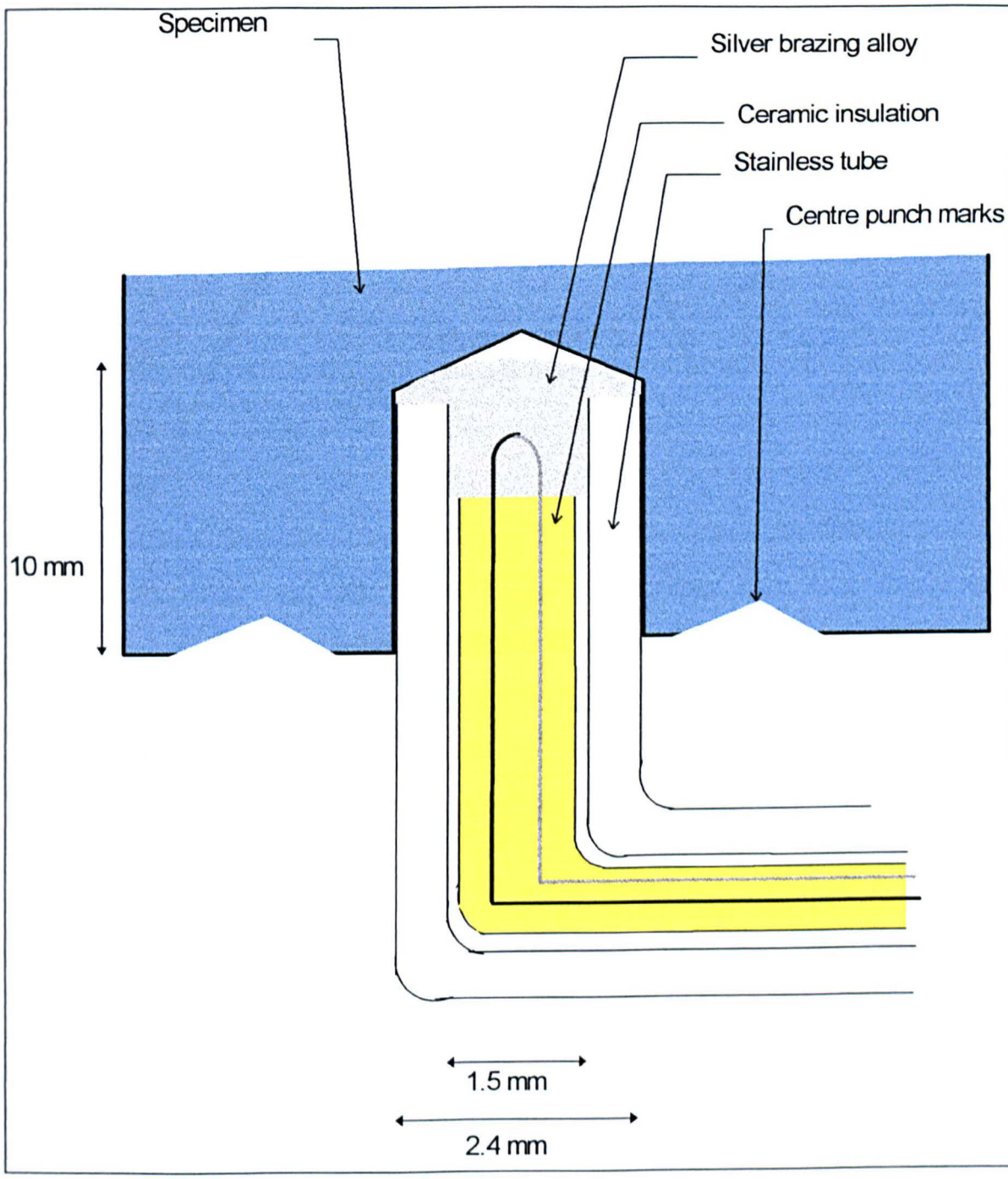

Figure 3.6 Schematic representation of a sectioned thermocouple tip inserted in a specimen

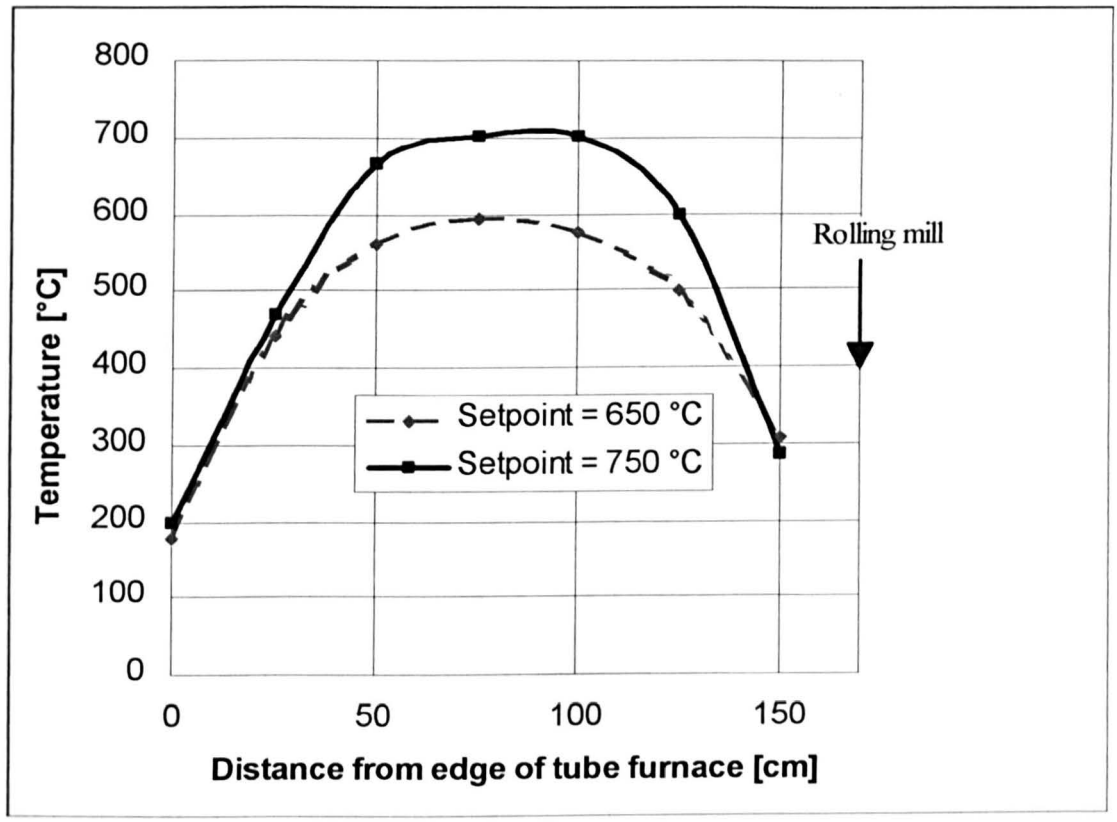

Figure 3.7 Temperature profiles of the tube furnaces at two different furnace set-points

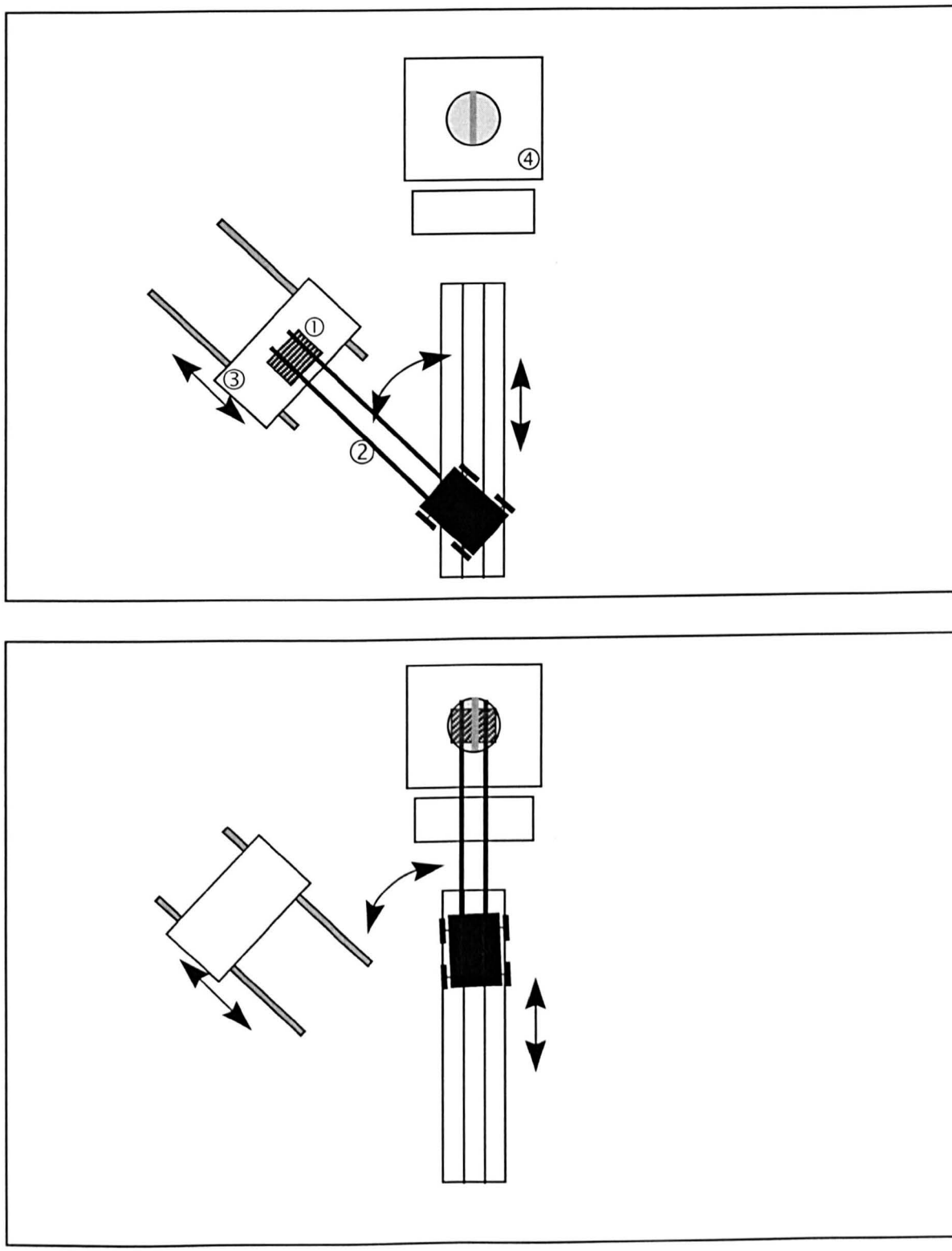

Figure 3.8a,b Schematic top view of the PSC-machine in Sheffield: a)specimen is heated in pre-heat furnace, b) specimen transported into deformation furnace

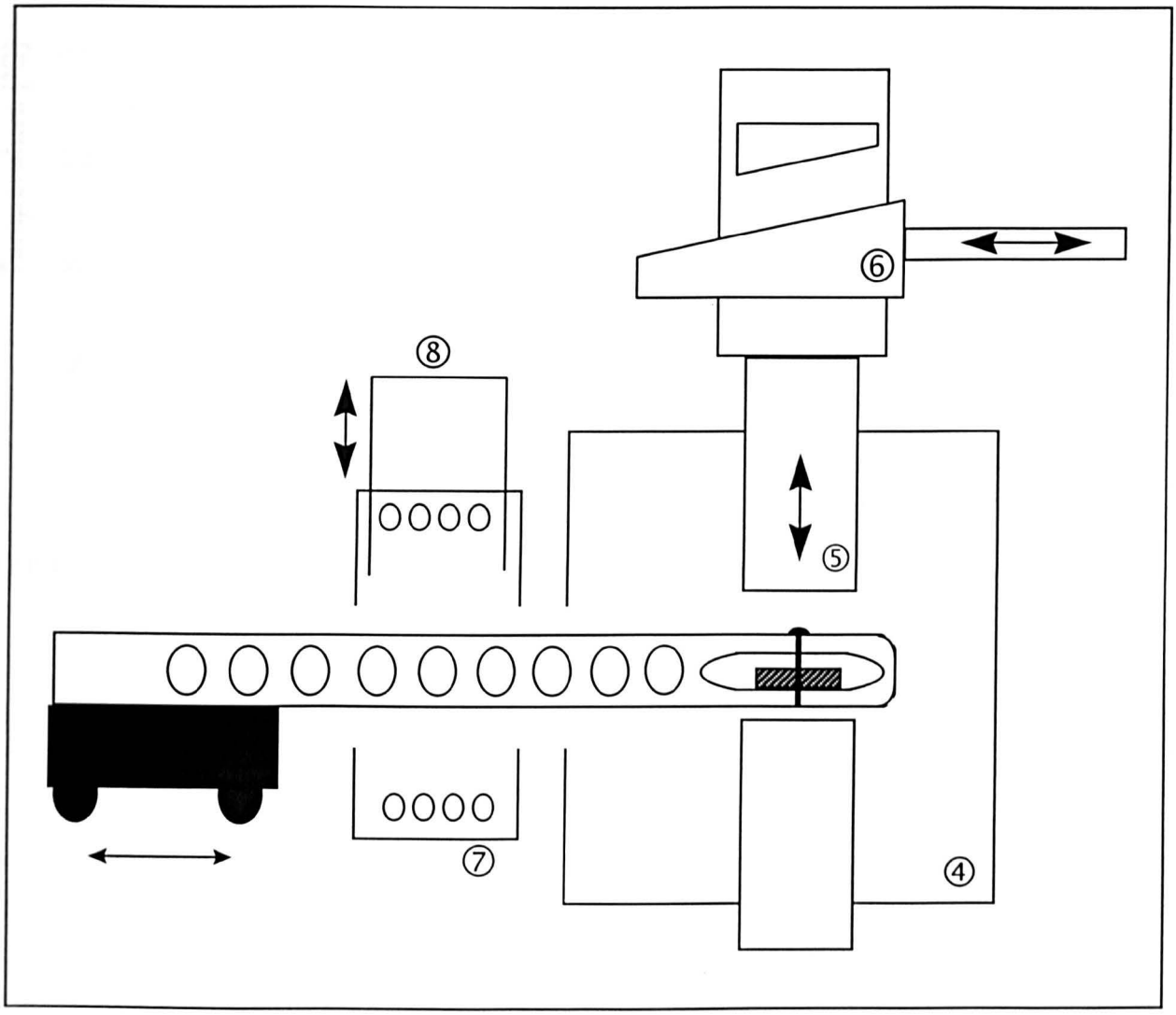

Figure 3.8c Schematic side view of the PSC-machine in Sheffield: Specimen just before being deformed.

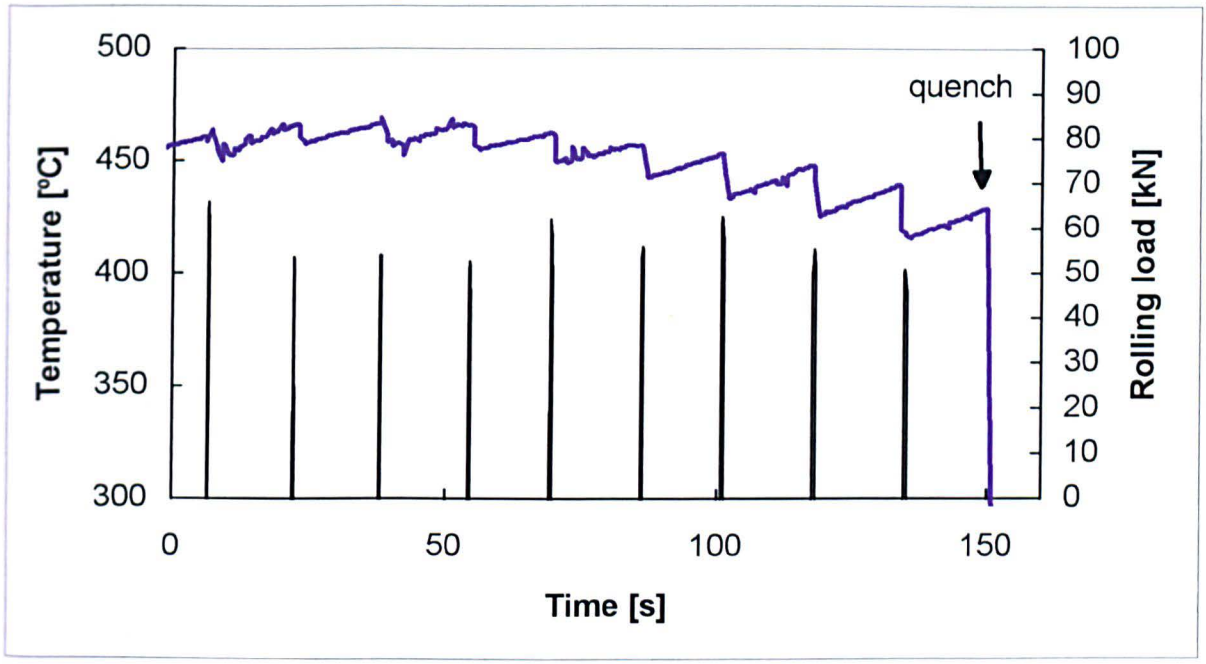

Figure 4.1a Temperature and load profile of a 9 pass experiment from series 1

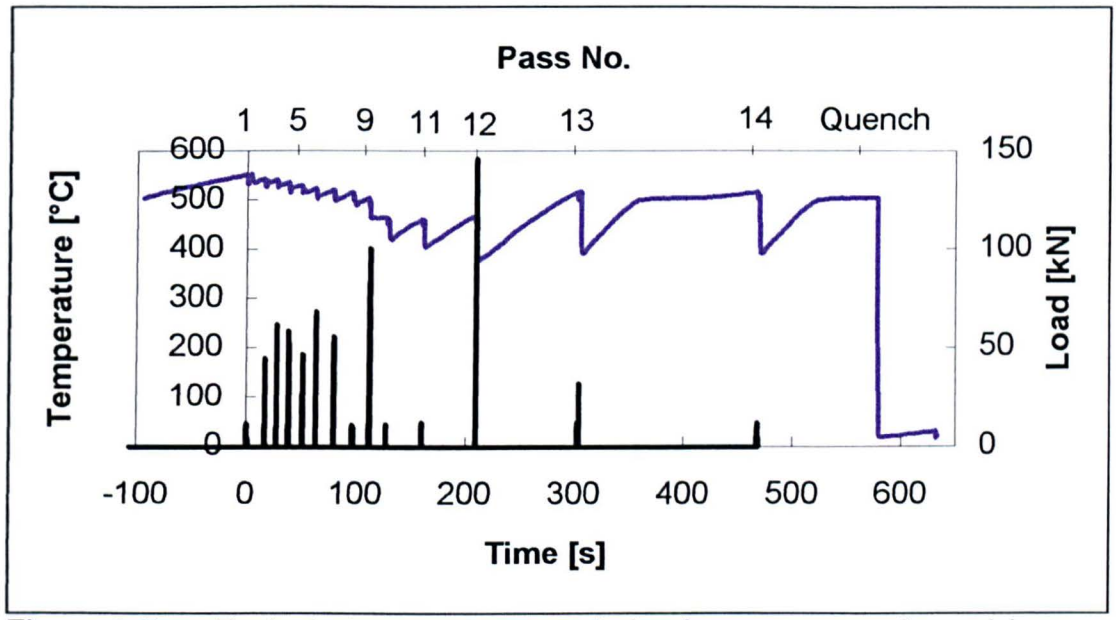

Figure 4.1b Typical temperature and load response of a 14 pass experiment from series 2a

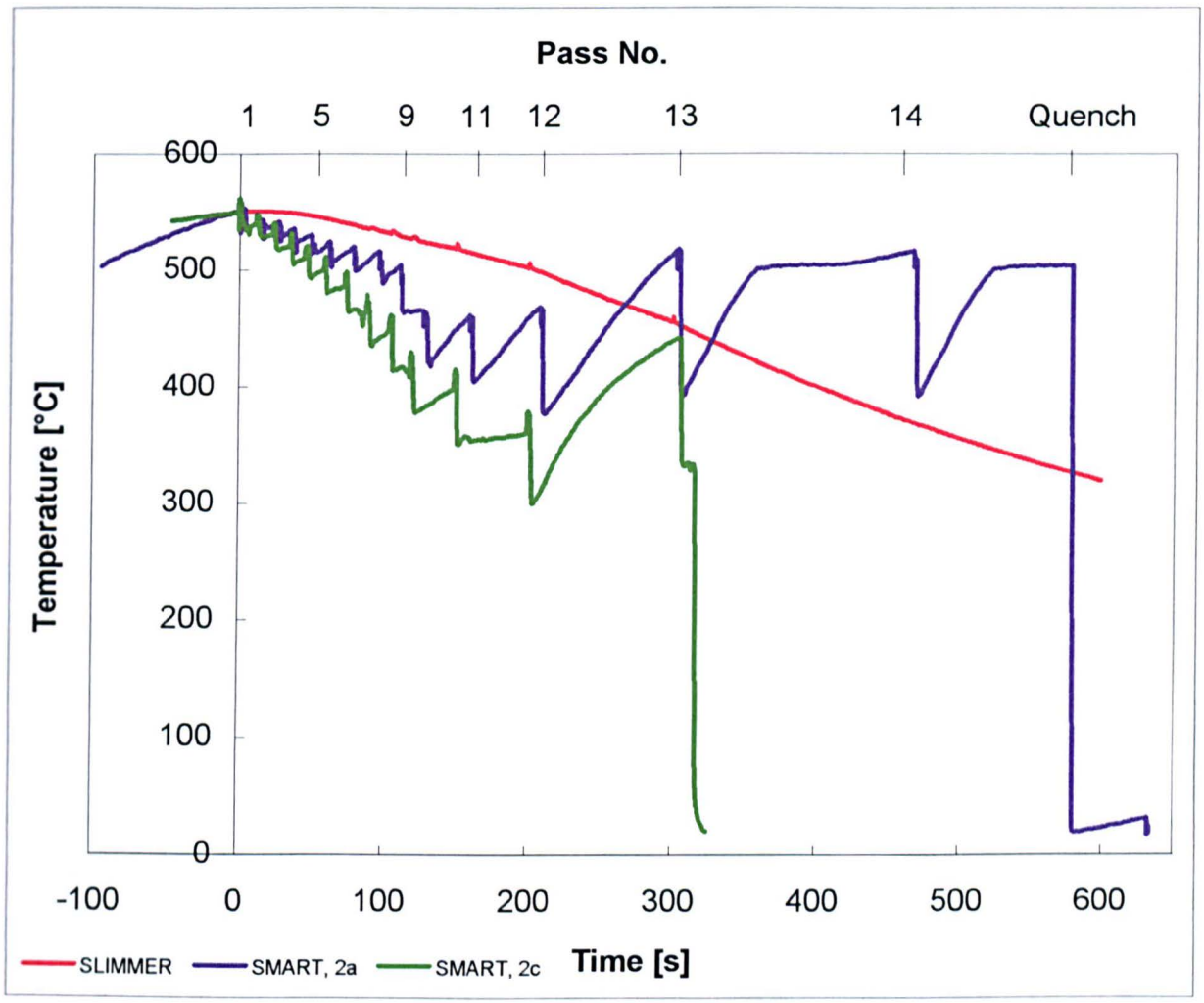

Figure 4.2 Temperature profiles of the SLIMMER simulation, series 2a and series 2c

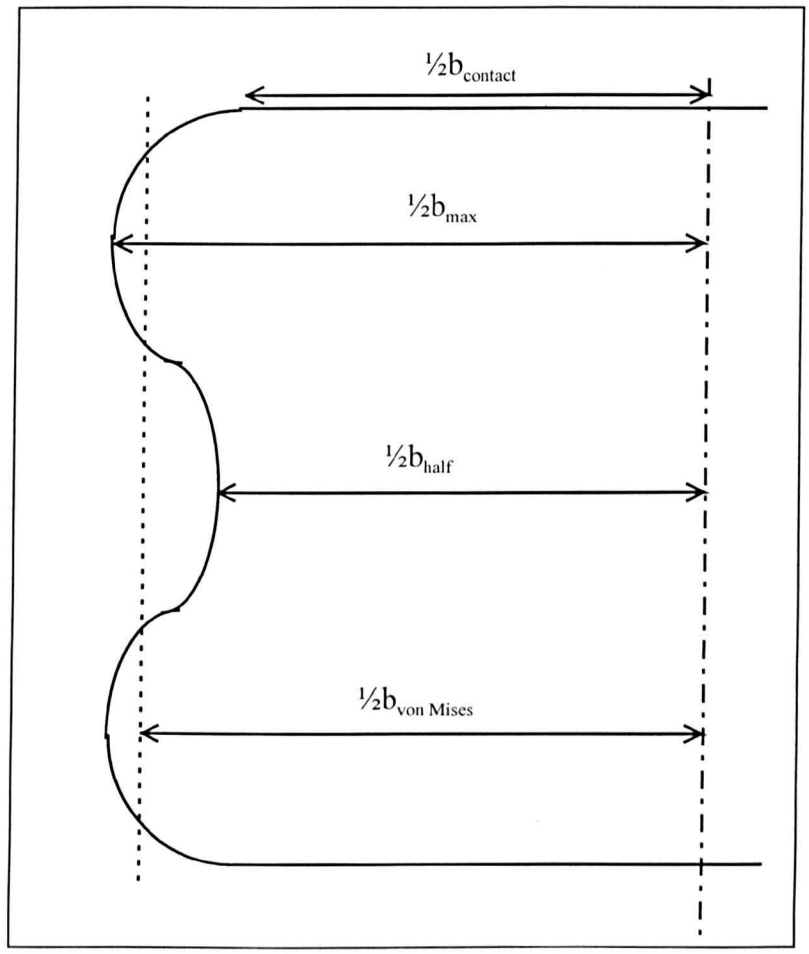

Figure 4.3 Illustration of the four values for the breadth of a sample

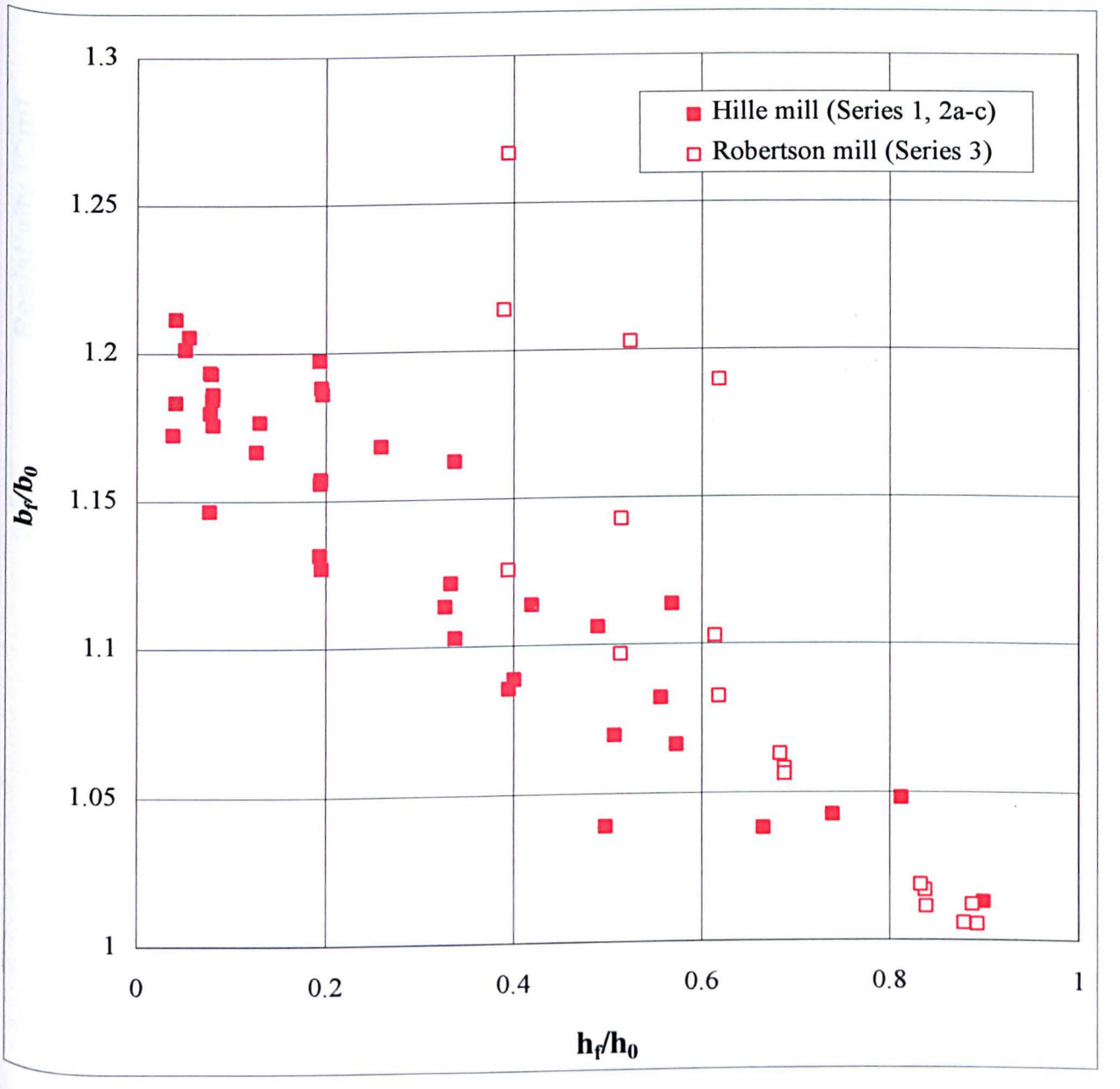

Figure 4.4 Scaled width against scaled heights for all rolling experiments

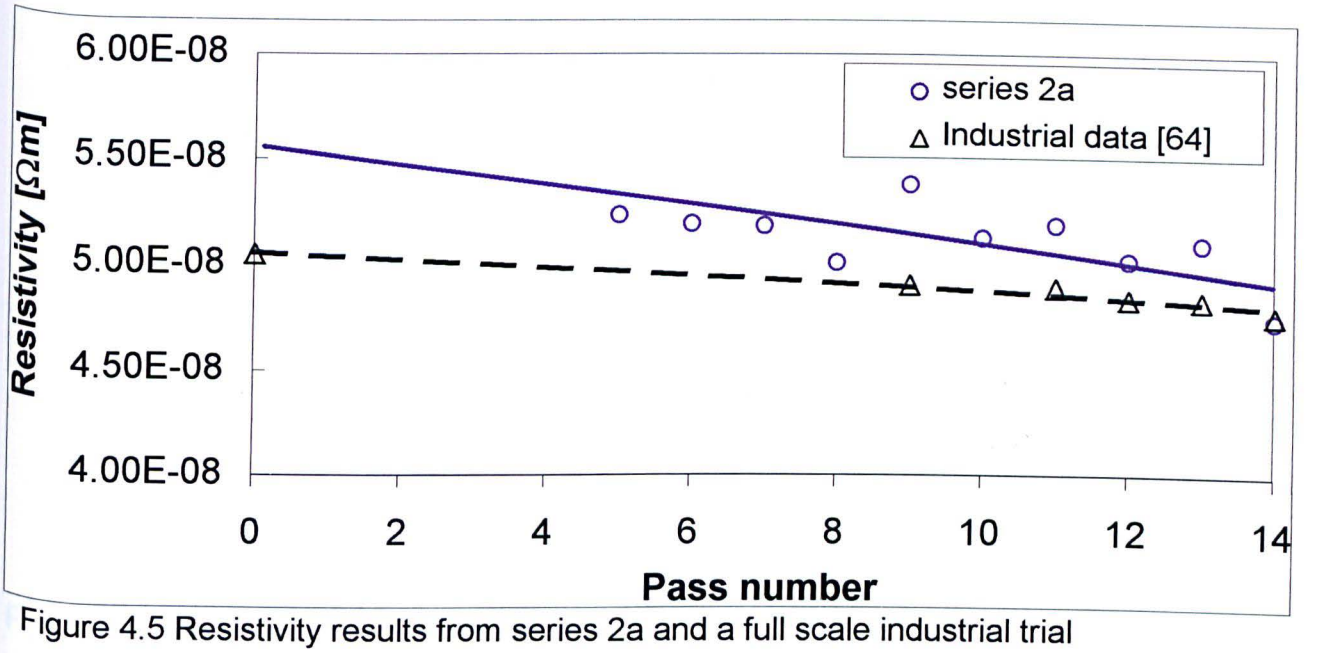

Figure 4.5 Resistivity results from series 2a and a full scale industrial trial

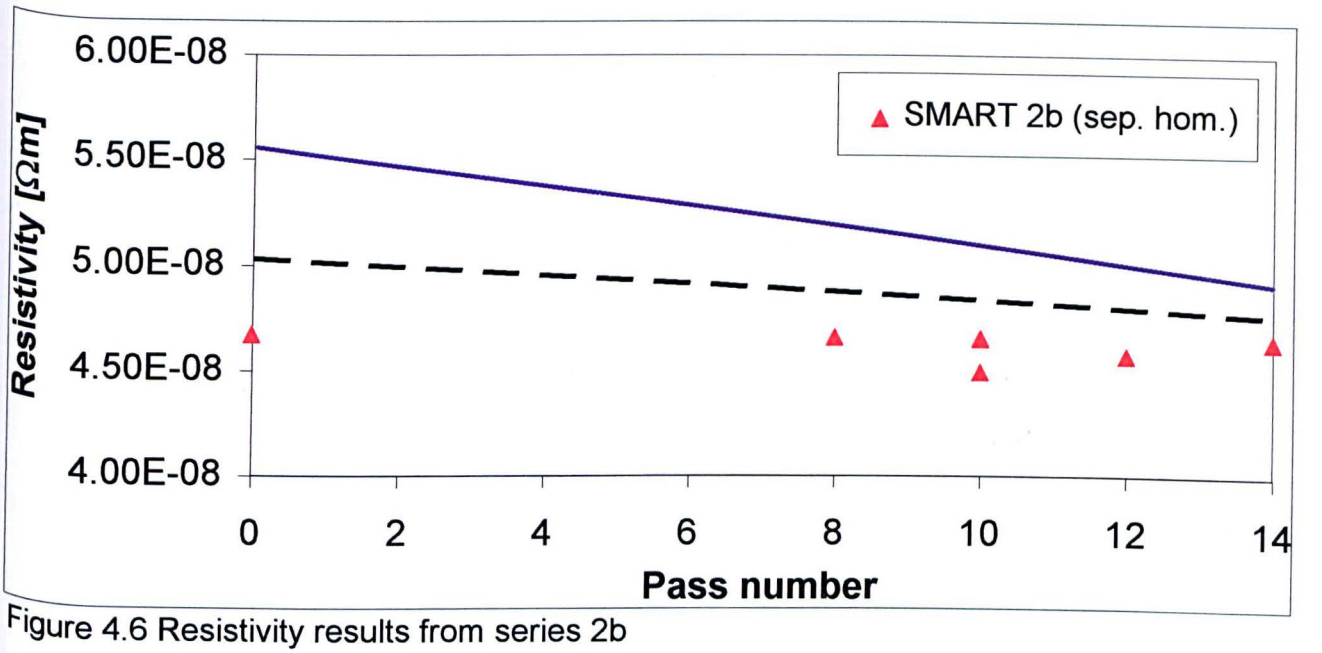

Figure 4.6 Resistivity results from series 2b

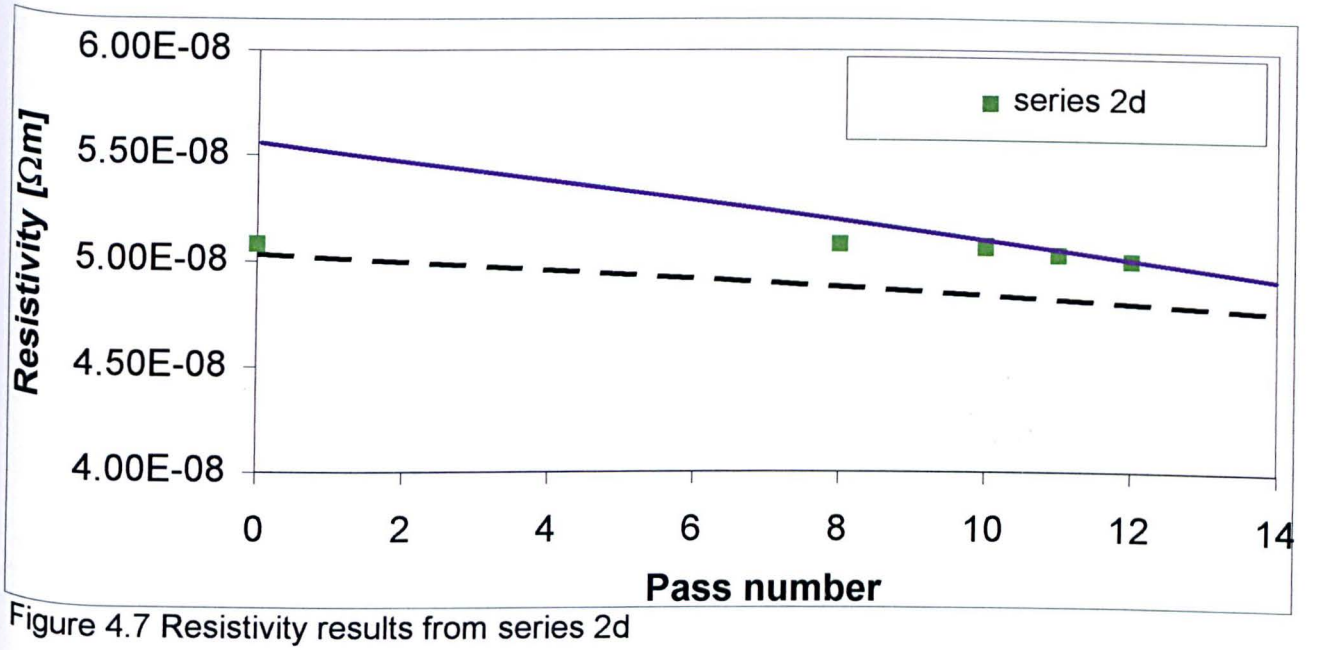

Figure 4.7 Resistivity results from series 2d

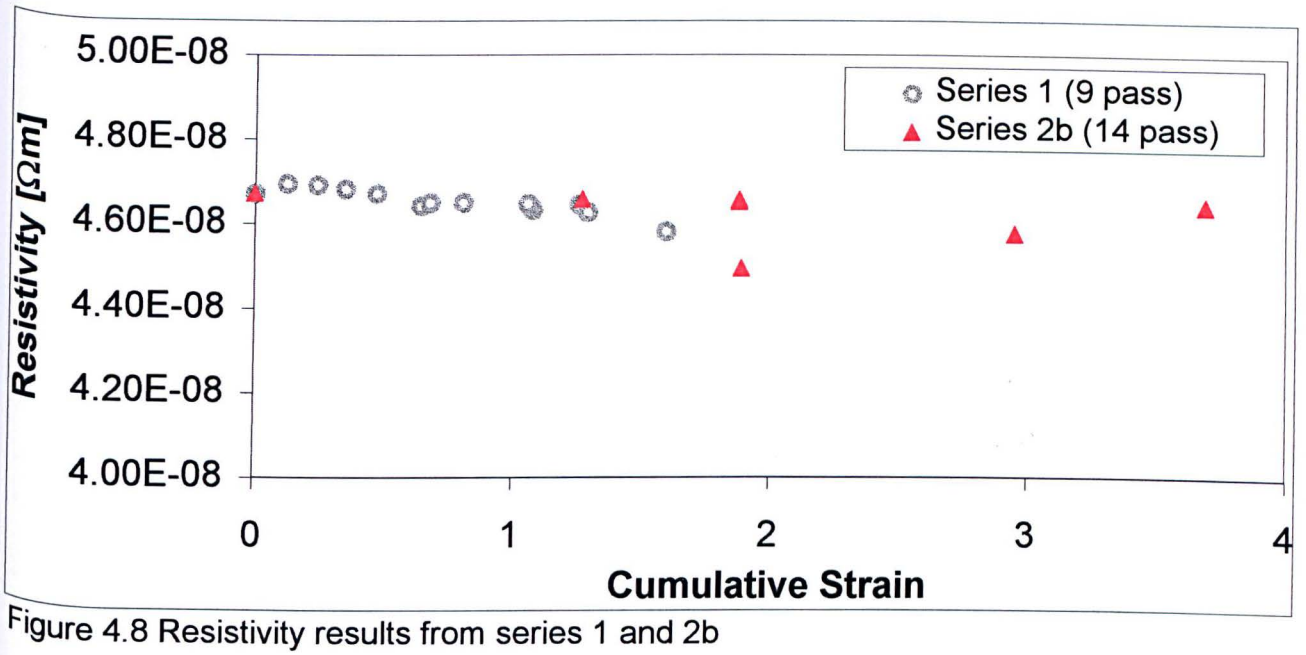

Figure 4.8 Resistivity results from series 1 and 2b

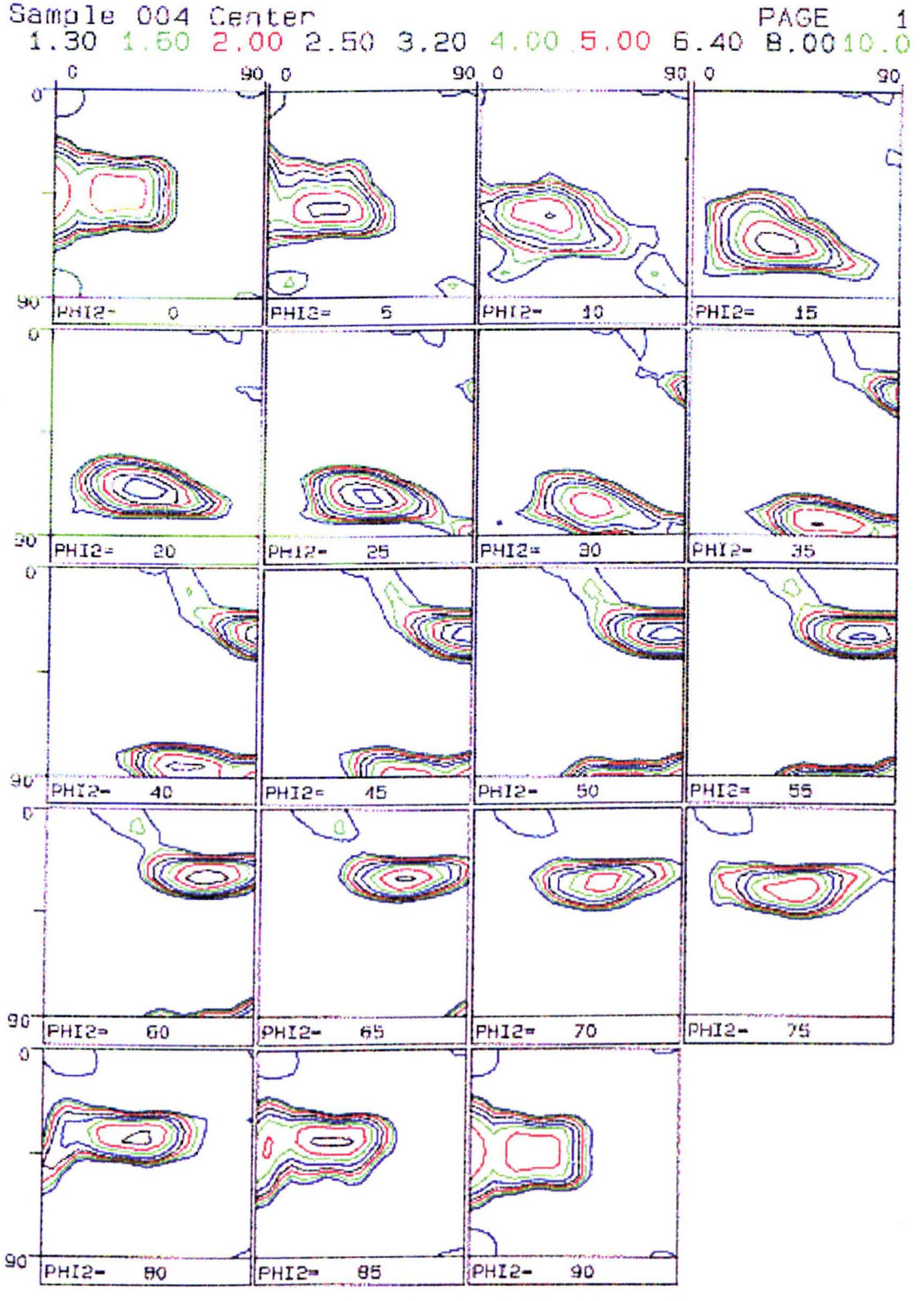

Figure 4.9 ODF of a specimen from series 1 after 9 passes

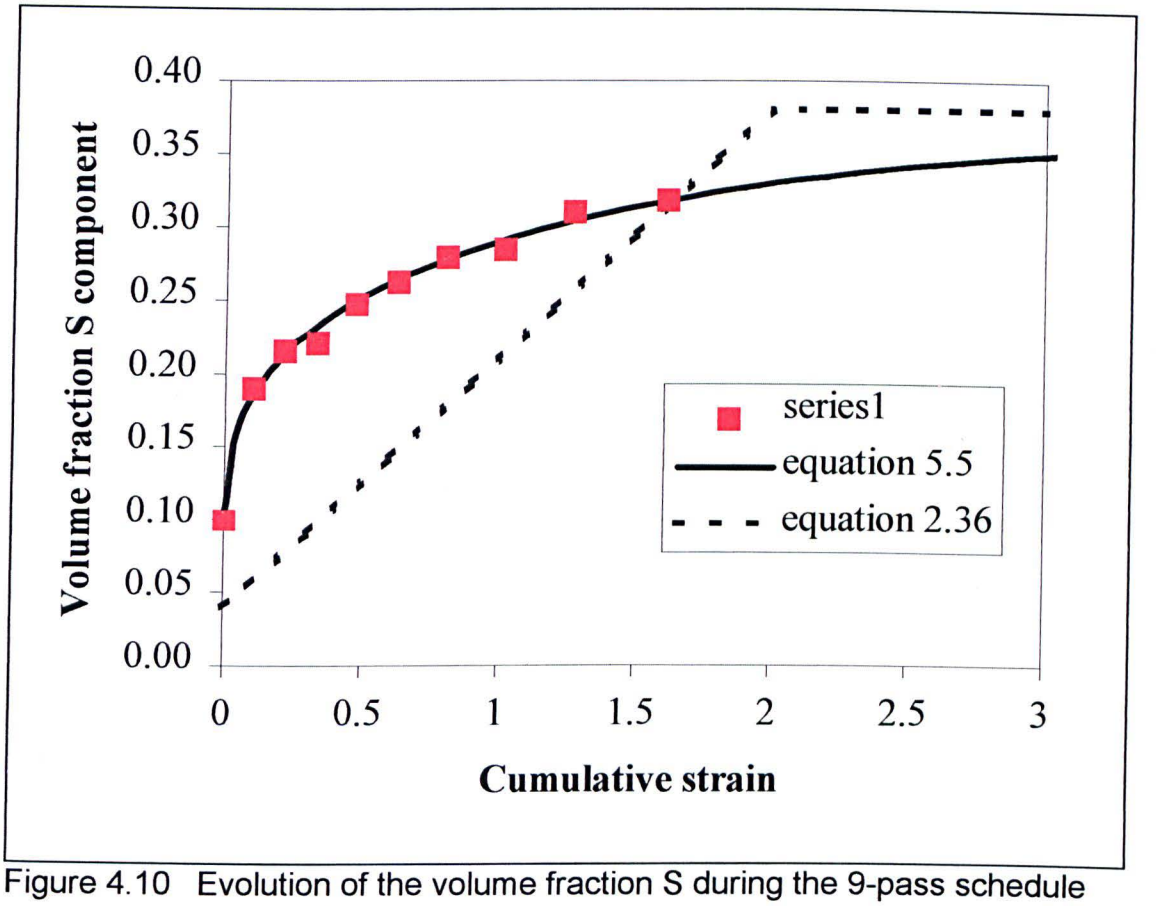

Figure 4.10 Evolution of the volume fraction S during the 9-pass schedule (series 1)

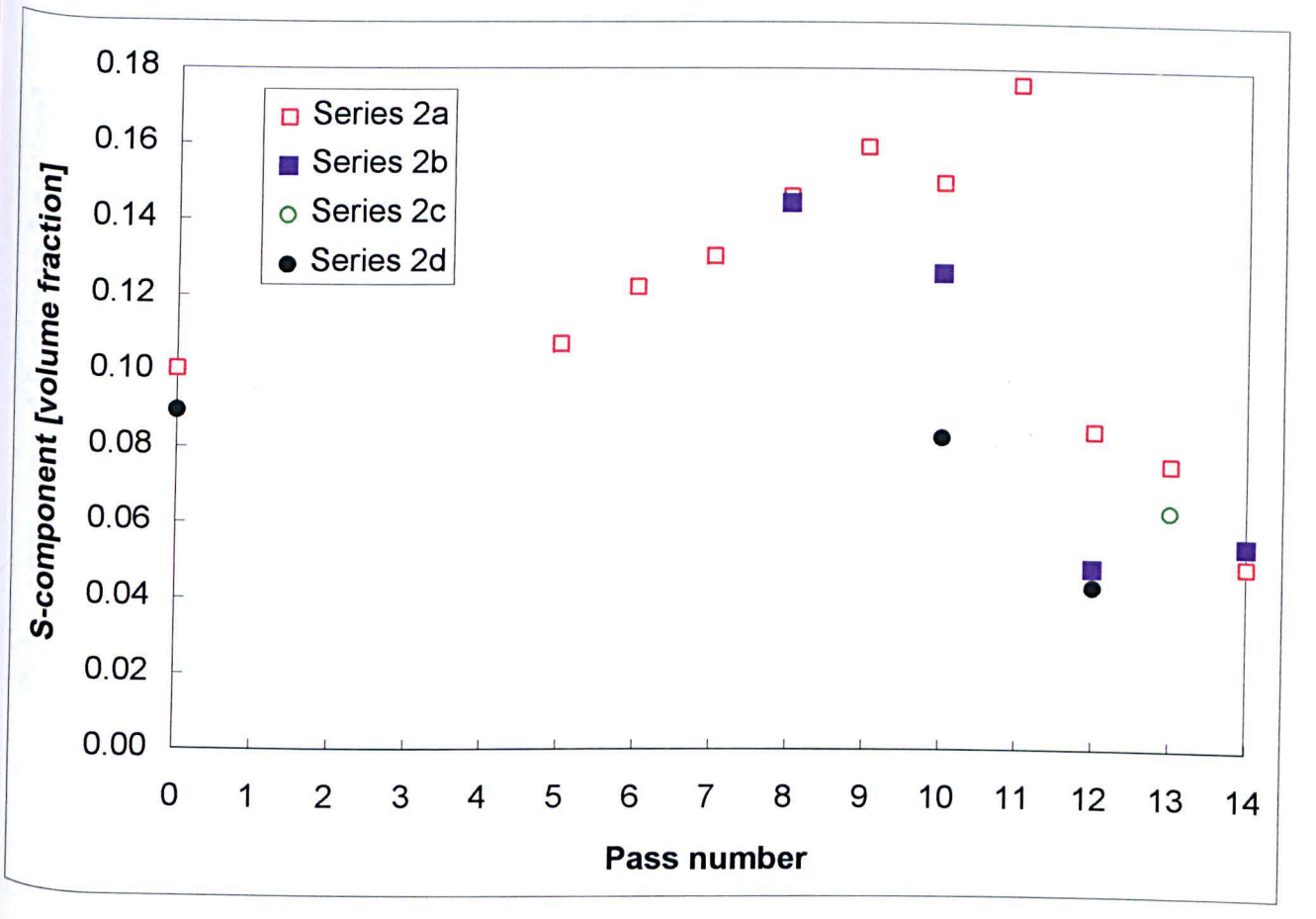

Figure 4.11 Evolution of the S-component during the 14 pass schedule

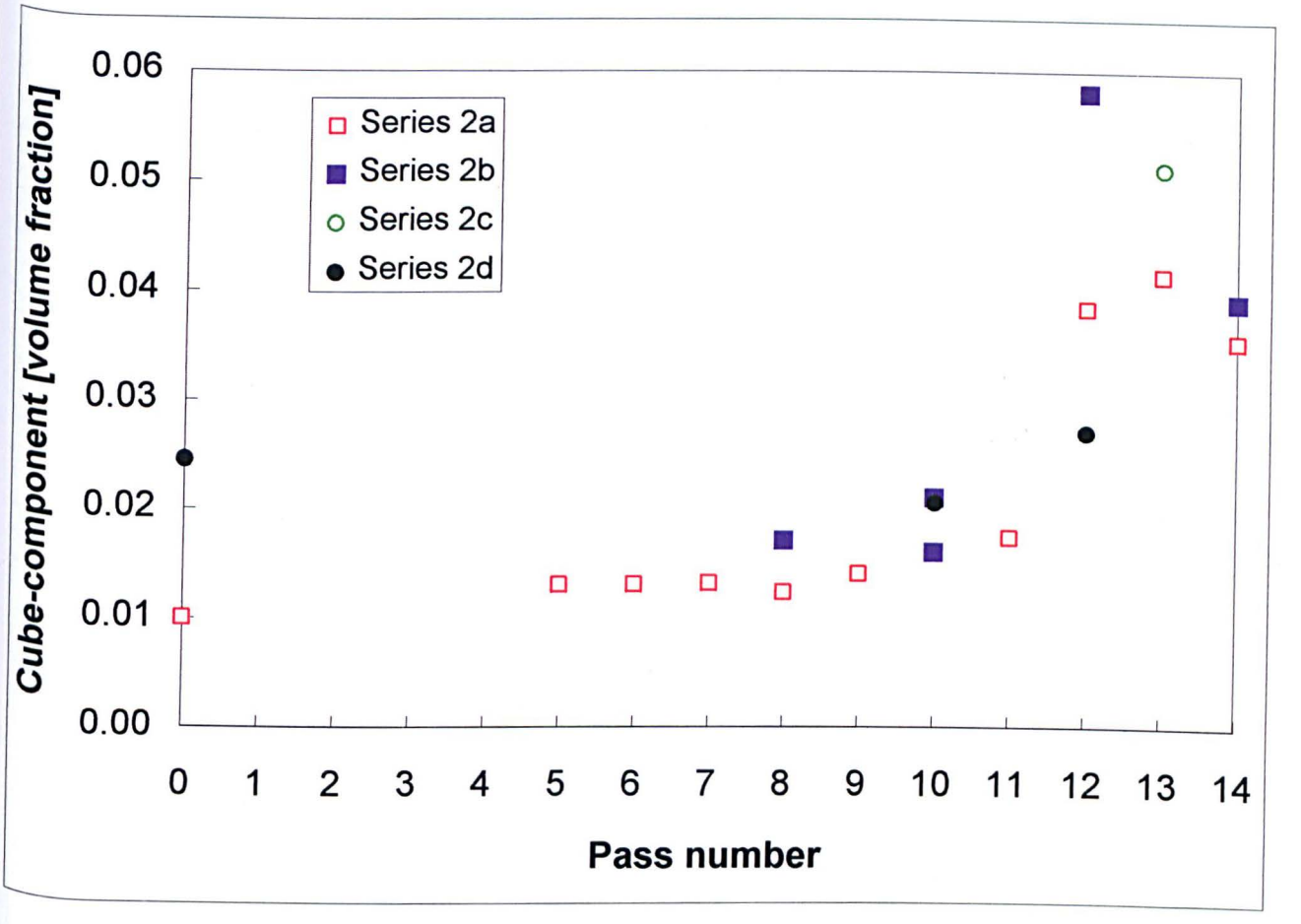

Figure 4.12 Evolution of the Cube-component during the 14 pass experiments

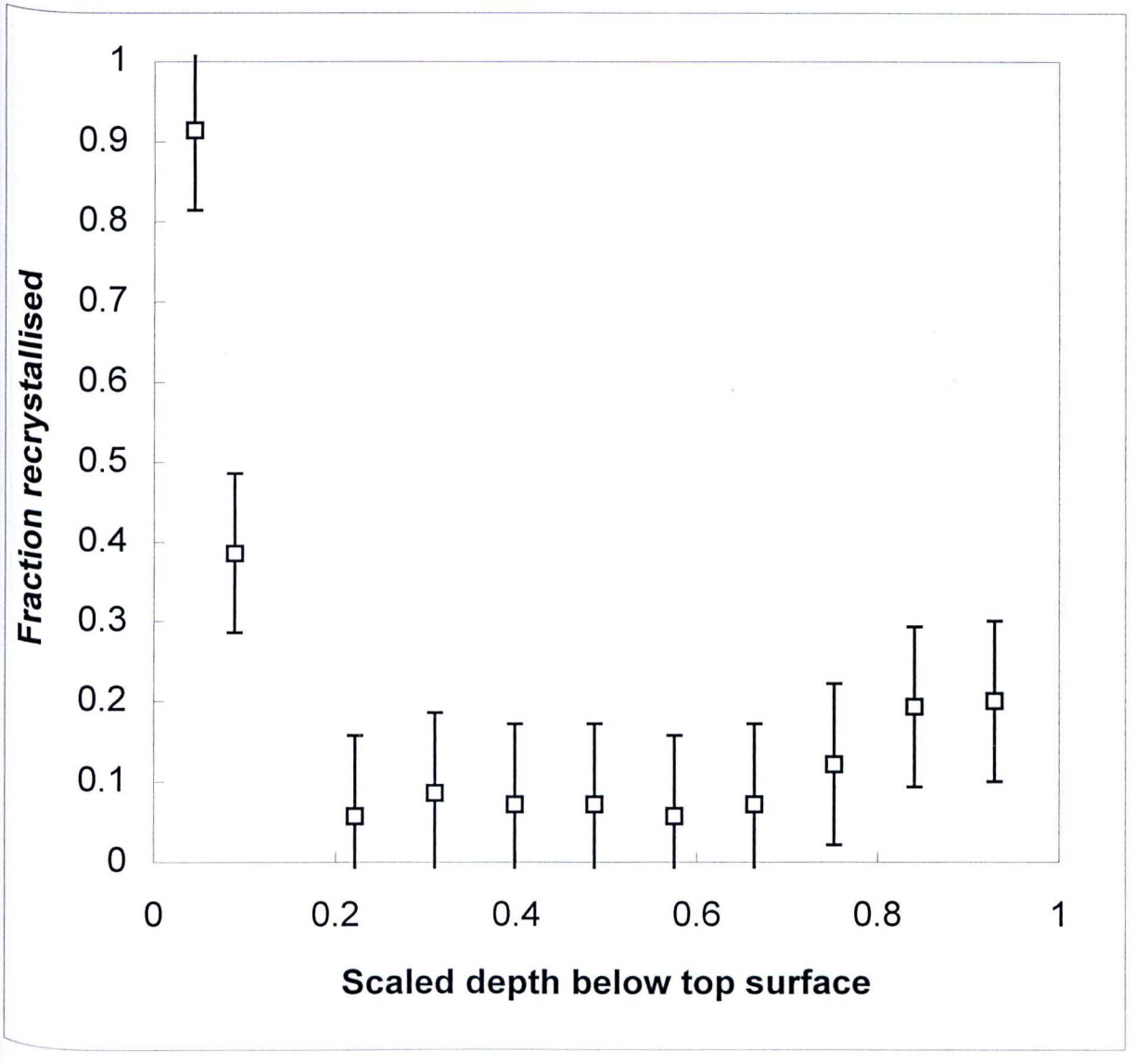

Figure 4.13 Recrystallised fraction after 8 passes (series 2a) as function of the depth below the top surface

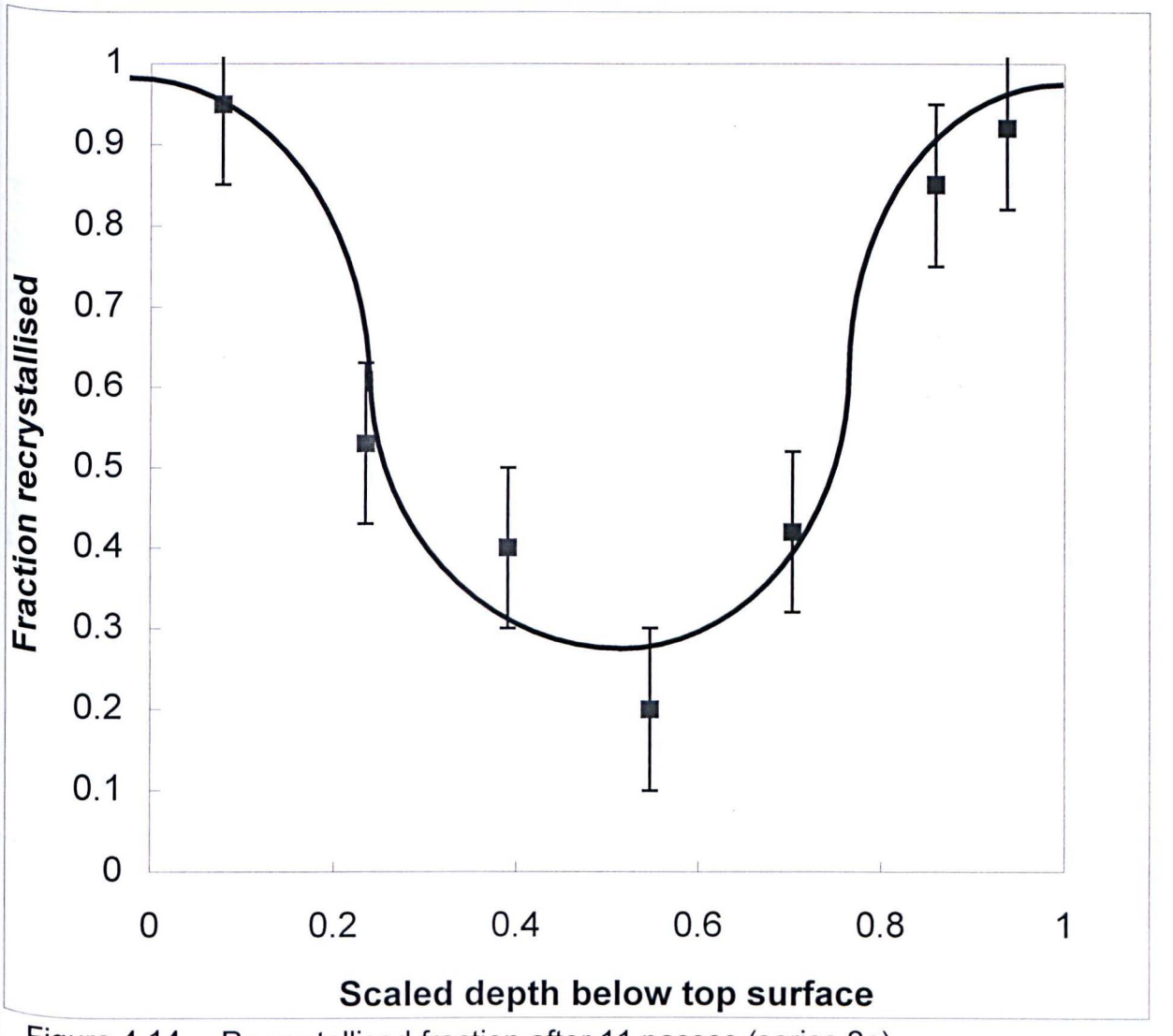

Figure 4.14 Recrystallised fraction after 11 passes (series 2a) as function of the depth below the top surface

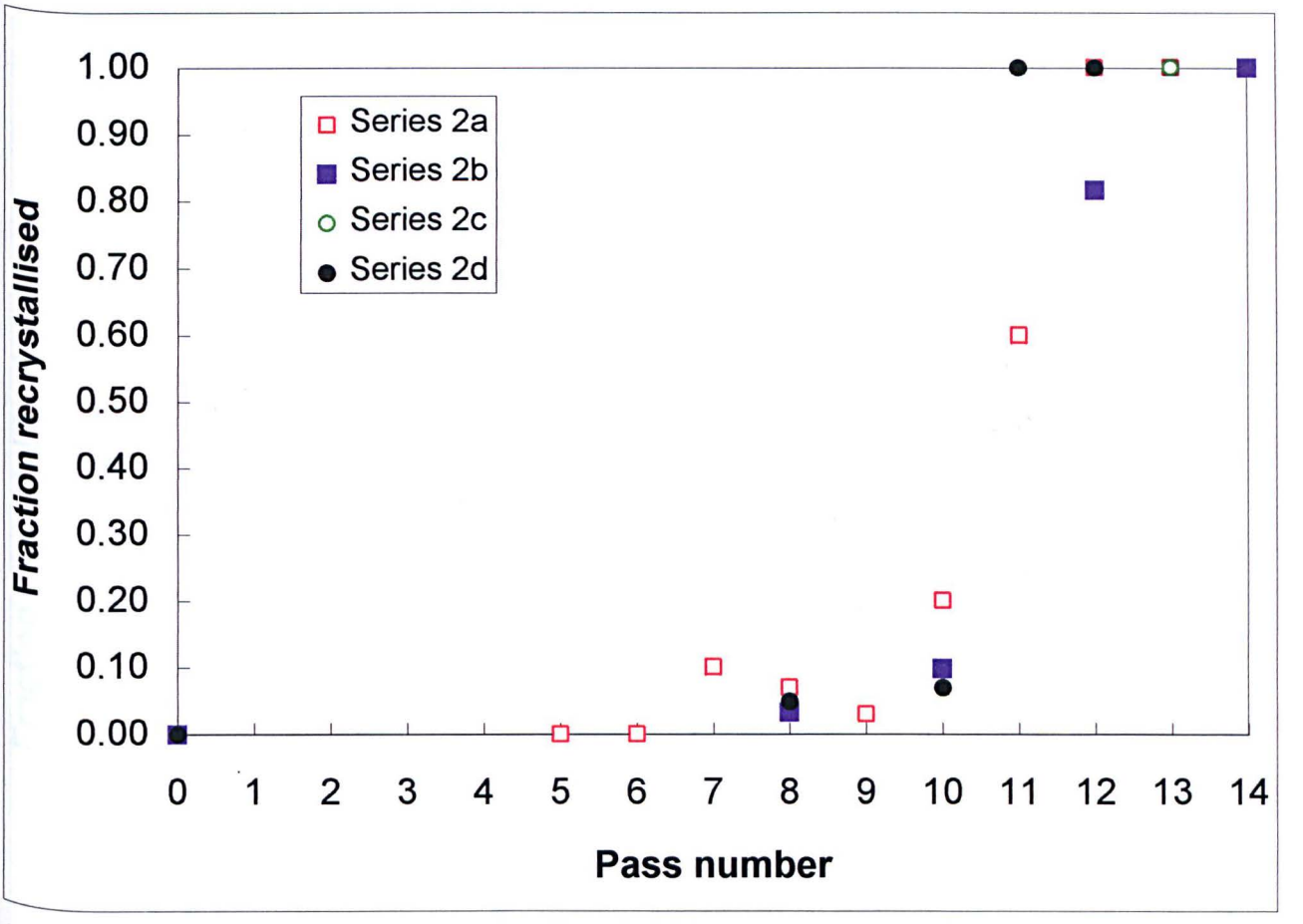

Figure 4.15 Fraction recrystallised as function of pass number for series 2a,b,c,d

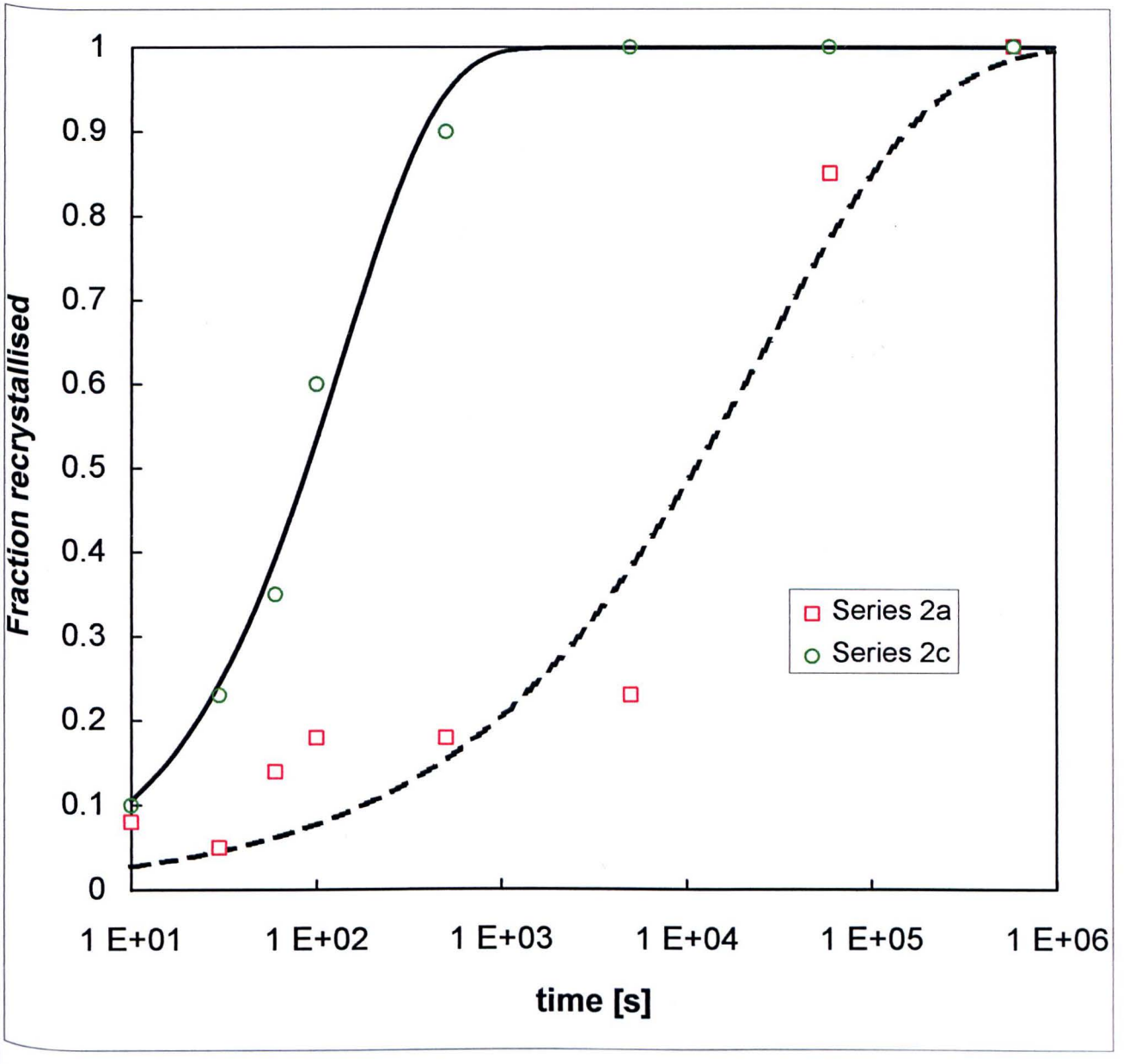

Figure 4.16 Avrami curves from 13 pass material of series 2a and 2c, annealed at 330 °C

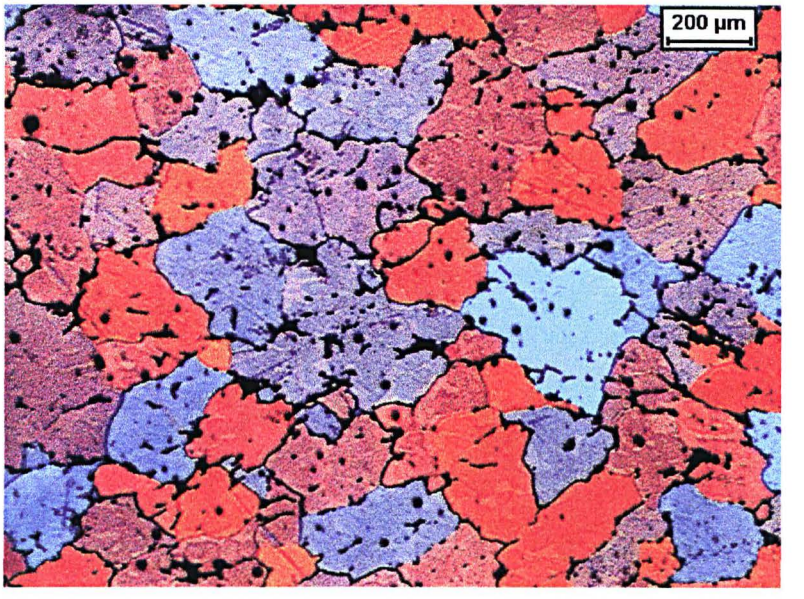

Figure 4.17a Microstructure after homogenisation

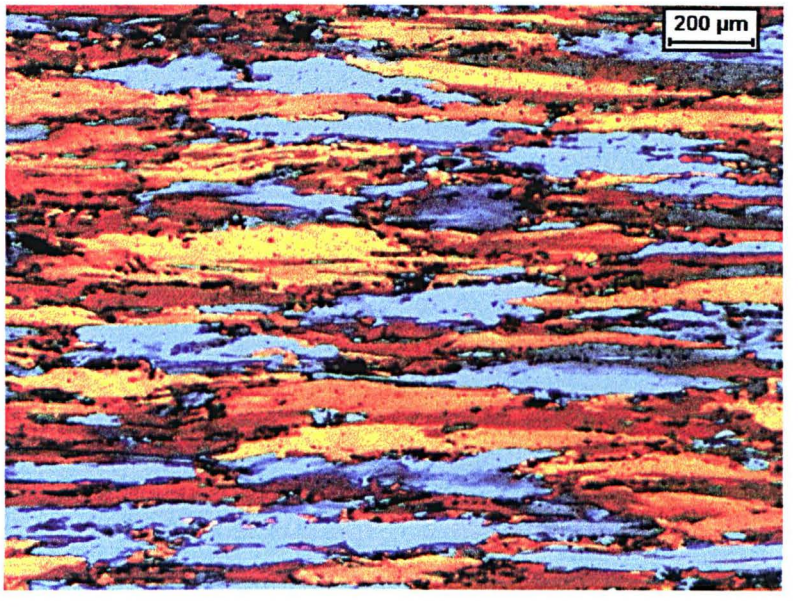

Figure 4.17b Microstructure after 9 passes of series 1

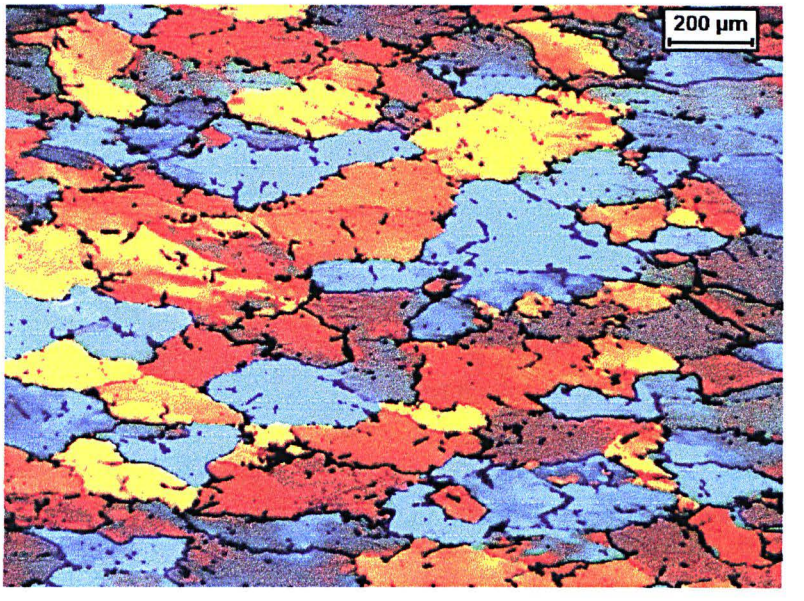

Figure 4.18a Microstructure after 5 passes of series 2a

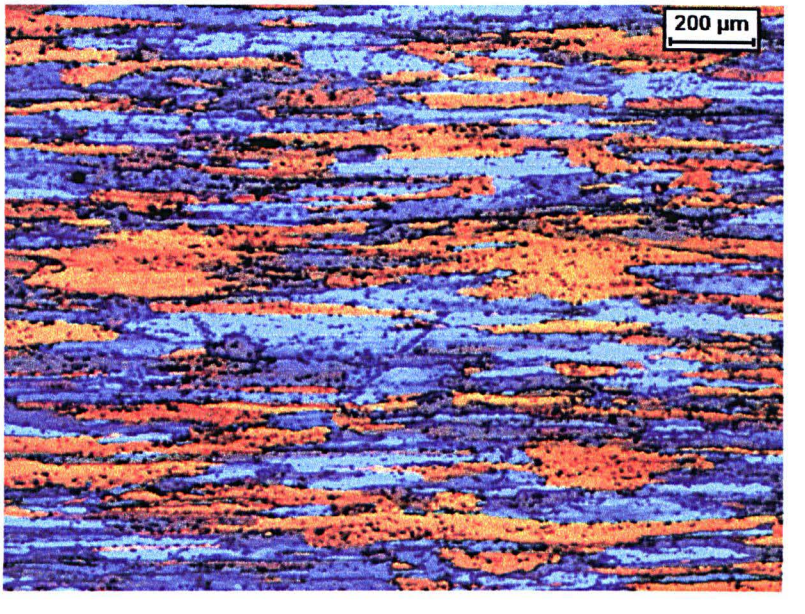

Figure 4.18b Microstructure after 10 passes of series 2a

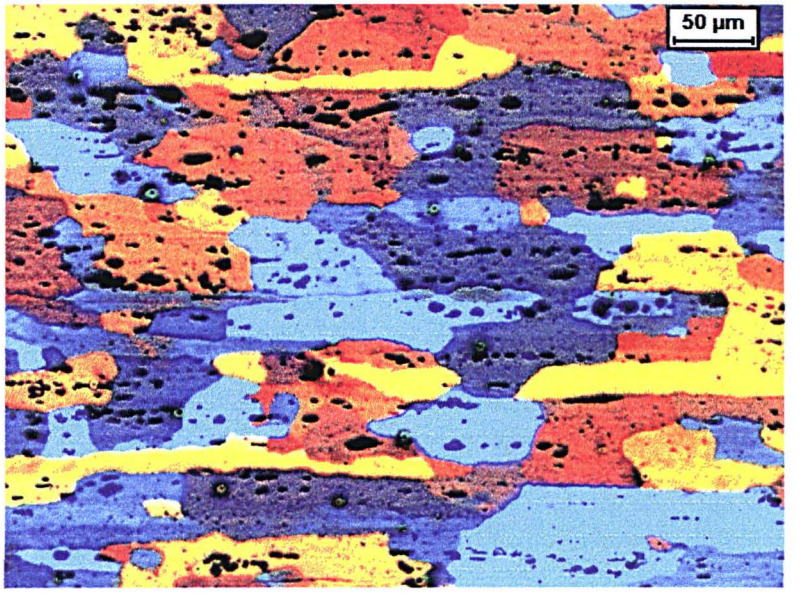

Figure 4.18c Microstructure after 12 passes of series 2a

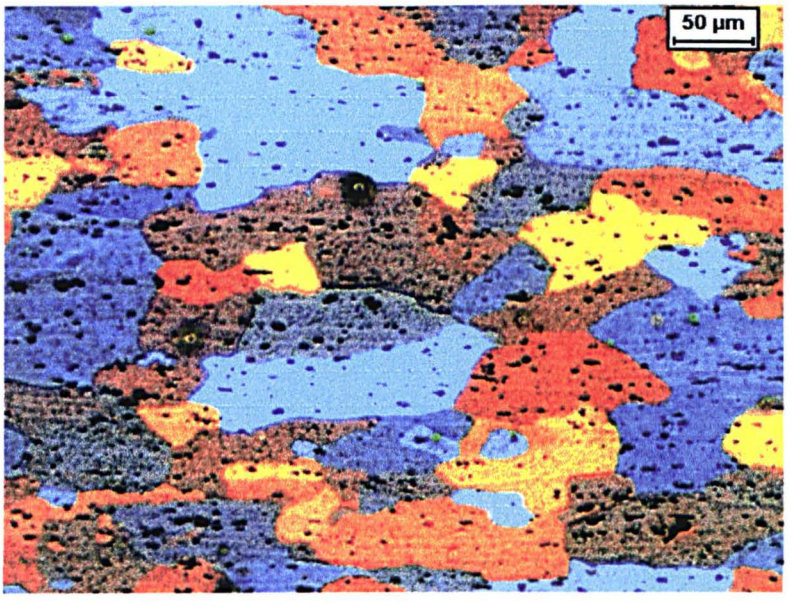

Figure 4.18d Microstructure after 14 passes of series 2a

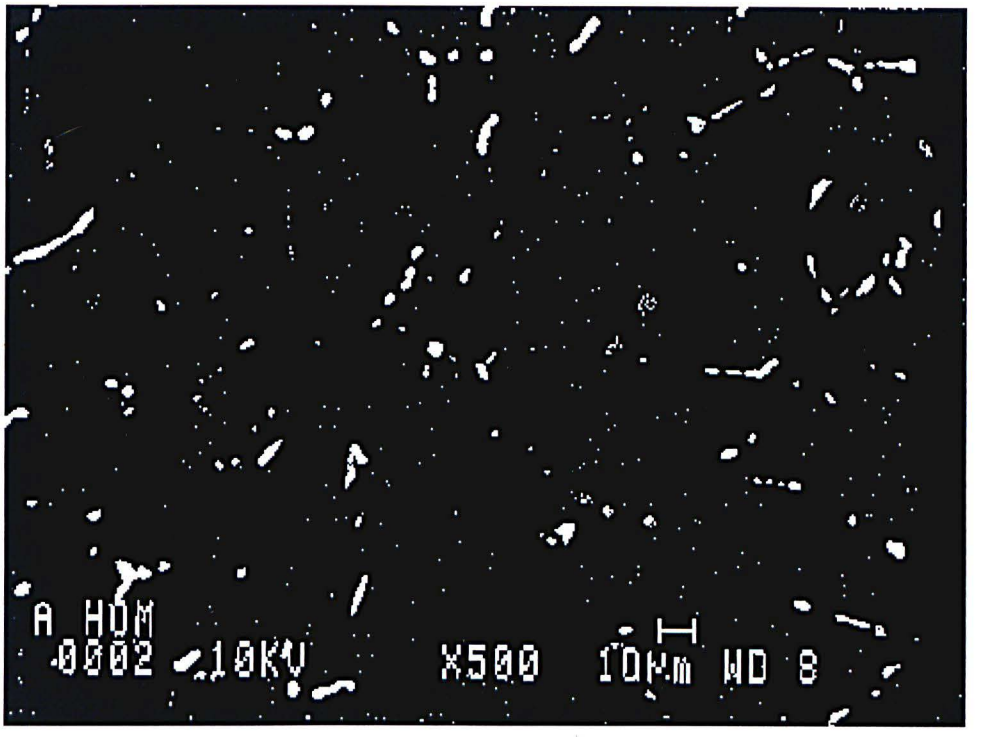

Figure 4.19a Constituent particles after homogenisation, material A (series 2a)

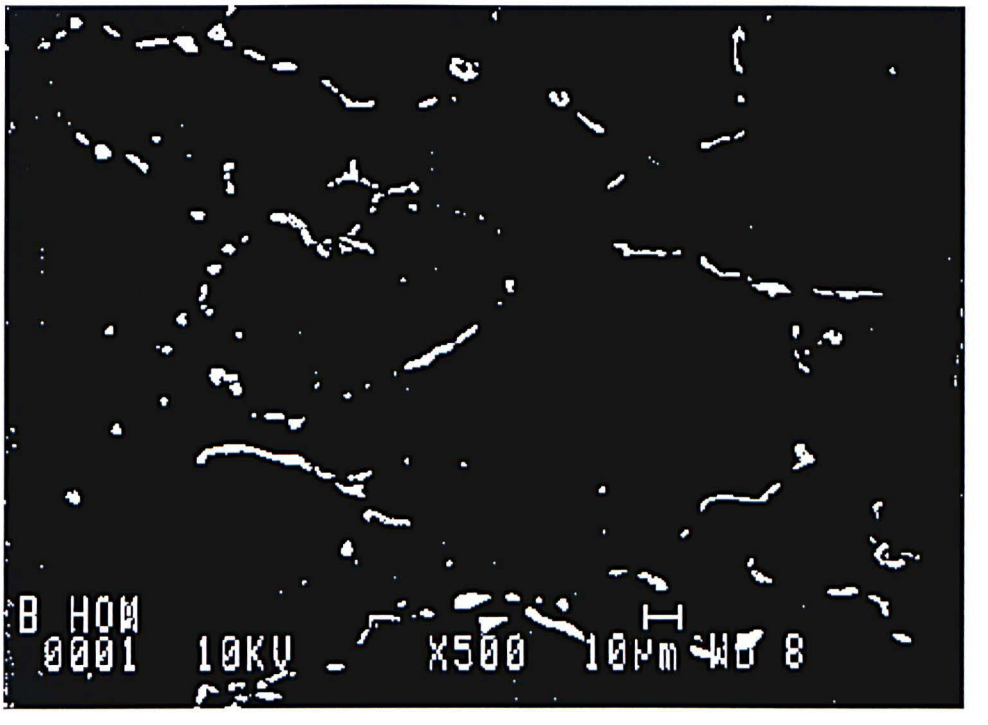

Figure 4.19b Constituent particles after homogenisation, material B (series 2d)

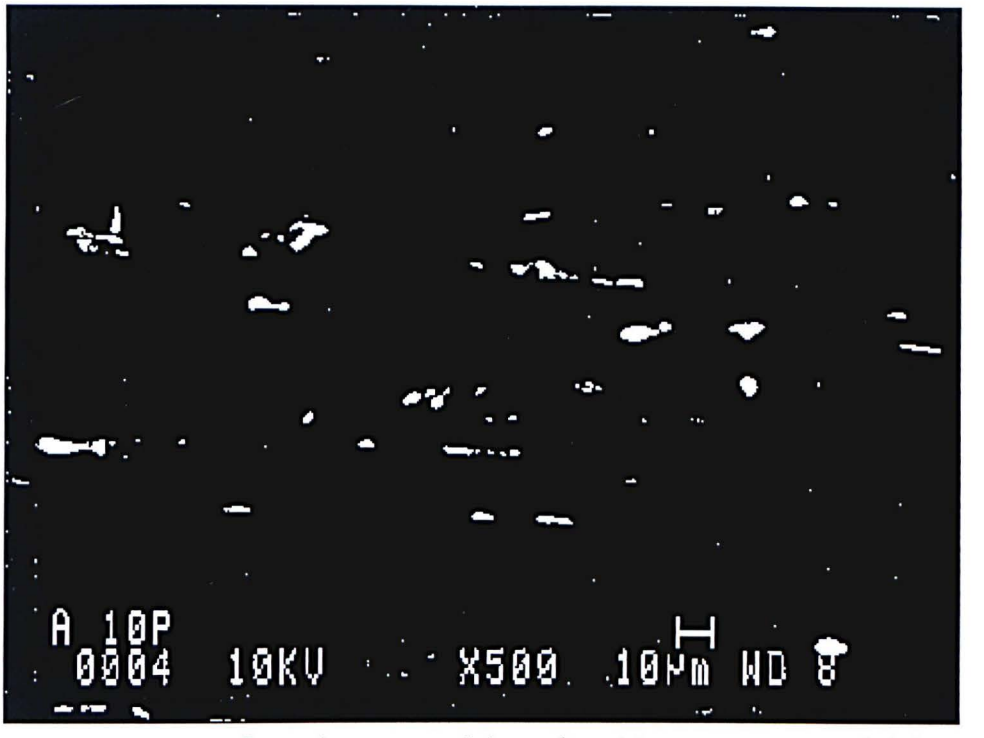

Figure 4.20a Constituent particles after 10 passes, material A (series 2a)

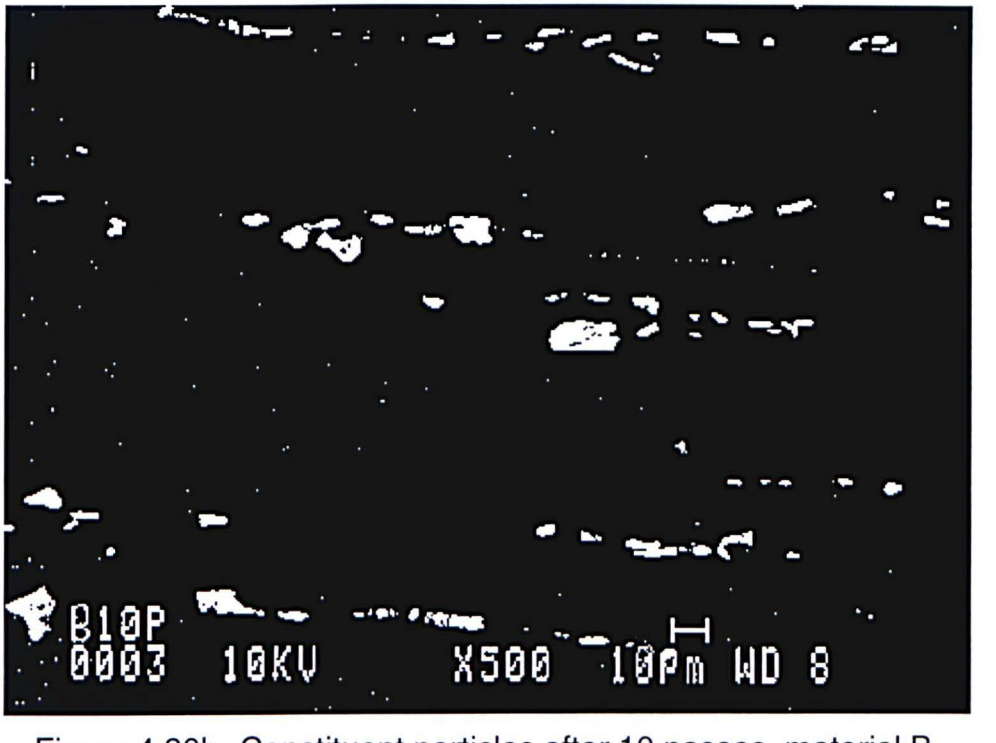

Figure 4.20b Constituent particles after 10 passes, material B (series 2d)

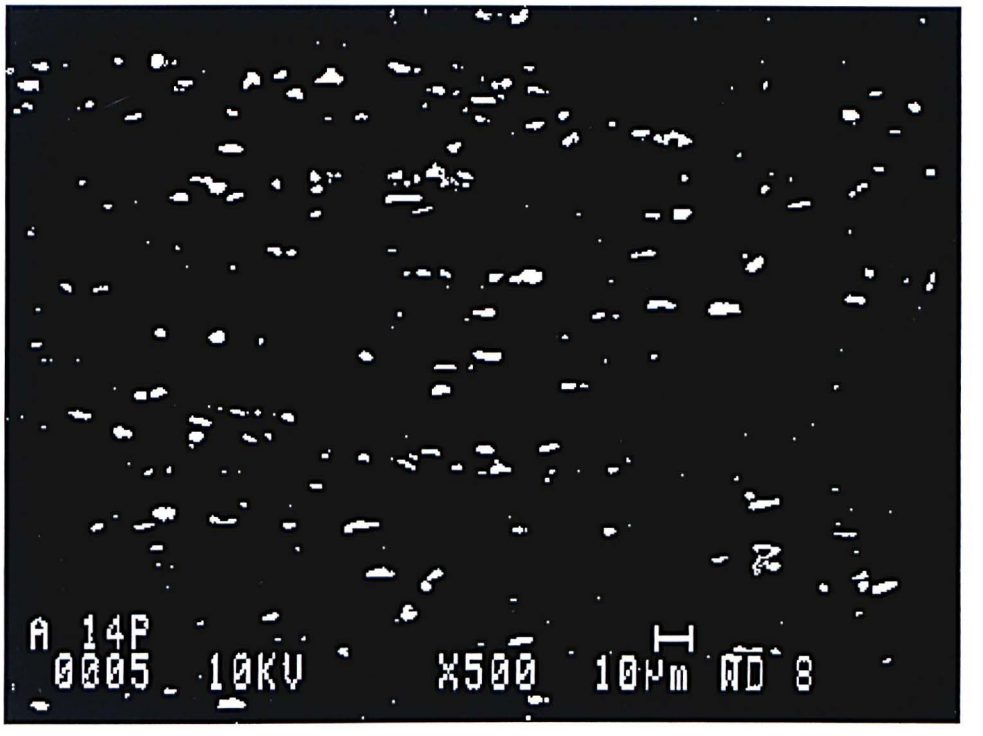

Figure 4.21a Constituent particles after 14passes, material A (series 2a)

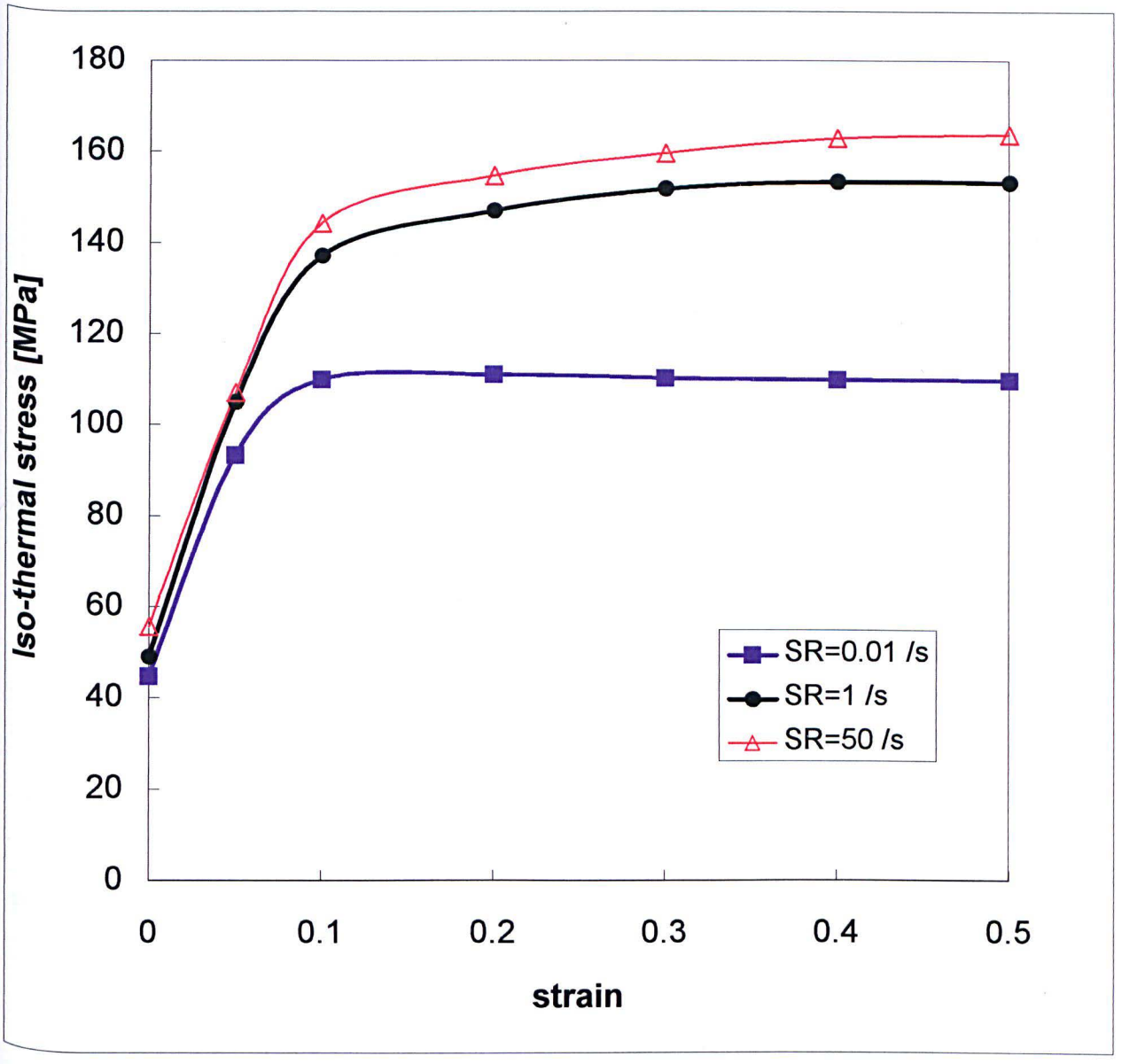

Figure 4.22 Iso-thermal stress-strain curves;
Tnom= 280 °C, three strain rates

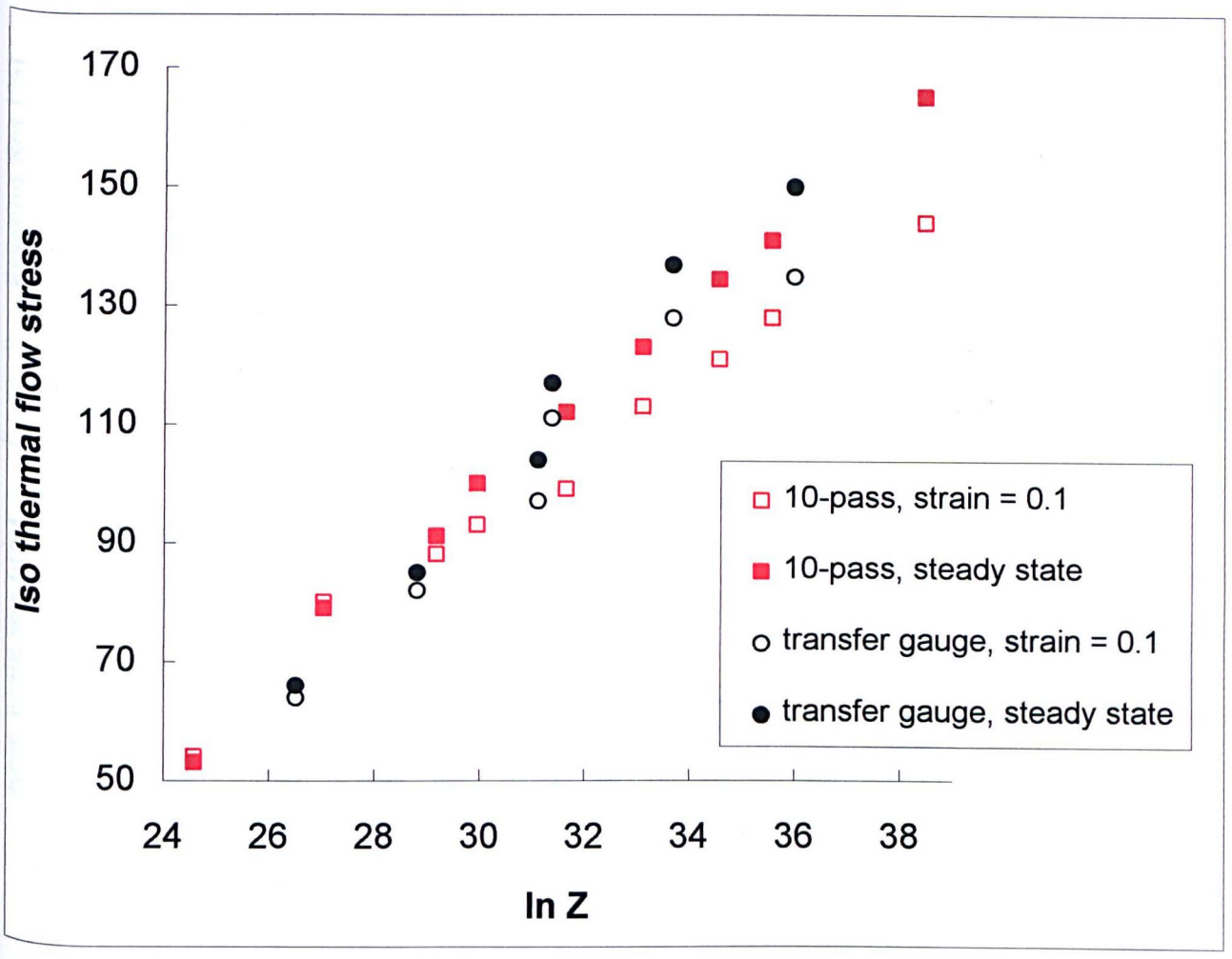

Figure 4.23 Isothermal flow stress data from PSC experiments

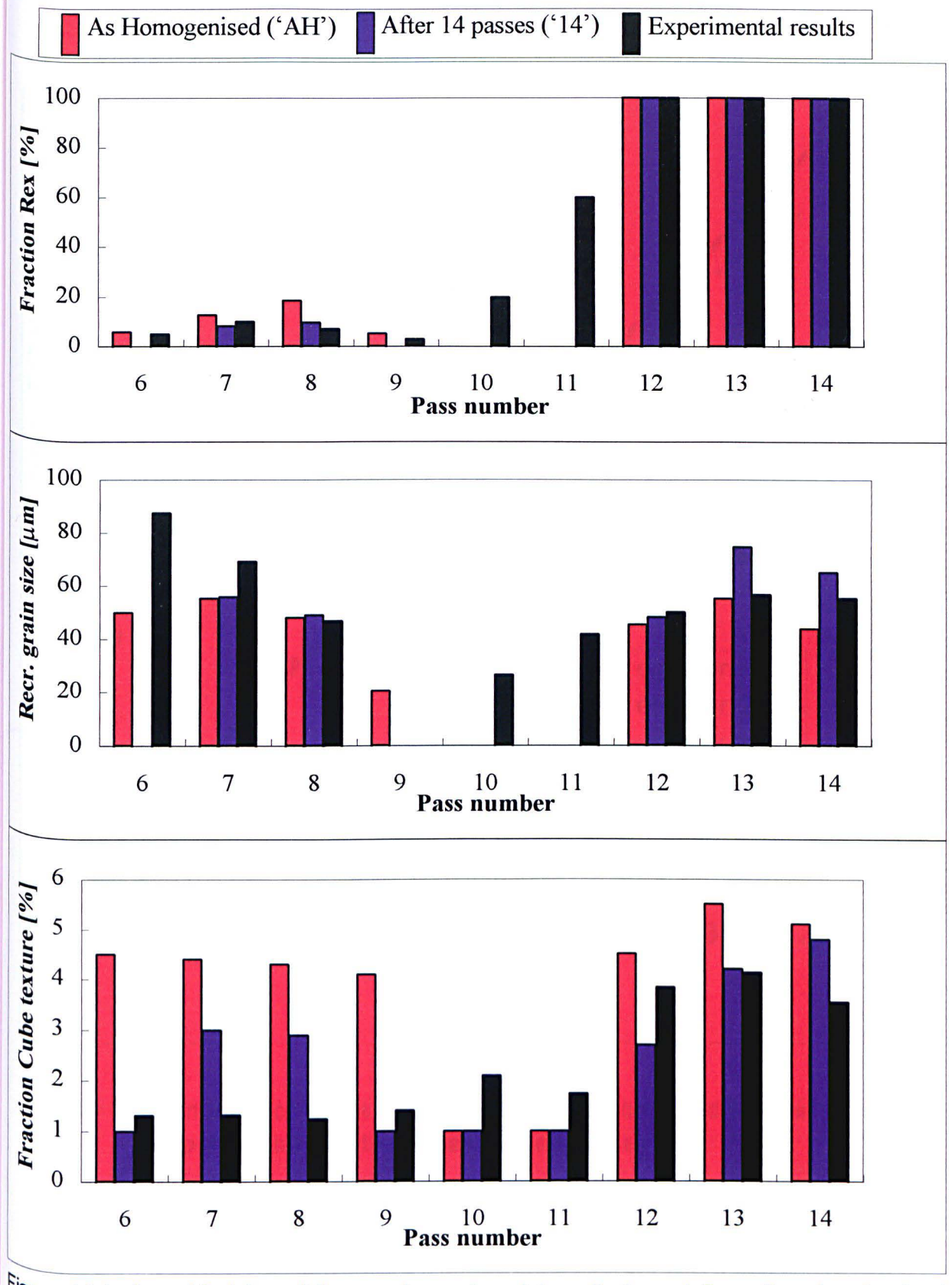

Figure 4.24 a,b,c Model predictions and experimental results. In each figure the microstructural predictions of the 'AH' and '14' simulations are compared with the experimental measurements. The red bars represent the particle distribution as measured on the as-homogenised material. The blue bars show the model prediction based on the distribution of the 14-pass material. The black bars represent the experimental values from SMART.

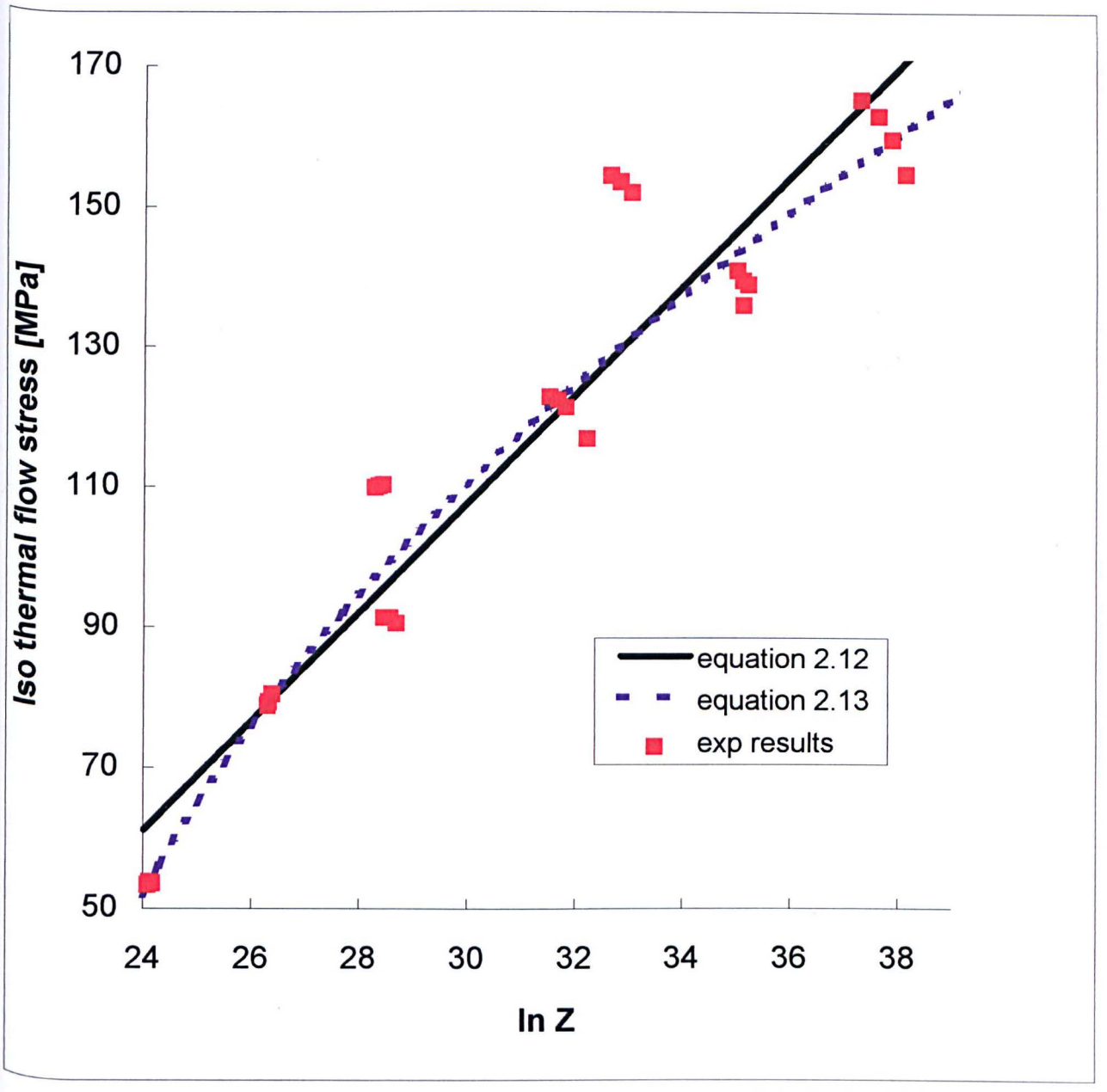

Figure 5.1 Performance of equation 2.12 and 2.13, compared with the experimental results (10-pass, steady state)

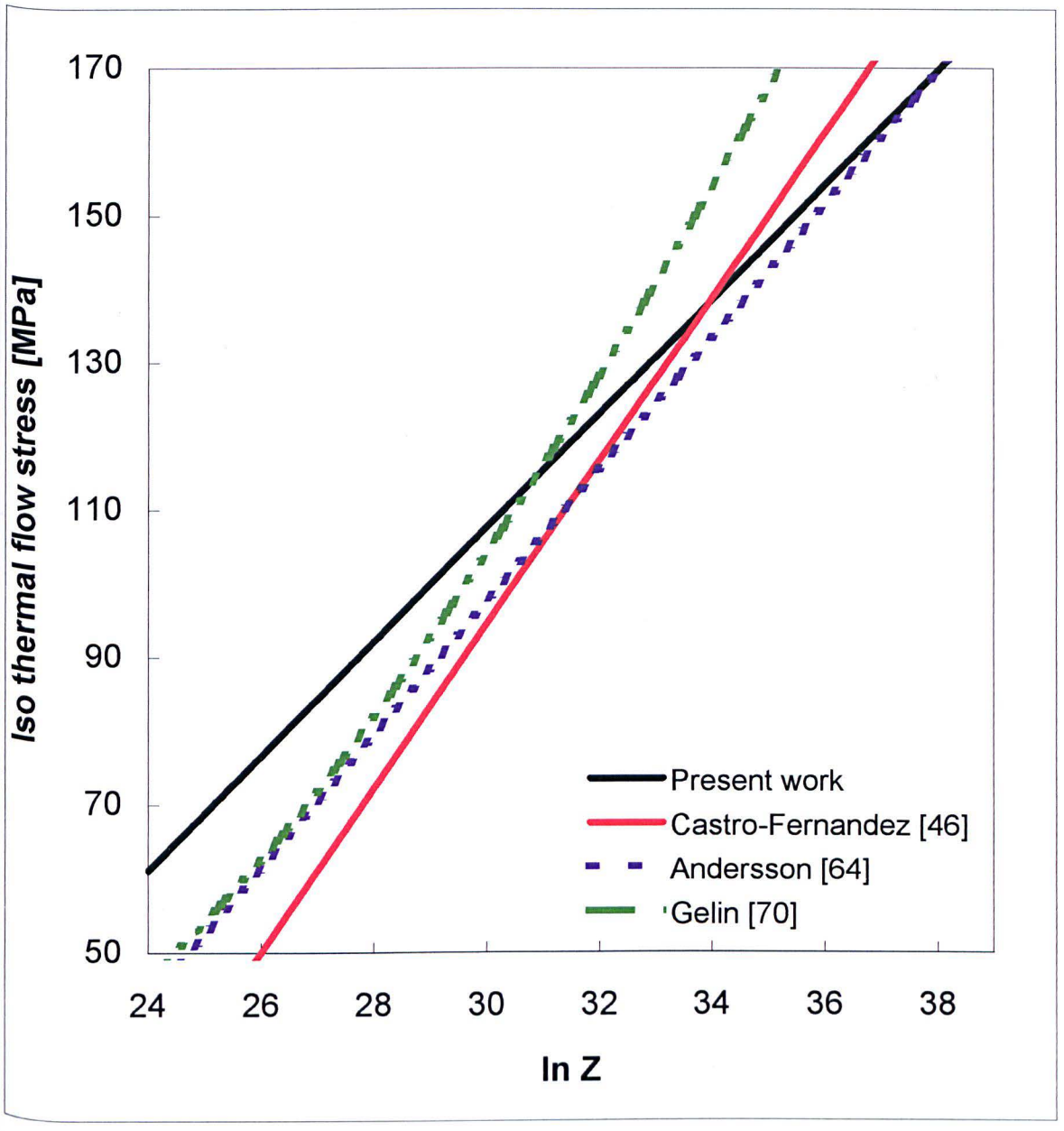

Figure 5.2 Comparison between the steady state flow stress predictions from equation 2.12 using the parameters from the present experimental work and those from the literature (data from Gelin are calculated with equation 5.1)

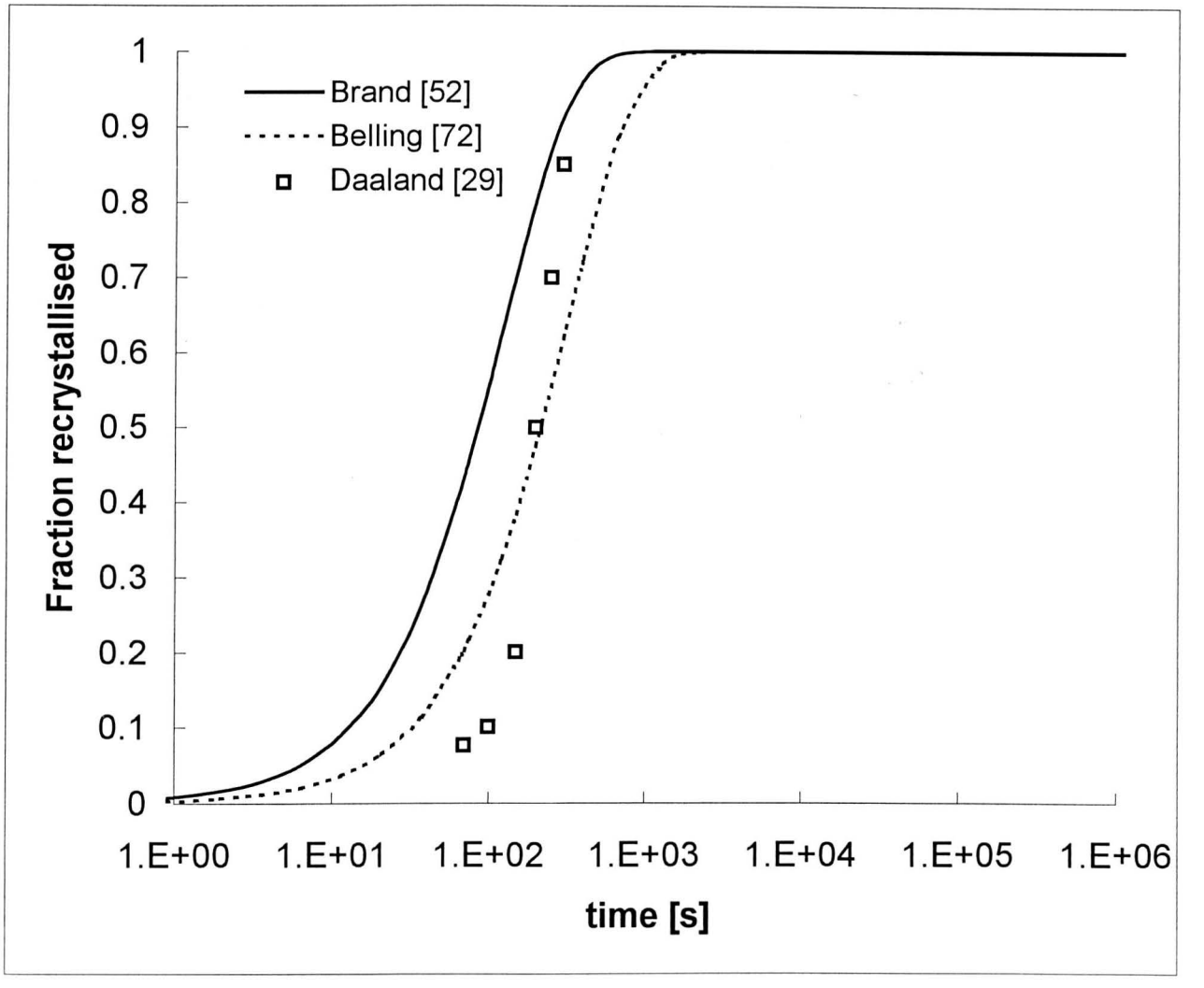

Figure 5.3 Avrami curves from the literature

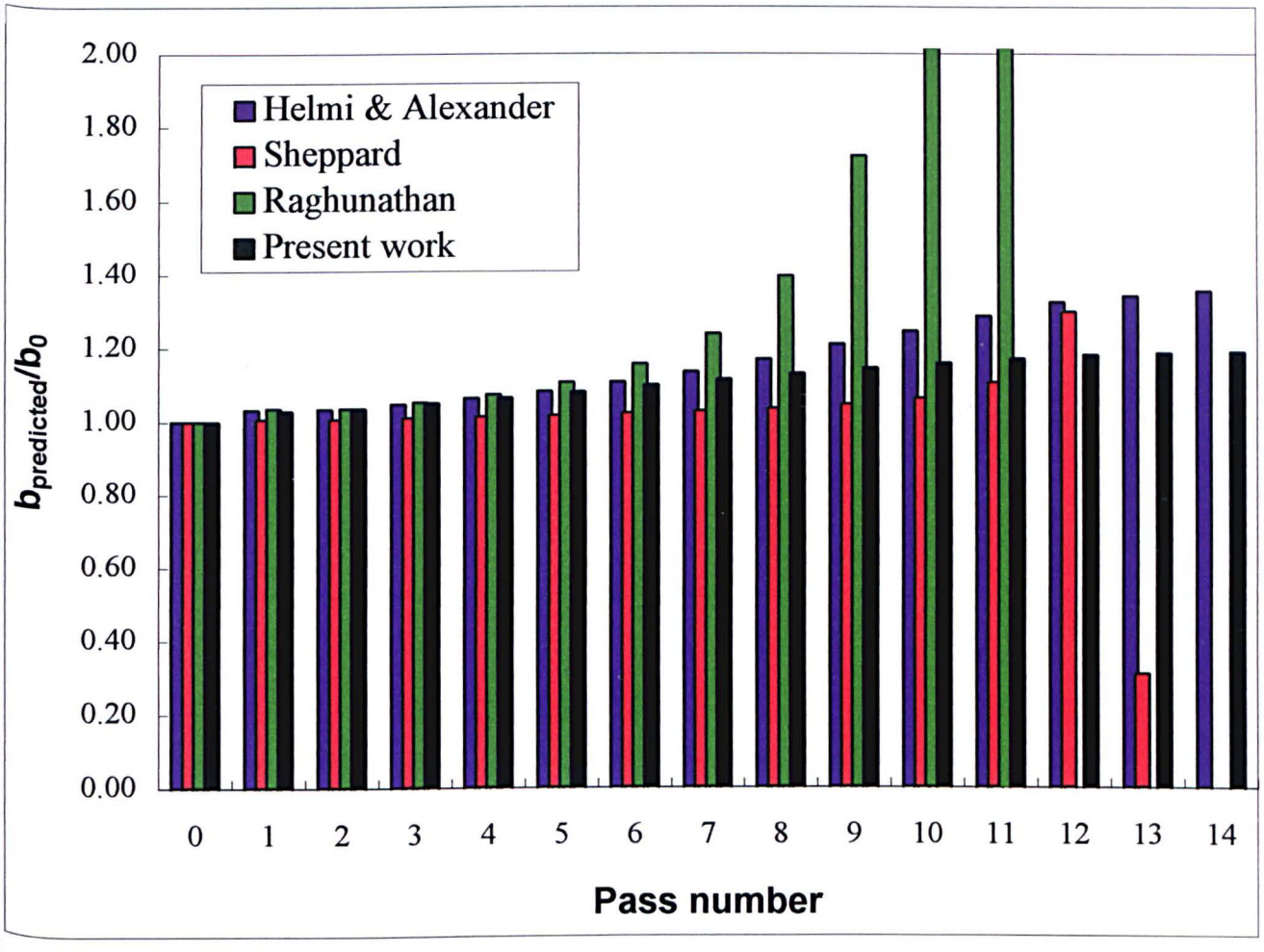

Figure 5.4 Model predictions for the four models

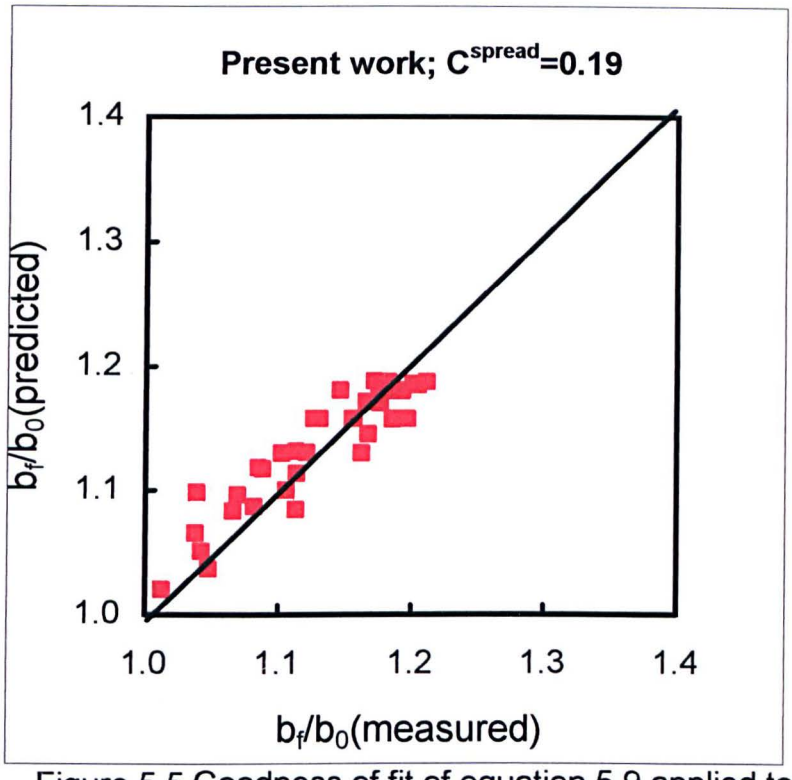

Figure 5.5 Goodness of fit of equation 5.9 applied to series 1 and 2

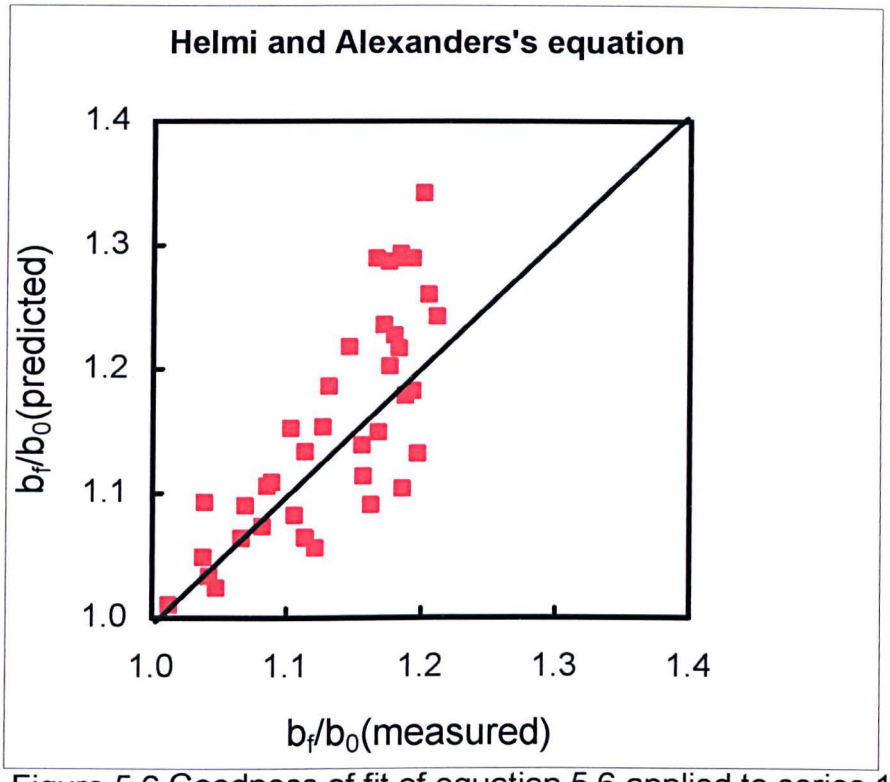

Figure 5.6 Goodness of fit of equation 5.6 applied to series 1 and 2

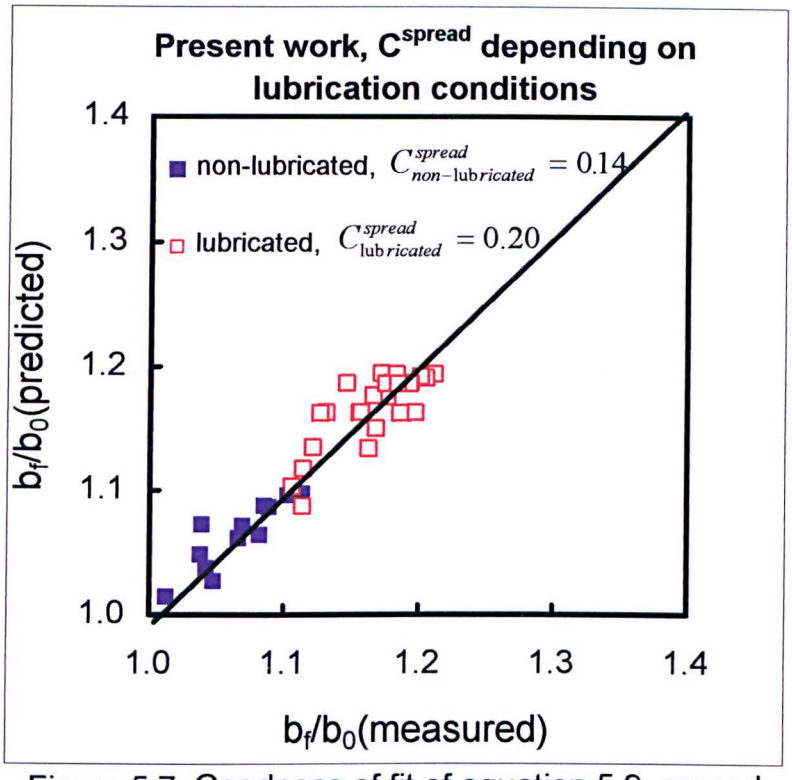

Figure 5.7 Goodness of fit of equation 5.9, spread coefficient depending on friction conditions

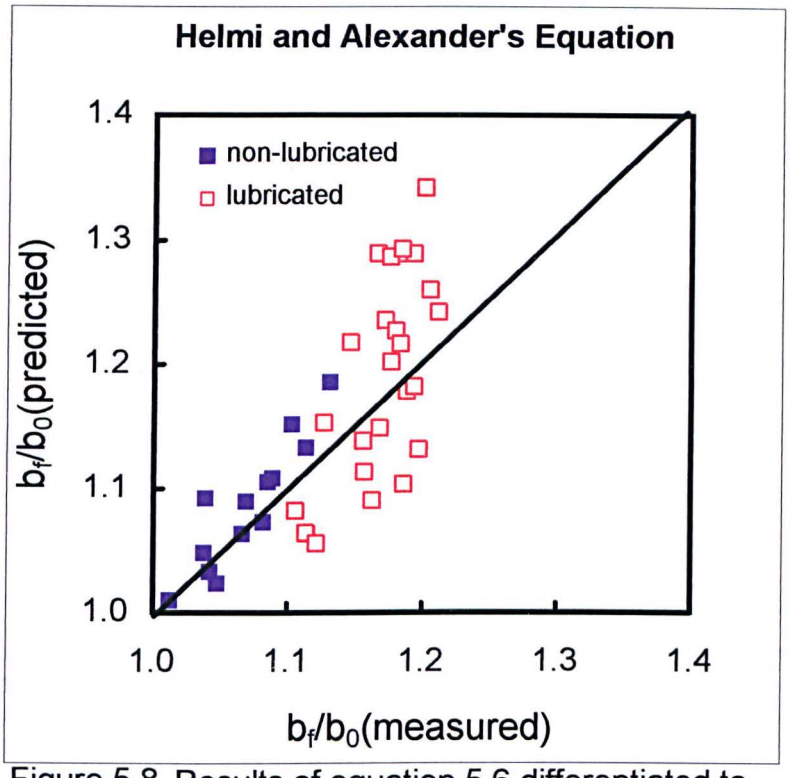

Figure 5.8 Results of equation 5.6 differentiated to lubricating conditions

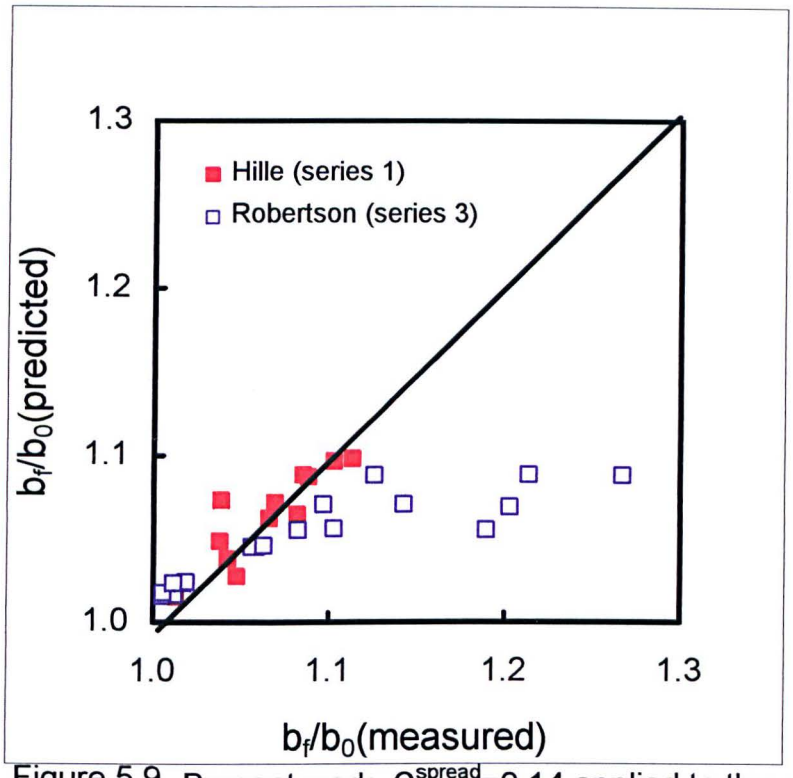

Figure 5.9 Present work, C^{spread}=0.14 applied to the results from the Hille and the Roberston mill

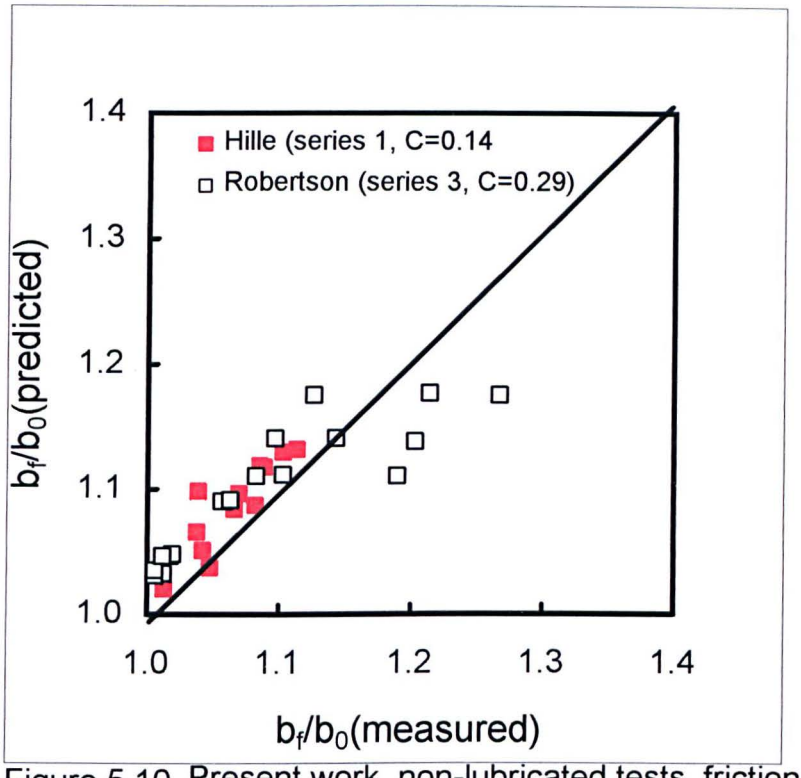

Figure 5.10 Present work, non-lubricated tests, friction coefficient optimised per roll radius.

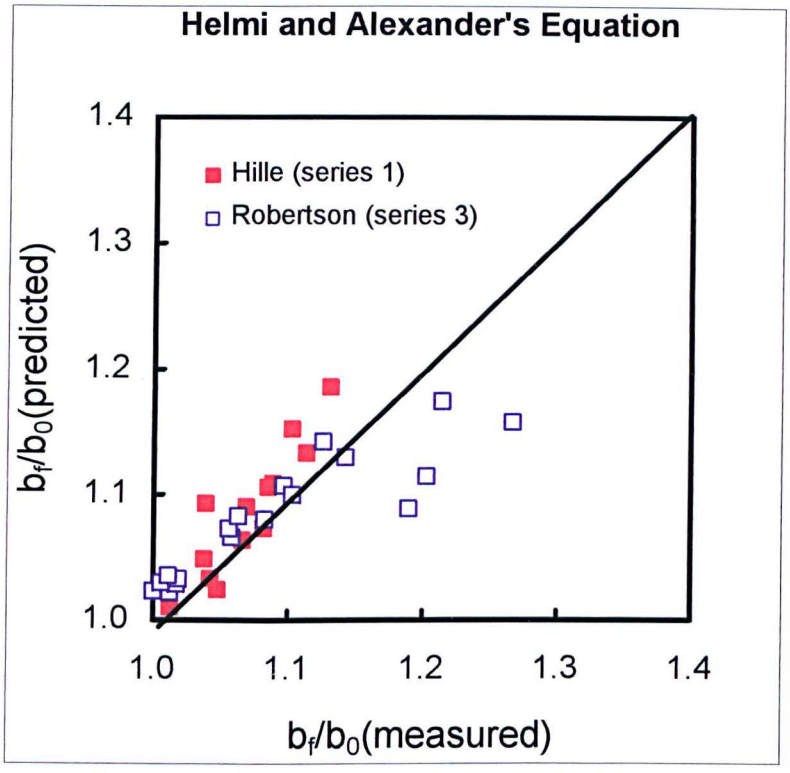

Figure 5.11 Equation 5.6 applied the results from the Hille and the Robertson mill

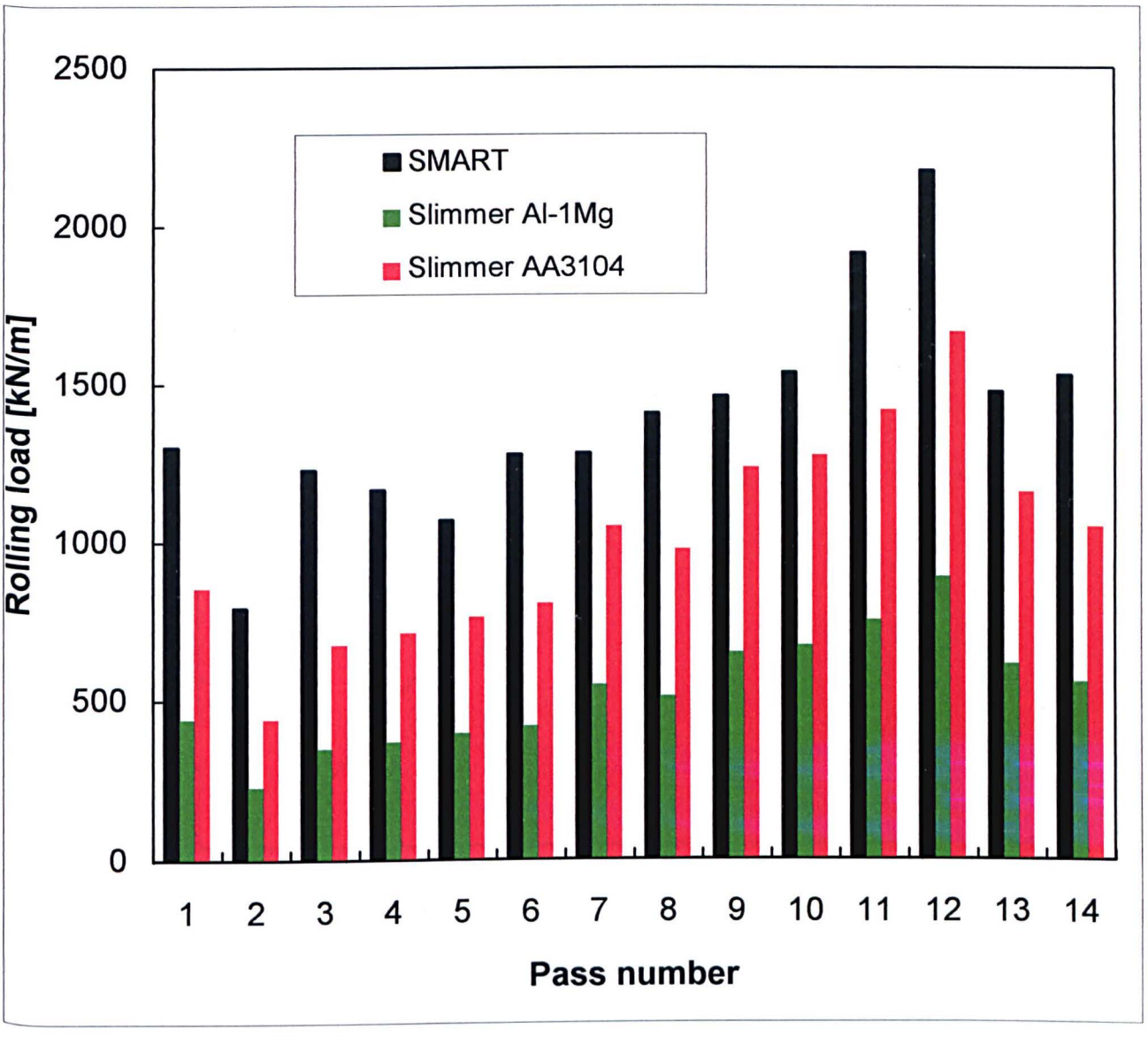

Figure 5.12 Roll force measurements and predictions

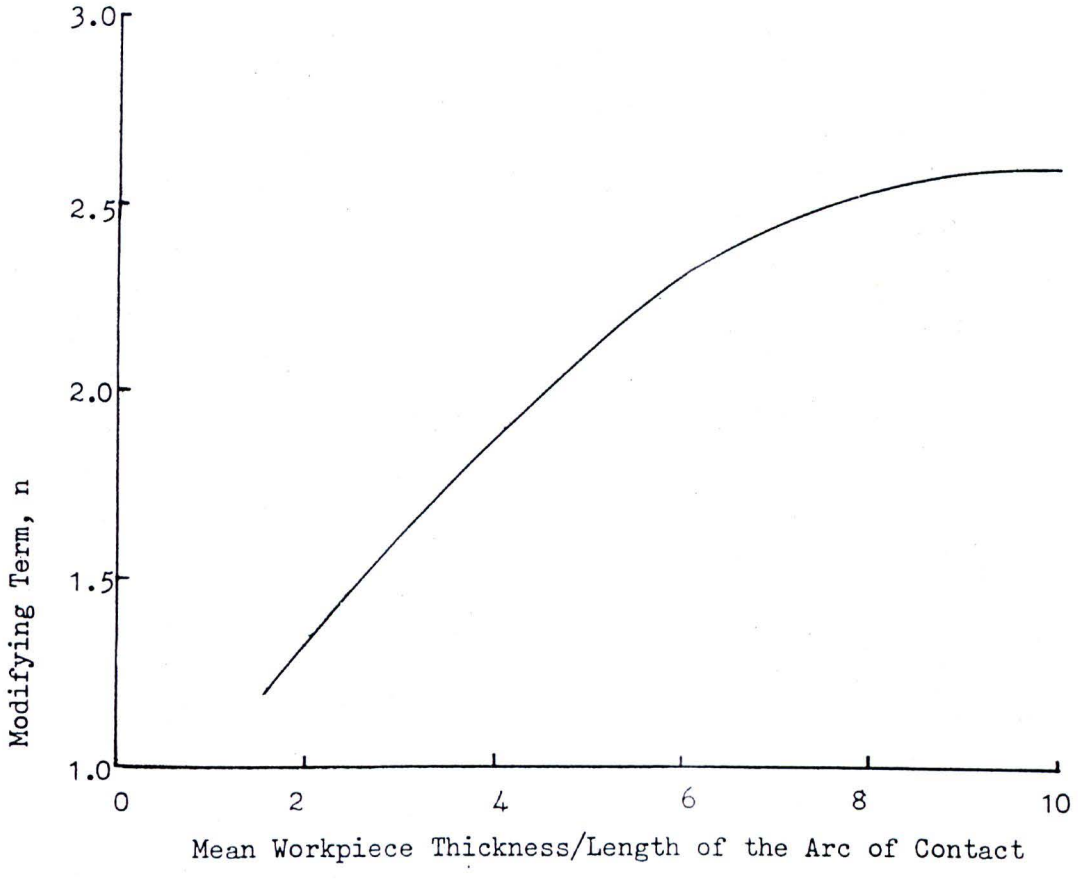

Figure 5.13 Beese's correction factor

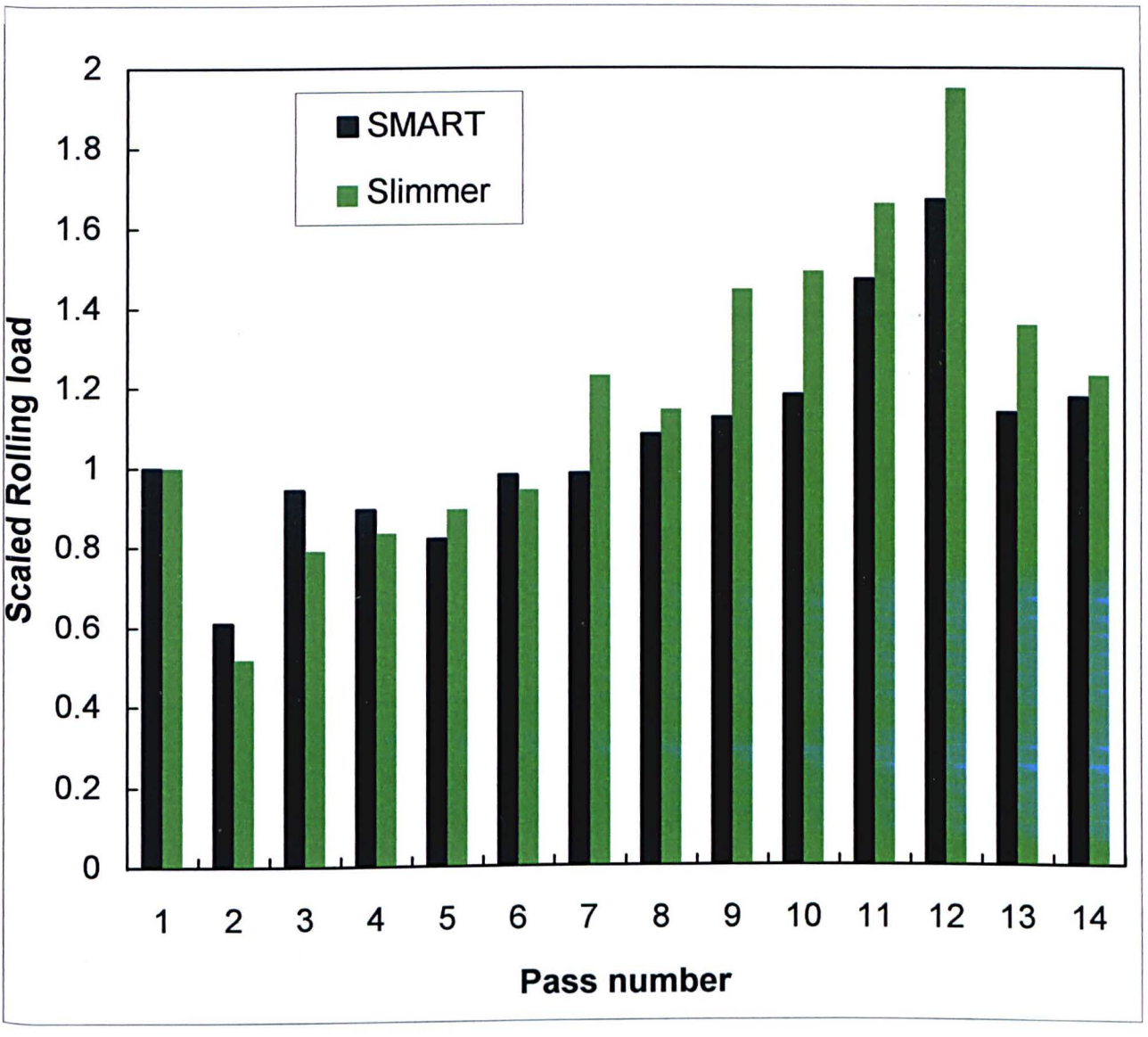

Figure 5.14 Roll force measurements and predictions

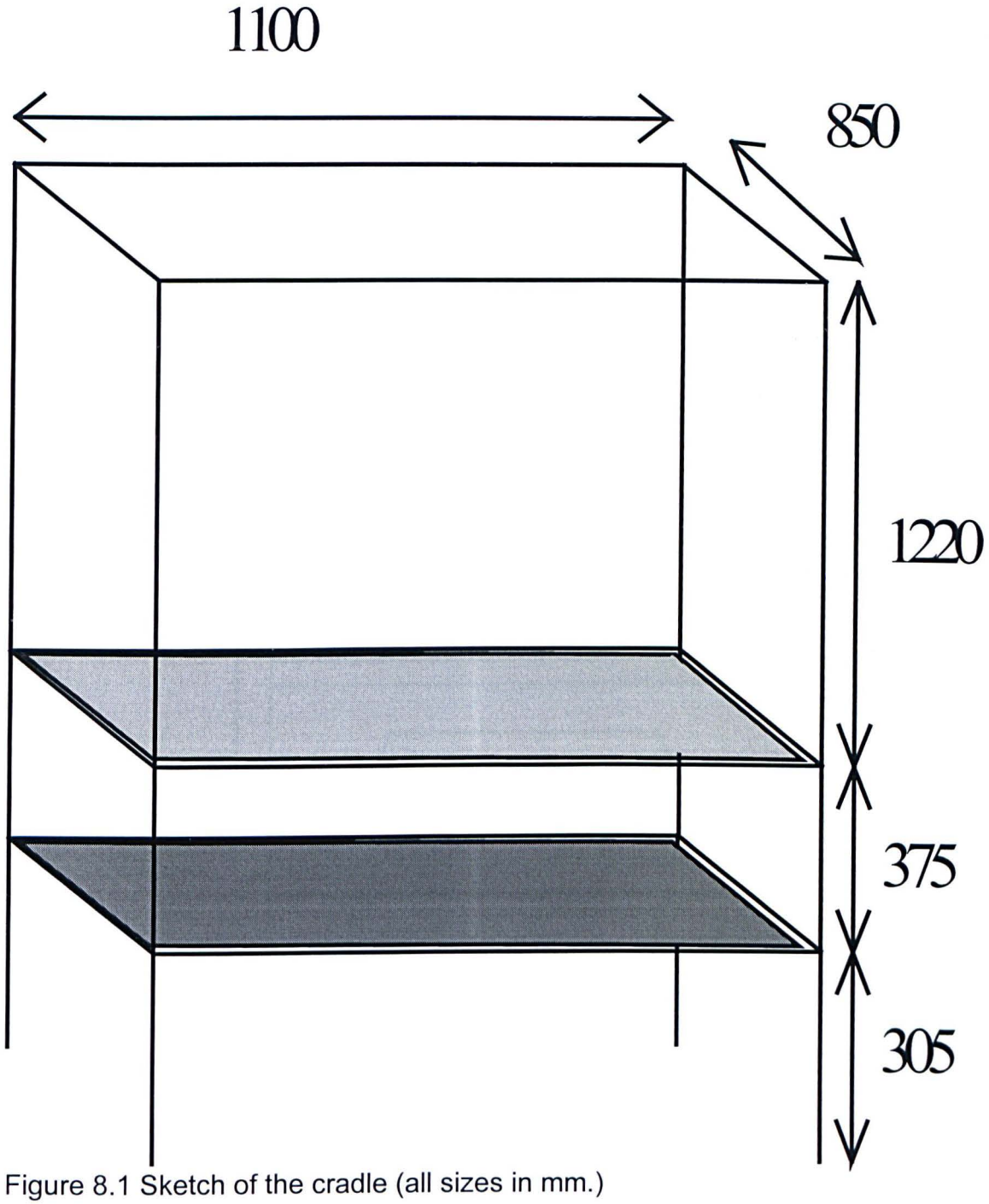

Figure 8.1 Sketch of the cradle (all sizes in mm.)

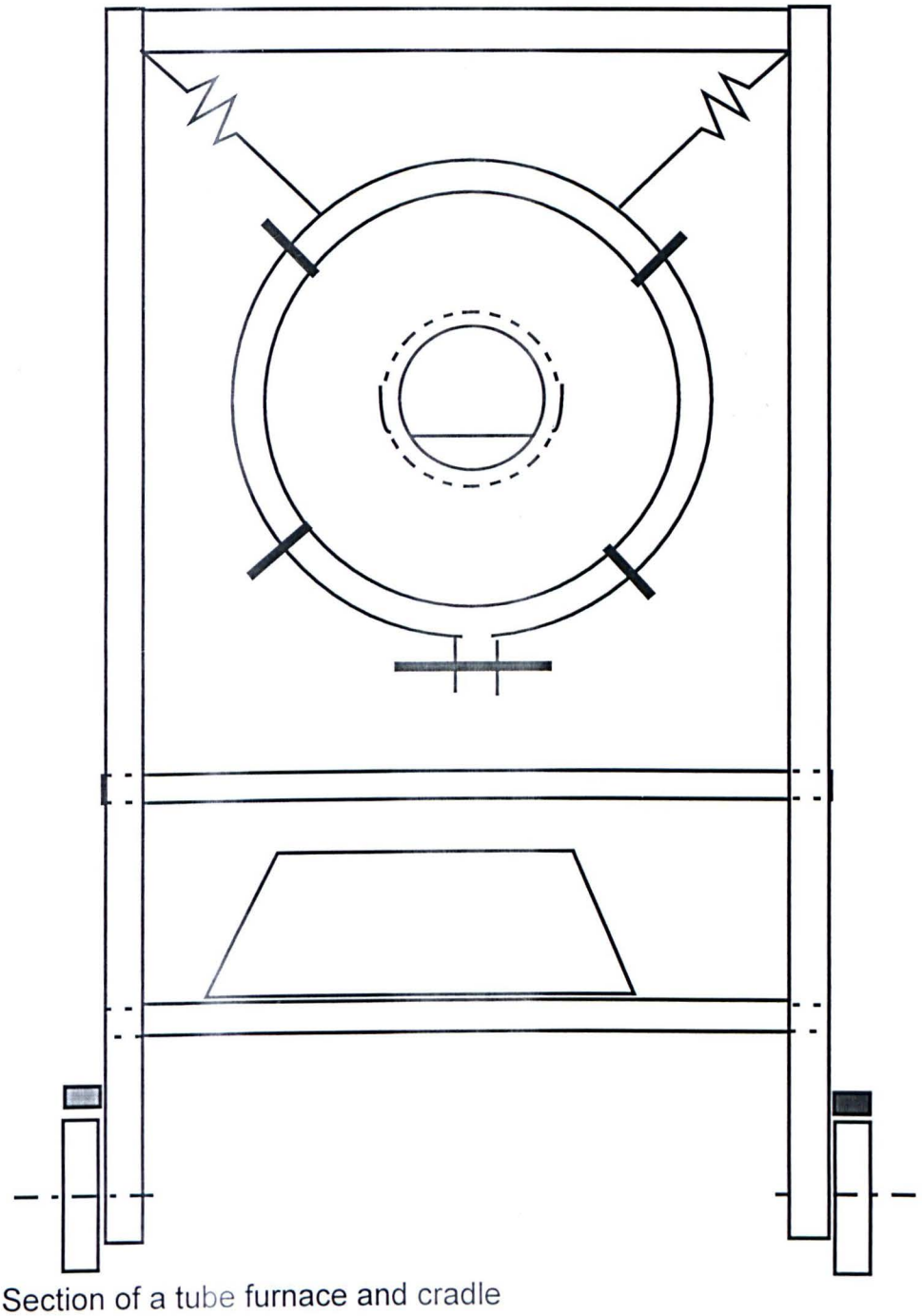

Figure 8.2 Section of a tube furnace and cradle

Figure 8.3 Sketch of the furnace suspension system

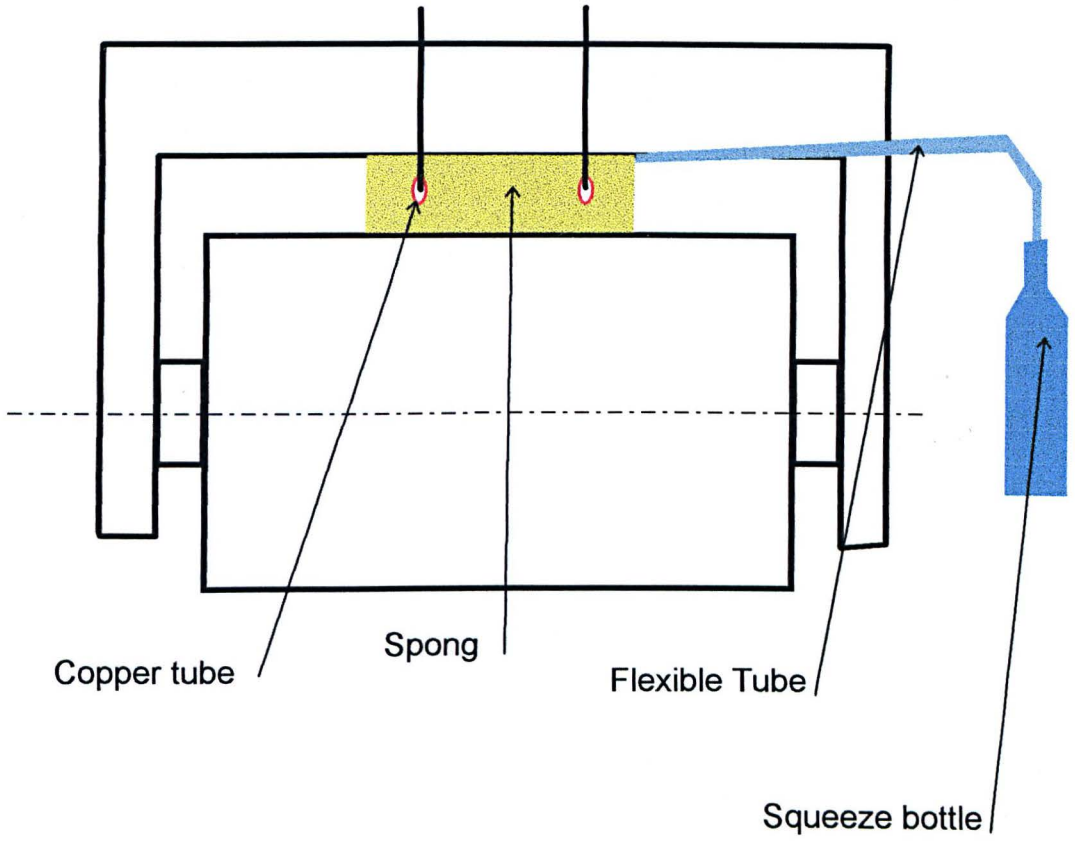

Figure 8.4 Schematic representation of the lubrication system